UNIVERSIDAD DE CONCEPCIÓN
FACULTAD DE CIENCIAS FÍSICAS Y MATEMÁTICAS

CHEMICAL COMPLEXITY IN SIMULATIONS OF CIRCUMSTELLAR DISCS FORMATION

Modeling complex chemical evolution in star forming regions

By: Sebastián Ignacio Aguilar Castillo

Thesis presented to the Faculty of Physical Sciences and Mathematics of the University of Concepción to obtain the Masters Degree in Astronomy

January 2025
Concepción, Chile

Advisor: Stefano Bovino

AGRADECIMIENTOS

Quiero expresar mi más profundo agradecimiento a todas las personas que han estado a mi lado durante este proceso y han hecho posible la culminación de esta etapa de mi vida.

Quiero agradecer especialmente a mi familia quienes me han dado todo el apoyo y cariño que pude necesitar durante estos años. A mis padres, Miguel y Sara, quienes han sido mi guía y mi mayor inspiración. Gracias por preocuparse por mí cada día, por brindarme amor incondicional y por las enseñanzas y reflexiones que han formado la persona que soy y seré. Los amo mucho y agradezco profundamente ser su hijo. A mis hermanos, Javier y Marcelo y nuestra mascota Kirby, gracias por ser una parte fundamental en mi vida y por ser mi distracción en momentos complicados, los atesoro con todo mi corazón. Gracias a mis abuelos, Gilberto y Sara, quienes fueron mis segundo padres y personas muy importantes en mi vida. Y mi pareja, Gardhi, quien vivió todo este proceso más de cerca, gracias por acompañarme tanto en las buenas como en las malas, por ayudarme a poner los pies en tierra en momentos difíciles, gracias por todo lo que has forjado junto a mi, por los momentos de calma que tanto he necesitado y por todo el amor que me has dado. Te amo mucho. También agradezco a tu familia, quienes me han recibido con los brazos abiertos y se han convertido en una segunda familia para mí aquí en el sur, los atesoro profundamente.

Agradezco tambien a mis amigos, a todas aquellas personas con las que compartí estos años, gracias por experiencias inolvidables y momentos que atesoraré siempre. En especial a aquellos amigos más cercanos, Javiera, Joaquín, Pablo y Vanessa. Gracias por su compañía, apoyo y amistad incondicional. Les deseo lo mejor y espero seguir compartiendo con ustedes en el futuro.

Finalmente agradezco a los profesores, a mi profesor guía Stefano y mi colaborador Alessandro quienes me brindaron las herramientas y conocimientos necesarios para realizar este proyecto. También a Dominik, quien, aunque no formó parte directa de mi proyecto, me ofreció su consejo y apoyo en momentos clave.

Resumen

La química desempeña un papel crucial en la formación y evolución de los sistemas estelares, por lo que resulta esencial estudiar el estado químico en regiones de formación estelar mediante simulaciones numéricas. A pesar de su importancia, modelar de networks químicas complejas en simulaciones es un proceso computacionalmente costoso debido al gran número de reacciones y especies implicadas. Para hacer frente a este reto, esta tesis emplea un marco de post-procesamiento para incorporar química compleja en simulaciones SPH de alta resolución. Utilizando el paquete astroquímico KROME, modelamos la evolución de química a lo largo de la historia dinámica de las partículas a partir de simulaciones preexistentes, centrándonos en reacciones en fase gaseosa y de polvo relevantes para la formación y evolución de especies portadoras de $H - C - O$, hasta la formación de metanol (CH_3OH).

En este estudio investigamos la complejidad química de los discos circunestelares formados dentro de un cúmulo de formación estelar. Analizando la estructura vertical de estos discos, identificamos regiones de mayor actividad química y exploramos la distribución espacial de moléculas orgánicas complejas. Nuestros resultados revelan que el metanol, una molécula clave para evaluar la posible complejidad química en regiones de formación estelar, se localiza predominantemente dentro de los discos circunestelares en su fase gaseosa, particularmente en aquellos que rodean objetos estelares más antiguos. Se observaron altas concentraciones de metanol en regiones del disco donde las condiciones físicas no favorecen la formación de esta molécula. Este fenómeno se atribuye al proceso de acreción de material en el disco, en el que las regiones de baja temperatura permiten la formación de metanol en los granos de polvo, que posteriormente se desorbe a la fase gaseosa a medida que el material se acreta hacia las regiones internas del disco, donde las temperaturas superan los 10^4 K.

Este trabajo establece una metodología robusta para integrar química compleja en simulaciones astrofísicas mediante técnicas de postprocesado. Al proporcionar una network química actualizada que incluye reacciones en granos de polvo, ofrece una base para futuros estudios destinados a investigar la evolución química en regiones de formación estelar y discos circunestelares.

Keywords – Astroquímica, Materia circunestelar, Moleculas orgánicas complejas

Abstract

Chemistry plays a crucial role in the formation and evolution of stellar systems, making it essential to study the chemical state of star-forming regions through numerical simulations. Despite its significance, modeling complex chemical networks within simulations is a computationally expensive process due to the large number of reactions and species involved. To address this challenge, this thesis employs a post-processing framework to incorporate complex chemistry into high-resolution smoothed particle hydrodynamics (SPH) simulations. Using the astrochemical package KROME, we model the evolution of chemistry along the dynamical history of particles from pre-existing simulations, focusing on gas and dust-phase reactions relevant to the formation and evolution of $H-C-O$ bearing species, up to the formation of methanol (CH_3OH).

In this study we investigated the chemical complexity of circumstellar discs formed within a simulated star-forming cluster. By analyzing the vertical structure of these discs, we identify regions of enhanced chemical activity and explore the spatial distribution of complex organic molecules. Our results reveal that methanol, a key molecule to assess the possible chemical complexity in star-forming regions, is predominantly located within circumstellar discs in its gas-phase, particularly those surrounding older stellar objects. Unexpectedly, high concentrations of methanol were observed in regions of the disc where the physical conditions do not favor the formation of this molecule. This phenomenon is attributed to the accretion process, wherein low-temperature regions allow the formation of methanol on dust grains, which subsequently desorbs into the gas phase as material is accreted into the inner disc regions where temperatures exceed 10^4 K.

This work sets a robust methodology for integrating complex chemistry into astrophysical simulations via post-processing techniques. By providing an up-to-date chemical network that includes surface reactions, it offers a foundation for future studies aiming to investigate the chemical evolution of star-forming regions and circumstellar discs.

Keywords – Astrochemistry, Circumstellar matter, Complex organic molecules

Contents

List of Tables

List of Figures

Chapter 1

Introduction

Within the frontiers of astronomy and astrophysics, we find different topics which help us to understand how our Universe works and evolves. Among the many different disciplines we can find those processes related to stellar formation and evolution, a topic much studied yet not fully understood, and in turn an important pillar for the understanding of the world around us (McKee and Ostriker, 2007). In the microphysical part of the problem in star formation and evolution processes we deal with different questions. Most specific on the side of protoplanetary and circumstellar systems we ask: How does chemistry in protoplanetary systems behaves? How are the properties of a system determined by the properties of the medium it forms? Which kind of chemical processes are going on inside circumstellar discs and how do these affect the evolution of the system?

To answer these different questions, astronomers and astrophysicists make use of astrochemistry, a powerful tool focused on the study of how chemical processes affect the dynamics of key processes at different scales such as galactic, star and planet forming discs. Astrochemistry has been heavily linked to star- and planet-formation processes due to the influence of different chemical reactions occurring inside pre-stellar and protoplanetary systems and their importance on the evolution of these objects. Different studies and reviews have stated the importance of astrochemistry in star formation processes (Mac Low and Klessen, 2004; Pan and Padoan, 2009; Caselli and Ceccarelli, 2012; Tielens, 2013; van Dishoeck, 2014; Boogert et al., 2015; Widicus Weaver, 2019)

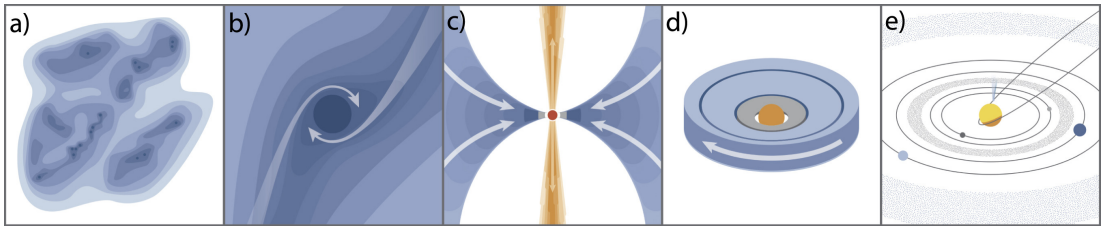

Figure 1.1.1: Stages of low-mass star and planet formation. **a:** Dense cores inside molecular clouds. **b:** Pre-stellar core collapse due to self-gravity. **c:** Protostar formation following the gravitational collapse of the pre-stellar core. Accretion of remnant material through a diks-like structure and outflows characterize this stage.**d:** Pre-main sequence star surrounded by a circumstellar disc, formation site of planets. **e:** Growth of a mature planetary system after the dispersal of the cloud remnant through disc winds.

Source: Öberg and Bergin (2021)

1.1 Star formation

Stars are fundamental to our understanding of astronomy and the Universe. These celestial objects, composed of hot gas, constitute the majority of what we observe in the sky and serve as primary indicators of the structures and evolution of the Universe. Therefore, understanding the processes by which stars form is essential, as it broadens our comprehension of different contexts, such as galactic evolution or the conditions necessary for the development of planetary systems.

Star formation begins in overdense regions of the interstellar medium, mainly composed of gas and dust, known as molecular clouds (MCs; Fig. 1.1.1a). Molecular clouds exhibit turbulent supersonic motions on size scales $\lesssim 0.1$ pc, meaning that the bulk of the cloud's volume experiences motions exceeding their thermal sound speed ($c_s = \sqrt{k_B T/\mu m_p}$). This speed is determined by the cloud temperature (T) and the mean molecular weight (μ), typically around 2.33 for molecular gas with solar composition. The supersonic nature of these motions results in a lognormal density distribution within the clouds (McKee and Ostriker, 2007).

Within molecular clouds are networks of filaments and clumps with intermediate densities (check Fig. 1.1.1a also), ranging from approximately 0.1 to 1 pc in size. These structures further fragment into smaller, dense regions known as prestellar cores, which are cold (~ 10 K) and dense ($10^3 - 10^4$ cm^{-3}) structures formed inside MCs (Jørgensen et al., 2020). These subdense gravitationally bound cores

are known to be the first step of the star formation process (Jørgensen et al., 2020; Öberg and Bergin, 2021; Larson, 2003; Caselli and Ceccarelli, 2012; Andre et al., 2000).

Stars originate from cold molecular interstellar clouds when the inward pull of gravity surpasses the outward push caused by gas and magnetic pressures. The contraction of clouds and the onset of star formation are triggered by compression from shocks, which increases the density. The three primary triggering mechanisms are:

- Clouds passing the density wave of a spiral arm in a spiral galaxy.
- Compression of clouds by a shockwave generated in a nearby supernova explosion.
- Cloud–cloud collisions in colliding or merging galaxies.

The collapse of a molecular cloud begins when its mass M exceeds the Jeans mass

$$M > M_J \approx 100 \left(\frac{T^3}{\mu^4 n} \right)^{1/2} M_\odot \tag{1.1.1}$$

where M_J is the Jeans mass of a homogeneous spherical cloud in terms of temperature T and volume density (particles per cm^3) n. This leads to an initial collapse on a free-fall time scale

$$t_{\mathrm{ff}} \approx (G\rho)^{-1/2} \approx 1 \times 10^8 (\mu n)^{-1/2}\,\mathrm{yr} \tag{1.1.2}$$

Interstellar clouds have cooling processes that facilitate star formation. They lose heat radiatively through primarily two cooling agents: molecular emissions and energy transfer between gas and dust. In dense gases, collisions between molecules result in excitation to elevated rotational or vibrational energy states. An excited molecule can return to a lower state by emitting a photon, a process known as photo de-excitation. The most common transitions are in the infrared (IR) or submillimeter bands. These photons can escape the cloud, as it is optically thin at IR wavelengths. If the density within the cloud is high and the kinetic temperature is sufficiently low ($T < 1000\,\mathrm{K}$), dust can form. Collisions between dust particles and molecules will transfer heat to the dust grains. Similarly, dust grains will

heat up if they absorb photons in the UV, optical, or near-IR spectra. These dust grains then emit radiation similar to that from blackbodies at temperatures below approximately $\sim 1000\,\mathrm{K}$, producing significant IR flux that exits the cloud.

Various cooling processes inhibit the adiabatic heating of a collapsing cloud. The potential energy acquired during contraction is rapidly released, allowing the collapse to occur nearly isothermally. As the density of isothermal clouds increases, the Jeans mass diminishes, enabling the substructures within the cloud to begin contracting. This leads to the fragmentation of the original cloud into sub-clouds that can further divide. This fragmentation is facilitated by the inherently clumpy structure of molecular clouds, likely due to magnetic effects (McKee and Ostriker, 2007).

As the fragments become denser, the fragmentation proceeds more rapidly because the free fall timescale decreases proportionally to $\sim n^{-1/2}$. Eventually, the fragment density increases to the point where they become optically thick to infrared radiation. When this occurs, the cooling mechanism stops and the collapse proceeds adiabatically. This leads to a rise in temperature and a corresponding increase in the Jeans mass to match the actual mass of the fragments. At this stage, the contraction stops and the fragments, now referred to as clumps, achieve hydrostatic equilibrium. These clumps will eventually form stars.

As these prestellar cores become gravitationally unstable, they undergo collapse and form an opaque hydrostatic core (Fig. 1.1.1b). The collapse transforms gravitational energy into radiation, which heats the surrounding envelope, causing a protostar to emerge (Fig. 1.1.1c). This process can create one or several young stellar objects (YSOs), which are encircled by collapsing envelopes and circumstellar discs where planets might eventually form.

During the protostellar phase, the protostar accretes mass from the surrounding collapsing envelope. As this material converges inward, the temperature and density increase progressively towards the core due to the heat generated by the growing star. To conserve angular momentum, a fraction of the infalling material extends outward into a flattened disc. This circumstellar disc functions as an intermediary, directing material towards the star while simultaneously dissipating some of the angular momentum. Observations indicate that this accretion phase is consistently paired with strong bipolar outflows and jets (Fig. 1.1.1c), which help

to remove additional angular momentum from the infalling material (Bachiller, 1996).

The system keeps accreeting mass from the envelope as it evolves. Once the envelope disperses, we are left with a pre-main sequence star, sufficiently hot to initiate fusion, and a Keplerian disc surrounding it, known as a protoplanetary disc (Fig. 1.1.1d). The protoplanetary disc phase lasts for approximately 1-10 million years, based on disc occurrence rates in stellar clusters with known median ages (Mamajek, 2009). During this period, the disc material is accreted onto the star, onto planets, and is dispersed through interactions with stellar photo-evaporative winds (Ercolano and Koepferl, 2014). What remains is a young planetary system that can continue evolving for hundreds of millions of years due to collisions between the remaining planets and planetesimals (Fig. 1.1.1e).

As free-fall collapse stops, the core of the clump attains equilibrium initially, with the surrounding gas continuing to accrete onto the core. At this stage, the clump is considered a protostar. Prior to this, the temperature was extremely low and the density was exceedingly high, leading to hydrogen being present as molecules and an active cooling process. This phase concludes when H_2 is broken down and the majority of the hydrogen becomes ionized.

1.2 Chemistry during star formation

The role of chemistry in star formation and stellar evolution is of great importance to understand the intricate processes that govern the formation and evolution of celestial bodies (van Dishoeck and Blake, 1998). From the dense molecular clouds that give birth to stars to the complex chemical environments of circumstellar and protoplanetary discs, chemistry provides critical insights into the physical conditions and evolutionary pathways of astronomical objects.

As mentioned in Section 1.1, star formation begins in molecular clouds, these stellar nurseries undergo specific processes to form stars inside, and one of these processes is cooling. One of the main cooling mechanisms in clouds is line radiation from molecules, being CO the dominant coolant within these regions (Goldsmith and Langer, 1978), which is the second most abundant molecule in these clouds, and an efficient coolant due to its rotational transitions that emit at millimeter and submillimeter wavelengths, allowing it to radiate away thermal energy and

cool the cloud.

In addition to simple diatomic molecules such as CO and H_2, star forming regions (SFRs) are also rich in complex organic molecules (COMs). These molecules, including methanol (CH_3OH) and formaldehyde (H_2CO), are typically formed on the surfaces of dust grains. Dust grains act as catalysts for chemical reactions, where atoms and simple molecules adsorb onto their surfaces, undergo chemical reactions, and then desorb back into the gas phase either thermally or through non-thermal processes such as photodesorption (Garrod et al., 2008). These COMs are not just passive tracers of physical conditions, but can significantly influence the star formation process. They can affect the chemistry of the gas, alter the ionization fraction, and participate in the cooling processes. Furthermore, COMs can be incorporated into the material that forms protoplanetary discs, influencing the initial chemical composition of emerging planetary systems (Herbst and van Dishoeck, 2009).

In general, chemistry in star-forming regions has profound implications for the formation of protoplanetary discs and, consequently, planetary systems (Öberg et al., 2010). As the molecular cloud collapses and forms a protostar, the surrounding material flattens into a rotating disc. The chemical composition of this disc is initially determined by the molecular cloud from which it formed. The incorporation of COMs into the disc can lead to the formation of prebiotic molecules and potentially, the building blocks of life (Jørgensen et al., 2012, 2020; Öberg and Bergin, 2021).

The different evolutionary stages during star formation are characterized by different density, temperature, and radiation profiles, as well as unique chemical compositions. This allows us to recognize different processes or star formation phases using different observable molecules when studying molecules lines. This information offers invaluable insights into the different processes related to stellar evolution and the formation of planetary systems.

Fig. 1.2.1 offers an explanatory view of the advantages of understanding the distinctive molecules used to characterize different structures or phases related to stellar evolution, i.e., it illustrates emission patterns for six commonly employed molecules to study cloud structures (HCN), PDRs (C_2H), prestellar cores (N_H^+), protostellar outflows (H_2O), protostellar cores (complex organics),

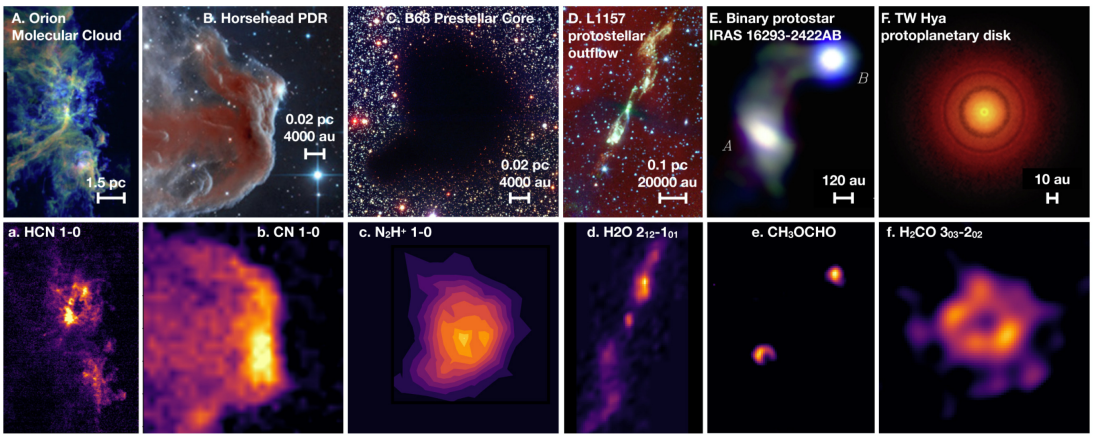

Figure 1.2.1: Illustrations of characteristic chemical structures associated with the different stages and scales of star and planet formation.
Source: Öberg and Bergin (2021)

and protoplanetary discs (H_2CO) (Öberg and Bergin, 2021).

1.3 Protoplanetary/Circumstellar discs

Since their first discovery in the Orion Nebula (McCaughrean and O'Dell, 1996), circumstellar and protoplanetary discs have raised substantial interest from astronomers because of their essential role in the processes of star and planet formation.

The origin of protoplanetary and circumstellar discs is the remnant of the star formation process, being a natural consequence of the conservation of angular momentum, a process well documented in both observational and theoretical studies (Hartmann, 1998; Williams and Cieza, 2011). The initial collapse within the hosting molecular cloud leads to the creation of a rotating dust- and gas-rich disc around many pre-main-sequence stars (Shu et al., 1987). The term "protoplanetary" is adopted because these objects are the formation sites of planetary systems (Williams and Cieza, 2011). These discs act as an accretion reservoir, providing the raw material onto the growing star and regulating its mass growth.

The significance of protoplanetary discs extends beyond stellar growth. They are the birthplaces of planets, as solid particles within the disc collide and stick together, gradually forming planetesimals and, eventually, planets (Armitage,

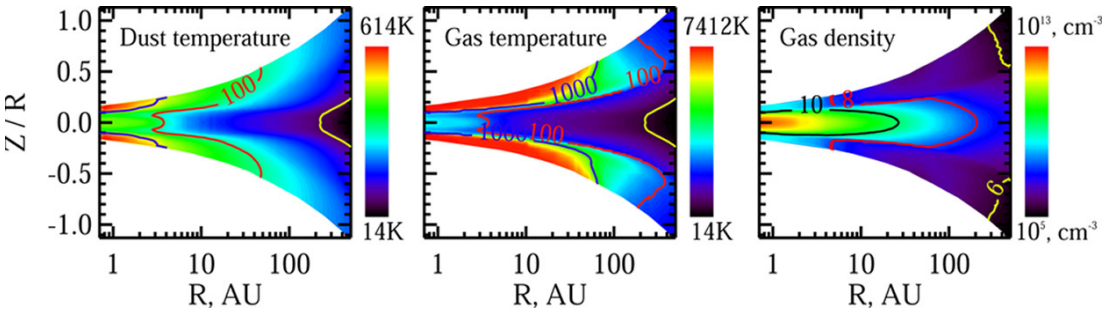

Figure 1.3.1: A vertical cross-section of a protoplanetary disc similar to the DM Tau system, determined using the ANDES thermochemical disc model (Akimkin et al., 2013). (Left) Depicts the radial and vertical distribution of dust temperature (in Kelvin). (Middle) Shows the radial and vertical distribution of gas temperature (in Kelvin). It is notable that gas temperatures are significantly higher than dust temperatures in the disc's surface layers. (Right) Illustrates the radial and vertical distribution of gas particle density (in cm^{-3}).

Source: Henning and Semenov (2013)

2011). The properties of the disc, such as its mass, temperature distribution, and chemical composition, directly influence the types of planet that can form and their potential habitability.

Protoplanetary and circumstellar discs are crucial in the context of stellar evolution, as they regulate the mass accretion onto the protostar and determine the final mass of the star. These discs also play a vital role in the formation of planetary systems. The processes within the disc, such as dust coagulation, planetesimal formation, and planetary embryo growth, set the stage for the eventual formation of planets (Lissauer, 1993; Testi et al., 2014). Understanding these discs allows astronomers to infer the conditions that lead to the formation of different types of planet, from terrestrial rocky planets to gas giants (Morbidelli et al., 2012; Öberg et al., 2023).

Protoplanetary discs show varied shapes and complex structures. Their temperatures span from 10 K up to 10000 K, and they feature high densities (e.g., 10^{15} cm^{-3}) down to interstellar medium-like conditions ($< 10^{4}$ cm^{-3}). These general conditions lead to a range of different chemical properties. The structure is marked by both radial and vertical gradients in temperature and density (refer to Fig. 1.3.1).

From the outermost parts of a disc to its most heavily shielded interiors, we observe varying chemical conditions. Radiation can reach the upper regions

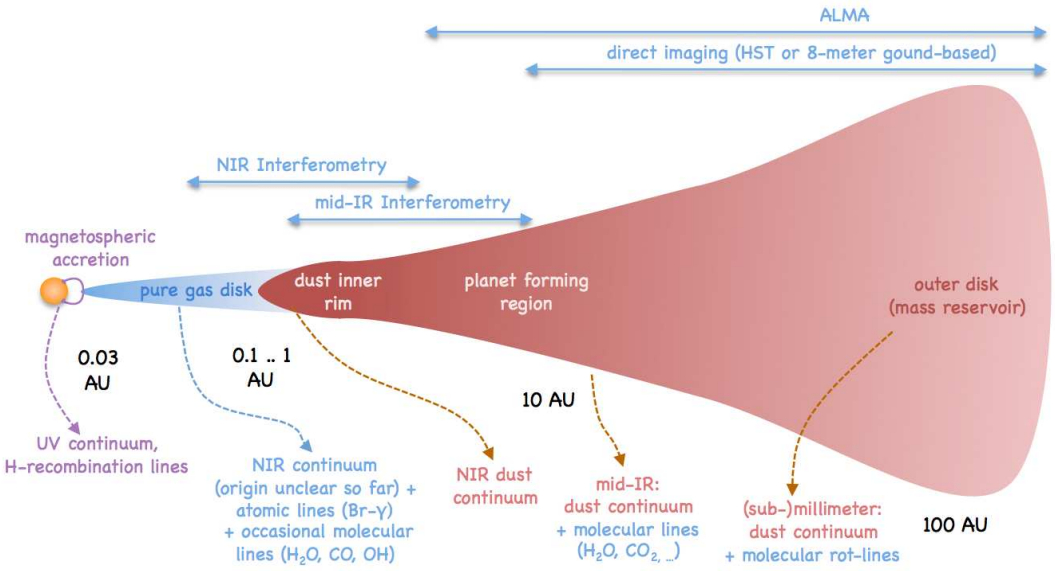

Figure 1.3.2: Diagram representing the structure and spatial dimensions of a protoplanetary disc. Note that the radial scale on the x-axis is nonlinear. The top of the diagram indicates the techniques capable of spatially resolving different scales, while the bottom shows the types of emissions originating from various disc regions.

Source: Dullemond and Monnier (2010)

of discs, facilitating complex molecular interactions, while in the well-shielded interiors the temperatures drop so significantly that molecules freeze out. The discs are also characterized by the evolution of dust particles, starting from microscopic grains that grow into pebbles and ultimately form planets. This progression significantly influences the disc's physical structure and consequently its chemistry.

Generally, a protoplanetary disc can be divided into two main regions: inner and outer disc. Fig. 1.3.2 shows a representation of the different structures present inside a protoplanetary disc.

1.3.1 Inner and outer disc chemistry

The inner disc, located within a few astronomical units (AU) of the central star, is characterized by extreme physical conditions. Typically, temperatures in this region exceed 10^3 K, and densities can surpass 10^{12} cm^{-3} (Najita et al., 2007; Henning and Semenov, 2013). This high-energy environment is situated interior to the water snowline, where volatiles are entirely in the gas phase due to sublimation

and short chemical timescales reset the chemistry (Pontoppidan et al., 2014).

The abundance of gas-phase species, coupled with the intense radiation from the central star, creates an ideal environment for the formation of complex chemical compounds. Observational evidence from infrared (IR) spectroscopy has confirmed the presence of various gas-phase species, including inorganic neutrals such as H_2, OH, H_2O, CO, and isotopologues like ^{13}CO, $C^{18}O$, and $C^{17}O$. Additionally, small organic molecules like HCN and C_2H_2 have been detected, along with sulfur-bearing compounds such as H_2S (Carr and Najita, 2011; Mandell et al., 2012; Najita et al., 2021).

The chemical environment in the inner disc is further influenced by three-body, endothermic, and high energy barrier reactions, which are facilitated by the elevated temperatures and densities. These reactions, along with continuous material transport from the outer disc and strong irradiation fields, may prevent the inner disc chemistry from reaching equilibrium (e.g., Ádámkovics et al., 2014). Chemical models predict the presence of N-bearing molecules (e.g., NH_3, HCN) and hydrocarbons (e.g., CH_4, C_2H_2) in this region, highlighting the importance of gas-phase chemistry in shaping the molecular composition (Willacy et al., 1998; Markwick et al., 2002; Najita et al., 2011).

Beyond the water snowline, extending to several hundred AU, lies the outer disc, which is characterized by significantly lower temperatures, often reaching tens of Kelvin, and reduced densities compared to the inner disc. The outer disc can be subdivided into distinct vertical layers, each exhibiting unique physical and chemical properties (Aikawa and Herbst, 1999).

The disc midplane, the innermost layer, is a cold, dense, and largely chemically inert region due to its effective shielding from ionizing radiation. Temperatures in the midplane can drop below 20 K, and densities can range from 10^6 to 10^8 cm^{-3}, leading to the rapid freeze-out of molecules onto dust grains (Henning and Semenov, 2013). The freeze-out timescales in this region are on the order of 10 to 1000 years, indicating that most molecules in the gas phase will condense onto grain surfaces within a fraction of the disc's lifetime. This process leads to the formation of icy mantles on dust grains, which are then processed by cosmic rays, driving further chemical evolution on grain surfaces.

Above the midplane is the warm molecular layer, where temperatures range

between 30 and 70 K. This layer is partially shielded from ultraviolet (UV) and X-ray radiation, allowing for a rich molecular chemistry driven by neutral-neutral and ion-molecule gas-phase reactions, in conjunction with grain surface chemistry (Dutrey et al., 2014; Aikawa et al., 2022). In this region, CO remains in the gas phase, protected from freeze-out, whereas water and other volatiles are predominantly frozen onto dust grains. The resulting gas-phase chemistry is carbon-rich due to the high C/O ratios, with photodesorption processes playing a significant role in maintaining the molecular gas phase in less opaque regions (Öberg et al., 2007, 2009b,a).

The outermost layer of the disc, the surface layer, is exposed to strong stellar UV radiation and the interstellar radiation field. This region is characterized by low densities and moderately high temperatures, which foster a photon-dominated region (PDR) where photochemistry is the dominant process (Glassgold et al., 2004; Nomura et al., 2007). In these layers, molecules are subject to ionization and dissociation, and ion-molecule reactions become prevalent. The chemistry in the disc surface is highly dependent on the strength and shape of the radiation field, leading to a diverse array of chemical products (Dutrey et al., 2014; Henning and Semenov, 2013).

The varying physical conditions within protoplanetary discs give rise to a complex and diverse chemical environment (see Table 1.3.1), where processes such as photochemistry, molecule-ion reactions, and gas-grain surface interactions play crucial roles. Understanding these chemical processes is essential for elucidating the mechanisms of planet formation and the initial conditions that determine the composition of emerging planetary systems.

1.4 Computational Astrochemistry

Chemical models in astrophysics are indispensable tools for bridging the gap between observable phenomena and the underlying physical processes that govern the evolution of astronomical environments. By simulating chemical processes under various astrophysical conditions, these models allow researchers to predict the abundances of molecules and elements in different regions of space. This predictive capability is crucial for a comprehensive understanding of the cosmic environment, including the formation and evolution of stars, planets, and other

Table 1.3.1: Chemical reactions active in discs

Process	Example	Midplane $r > 20$ AU	Molecular layer $r > 20$ AU	Atmosphere $r > 20$ AU	Inner zone $r < 20$ AU
Bond formation					
Radiative association	$C^+ + H_2 \rightarrow CH_2^+ + h\nu$	X	X	X	X
Surface formation	$H + H\|\|gr \rightarrow H_2 + gr$	X	X	0	0
Three-body	$H + H + H \rightarrow H_2 + H$	0	0	0	X
Bond destruction					
Photodissociation	$CO + h\nu \rightarrow C + O$	0	X	X	X
Dissociation by CRP	$H_2 + CRP \rightarrow H + H$	X	X	0	0
Dissociation by X-rays	—	0	X	X	X
Dissociative recombination	$H_3O^+ + e^- \rightarrow H_2O + H$	X	X	X	X
Bond restructuring					
Neutral-neutral	$O + CH_3 \rightarrow H_2CO + H$	X	X	0	X
Ion-molecule	$H_3^+ + CO \rightarrow HCO^+ + H_2$	X	X	X	X
Charge transfer	$He^+ + H_2O \rightarrow He + H_2O^+$	X	X	X	X
Unchanged bond					
Photoionization	$C + h\nu \rightarrow C^+ + e^-$	0	X	X	X
Ionization by CRP	$C + CRP \rightarrow C^+ + e^-$	X	X	0	0
Ionization by X-rays	—	0	X	X	X

Source: Henning and Semenov (2013)

celestial bodies.

The integration of chemical models with hydrodynamic and radiative transfer simulations is particularly vital for exploring complex interactions between chemistry and physics, such as thermal processes, i.e. cooling and heating, dust-grain chemistry, and radiation-matter interactions (Grassi et al., 2014; Bovino et al., 2019). In star-forming regions, where gas dynamics and chemistry are intricately linked, these models play a significant role in understanding the mechanisms behind star and planet formation.

Modeling the chemical evolution within circumstellar and protoplanetary discs requires solving complex networks of chemical reactions that include both gas-phase interactions and processes involving dust grains. These models must account for the diverse physical conditions present in these environments (see Section 1.3), such as temperature gradients, density variations, and intense radiation fields, to accurately simulate chemical evolution. A key challenge is achieving a proper balance between computational efficiency and the accuracy of these models.

An accurate treatment for the evolution of a system would require on-the-fly (OTF) non-equilibrium chemistry calculations in hydrodynamics simulations, where chemical evolution is integrated directly within hydrodynamic simulations. This method ensures a self-consistent evolution of both the physical and chemical

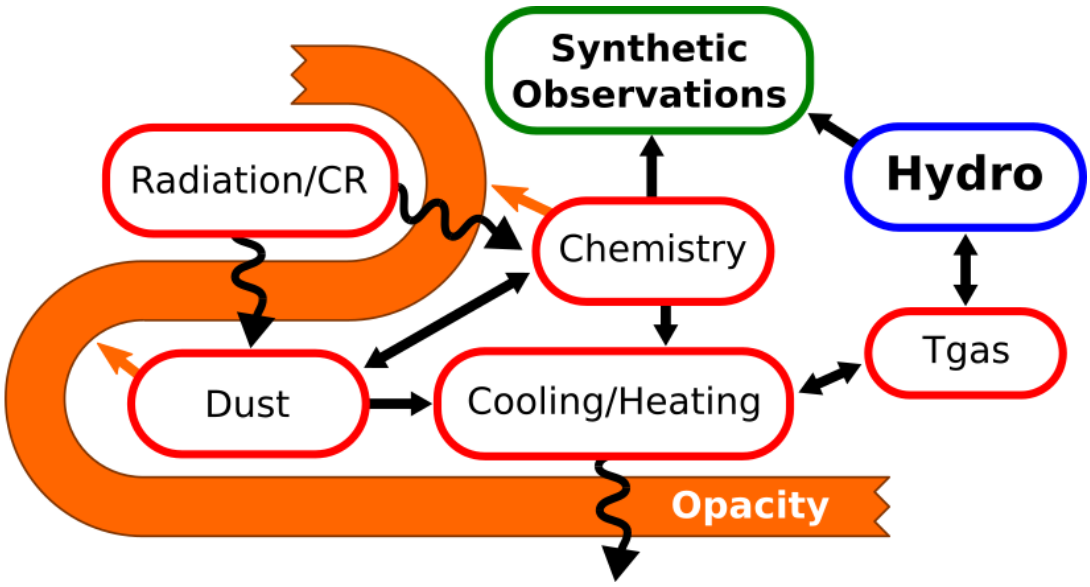

Figure 1.4.1: Sketch of the complex interplay between microphysics and chemistry.

Source: (Bovino et al., 2019)

properties of the system, as chemical processes are calculated simultaneously with the hydrodynamic equations. OTF chemistry provides a detailed and accurate representation of the interactions between physical and chemical processes (see Fig. 1.4.1), making it ideal for studying environments where these interactions are strongly coupled, such as in star-forming regions or the dense midplanes of protoplanetary discs. Many efforts have been made in the last decades to properly include non-equilibrium chemistry in simulations, accounting from simple models to trace specific species (Gnedin et al., 2009; Christensen et al., 2012; Tomassetti et al., 2015; Katz et al., 2017; Pallottini et al., 2017; Lupi et al., 2018; Nickerson et al., 2018) to more complex ones even including metal elements (Glover et al., 2010; Hu et al., 2016; Richings and Schaye, 2016; Capelo et al., 2018; Lupi et al., 2020; Lupi and Bovino, 2020).

However, the inclusion of complex chemical networks in three-dimensional simulations demands significant computational resources. The computational expense arises from the need to solve coupled ordinary differential equations (ODEs) for chemical reactions at each time step, which must account for the formation and destruction of various species (see Grassi et al., 2014; Bovino et al., 2019). If in addition one wants to account for the thermal evolution of the system coupled to chemistry, one needs to account for the rate of temperature change in

time:

$$\frac{dT}{dt} = \frac{\gamma - 1}{k_B \sum_i n_i} \left[\Gamma(T, \bar{n}) - \Lambda(T, \bar{n})\right] \tag{1.4.1}$$

with $\Gamma(T, \bar{n})$ and $\Lambda(T, \bar{n})$ the cooling and heating functions in terms of temperature (T) and the vector that contains the abundances of all species ($\bar{n}$), the dimensionless adiabatic index γ (see Grassi et al., 2011), and k_B the Boltzmann constant. This makes the task of including chemistry in numerical simulations highly demanding, often requiring sophisticated and computationally intensive numerical solvers (Glover et al., 2010).

To overcome the computational challenges associated with OTF chemistry, post-processing techniques have been developed as a more efficient alternative. This approach is based on the integration of the chemical equations over the extracted properties of a standard simulation, i.e. without OTF chemistry (see, e.g. Ferrada-Chamorro et al., 2021). This method allows for detailed chemical analysis of specific regions within the disc without the computational demands of OTF chemistry.

The primary advantage of post-processing techniques is their computational efficiency. By decoupling chemical calculations from hydrodynamic simulations, researchers can apply more complex chemical networks and study a broader range of conditions without being limited by the computational demands of OTF chemistry. This approach is particularly beneficial when studying large-scale systems or focusing on specific regions such as circumstellar discs, where different regions may exhibit vastly different chemical behaviors due to variations in temperature, density, and radiation. Furthermore, post-processing offers greater flexibility in the choice of chemical networks and reaction rates, which can be adjusted or refined based on the objectives of the study and the general properties of the base simulation (Ruaud et al., 2018; Ferrada-Chamorro et al., 2021; Coutens et al., 2020).

However, post-processing techniques are not without limitations. One of the key challenges is the potential loss of accuracy in scenarios where the chemistry strongly influences the physical conditions of the system, such as in temperature-dependent simulations. In such cases, the decoupling of chemical and hydrodynamic processes

may lead to discrepancies between the simulated and actual conditions within the disc. Nonetheless, for many applications, particularly those involving large chemical networks or studies focused on specific chemical processes, the benefits of post-processing outweigh these limitations (Ferrada-Chamorro et al., 2021).

Chapter 2

Methods

This chapter aims to provide an overview of the methodology employed in this study to investigate the theoretical aspects of chemical complexity in numerical simulations through post-processing techniques. We have taken the approach of combining advanced computational techniques with astrophysical models that simulate conditions within interstellar clouds to model chemistry in these environments. Our aim is to gain insight into the chemical intricacies of the star-formation process and circumstellar disc evolution.

We begin by describing the post-processing techniques that have been applied to the simulation data. This includes an overview of the foundational framework we use, an explanation of the modifications and considerations we have implemented, and a detailed explanation of how this technique operates at the code level.

Next, we provide some details about the heart of our work, which is the astrochemical package KROME. This section aims to provide an overview of the software architecture of KROME, the types of solvers it includes, how it evolves chemistry through rate equations, and the processes that can be incorporated into chemical networks.

In addition, this chapter introduces the reference model presented in Bate (2019), which we use as a foundation for the incorporation of chemistry. We begin by taking a look at the calculations presented in the study, the general considerations, and initial conditions. We then proceed to explain the data extracted from this work, with a particular focus on the physical conditions and characteristics of the selected subregion.

2.1 Chemical Post-Processing

Since the initial detection of molecules in the interstellar medium (ISM), there has been a significant increase of interest in astrochemistry. Currently, it is widely recognized that a comprehensive understanding of astrophysical phenomena requires an understanding of the chemical structure and evolution of any given system. However, incorporating self-consistent chemical evolution into theoretical models to better constrain processes in astronomical environments is a highly challenging task. Chemical reactions occur on very short time scales compared to other dynamic processes, they are strongly influenced by local properties such as density, temperature, and radiation flux, and can in turn also affect these quantities.

From a numerical perspective, accurately modeling the evolution of any system as a whole would require OTF, non-equilibrium chemistry in hydrodynamic simulations. Although this is feasible on galactic scales, the complexity of chemistry grows exponentially when simulating the smaller scales typical of prestellar cores and protoplanetary discs. During the initial stages of star formation, prestellar cores are distinguished by exceedingly high densities ($n_{H_2} \gtrsim 10^4\,\mathrm{cm}^{-3}$) and low temperatures ($T < 20$ K), with a well-defined chemical structure determined by characteristic chains of chemical reactions (Caselli and Ceccarelli, 2012; Öberg and Bergin, 2021). These conditions facilitate the adsorption of heavy species on the surfaces of dust grains, a process known as freeze-out (Bacmann et al., 2002, 2003; Tafalla et al., 2006), by leading to numerous gas-grain interactions and surface reactions, further increasing the chemical complexity of the said systems (van Dishoeck, 2018). Consequently, the number of reactions in chemical networks expands exponentially, making OTF calculations a highly expensive process.

In order to gain insight into the features and chemical complexities observed in star-forming regions, it is essential to include gas-grain interactions and surface chemistry in our models. A common approach is to construct low-dimensional models to qualitatively explore the different formation pathways of interstellar complex organic molecules or to perform sensitivity studies by mapping a large parameter space. However, to date, there have been no studies that have consistently followed the formation of COMs in three-dimensional simulations. In contrast, most available studies employ a post-processing approach, in which

the raw output of simulations is integrated with a non-equilibrium chemistry solver (Ruaud et al., 2018; Coutens et al., 2020). This method involves selecting a subset of resolution elements (particles) from standard simulations, which are performed without OTF chemistry, and subsequently integrating the chemical equations based on the pre-determined dynamical history of these particles. This approach allows researchers to investigate the influence of the physical parameters in different chemical networks on the evolution of specific tracers without the complications of doing it OTF.

In this study, we will employ the post-processing methodology outlined in Ferrada-Chamorro et al. (2021), which uses the chemical simulation package KROME to derive chemical abundances from a standard hydrodynamic simulation. The objective is to adapt and enhance this approach to meet our specific research needs, particularly by modifying the routines to accommodate Smoothed Particle Hydrodynamics simulation data from Bate (2019).

2.1.1 Base Framework

The post-processing method presented in Ferrada-Chamorro et al. (2021) operates under the assumption that chemistry does not significantly influence the dynamical evolution of the system. This assumption holds under the isothermal condition considered in their work. However, if the isothermal condition is relaxed, OTF chemistry with at least a minimal network is necessary to track the thermal evolution of the gas (e.g., Grassi et al., 2017).

The process begins with a standard magneto-hydrodynamic (MHD) simulation of the system, excluding chemical interactions. Outputs from this simulation are collected, storing the history of the system's dynamical properties. From this initial dataset, a random subset of particles ($N' = f_{\rm part} N$) is selected, where $f_{\rm part} \leq 1$ is a user-defined parameter representing the fraction of particles to be extracted.

Chemistry is then evolved for this subset (N') using the KROME package. A coarse integration time step ($\Delta t = m \Delta t_0$) is used, where (Δt_0) is the time interval between snapshots, and $m \geq 1$. During each integration step, the density of the particles is kept constant at the value obtained from the evolution history of the particle at the beginning of the step.

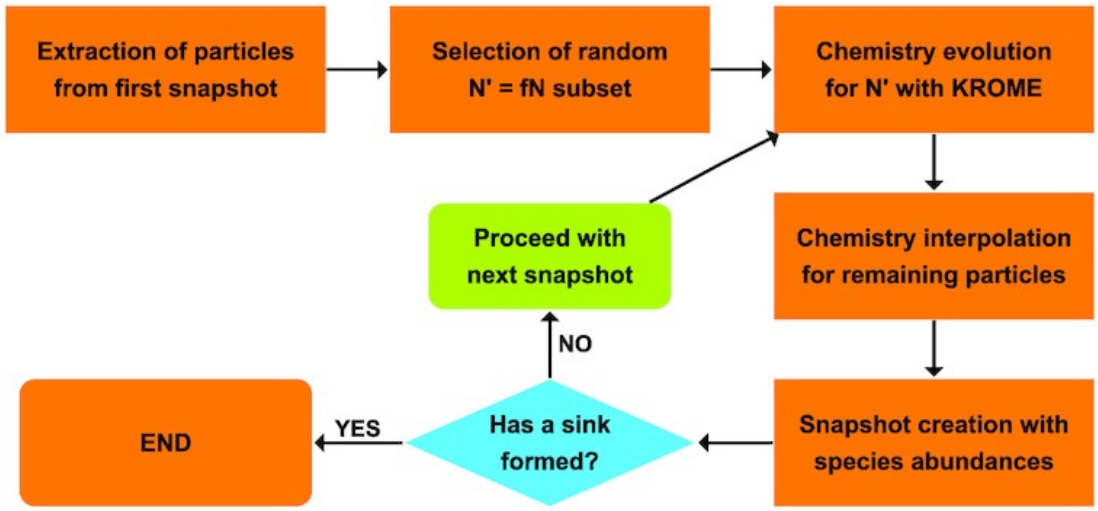

Figure 2.1.1: Schematic flowchart of the base post-processing method showing the different steps and filters to include chemistry in MHD simulations.
Source: Ferrada-Chamorro et al. (2021)

After evolving the chemistry for the (N') subset, species abundances for the remaining $(1 - f_{\text{part}})$ particles in the simulation are estimated. This is done by binning the post-processed particle subset based on density. For each non-evolved particle, the corresponding density bin is identified, and the spatially closest evolved particle in that bin is found. The species abundances from this evolved particle are then assigned to the target particle.

Fig. 2.1.1 shows a summarized scheme of the post-processing method.

2.1.2 Extraction of a sub-region from 3D simulations

In our case, we are employing a simplified version of the presented framework because we already possess a small subset of particles extracted from the original simulation for analysis. Therefore, we no longer need to consider the fraction of particles for our runs or implement an interpolation scheme for the chemistry of the remaining particles; this adaptation will allow the effective analysis and interpretation of the chemical evolution within this targeted astrophysical environment, thereby providing detailed insights into its dynamics and the interplay of chemical processes.

The selection of particles belonging to the subregion of interest is performed at the end of the calculation (Bate, 2019), ensuring that our region only comprises gas particles that have evolved up to the final step of the calculation. This removes

the concern of gas particles transitioning into sink particles or any loss of data. Our post-processing routines now exclusively focus on introducing chemistry into the data, focusing on the evolution of chemical species specified in the user-defined chemical network. This procedure is explained here and also summarized in Fig. 2.1.2:

- We begin by extracting crucial properties necessary to evolve the chemistry of each sampled particle from the data set. These properties encompass the total gas density $\rho_{\rm gas}$, gas temperature $T_{\rm gas}$, dust temperature $T_{\rm dust}$, the total extinction A_v and the snapshots time, all measured in CGS units. To ensure comprehensive analysis, we capture these parameters in all snapshots within the data set and meticulously store them in separate binary files. This systematic approach facilitates efficient data management and processing, laying the groundwork for applying chemical evolution routines to our selected particle sample;

- once the essential properties have been extracted from the dataset, the next step is to initialize the species abundances for each particle based on the values provided in Tab. 2.4.3. This table lists the initial abundances of various chemical species, which are essential to set the starting point of the chemical evolution in the simulations. By applying these initial values uniformly across the particle sample, a consistent baseline is established to track and analyze the evolution of chemical species over time. This initialization process ensures that our simulations start with accurate and predefined conditions, thus enabling robust investigations into the chemical dynamics within the studied astrophysical environment;

- subsequently, the chemical abundances for the particle set are evolved using the KROME package. Following the same procedure as in Ferrada-Chamorro et al. (2021) assuming a coarse integration time step $\Delta t = m\Delta t_0$. At each step, the particle density is kept constant at the value obtained from its evolutionary history at the beginning of the time-step;

- finally, the abundance values are stored at the end of each time step in a new output file, which contains all the species mass fractions. These stored abundances serve as the initial values for the subsequent time step. Repetition of this procedure for each time step allows the chemical

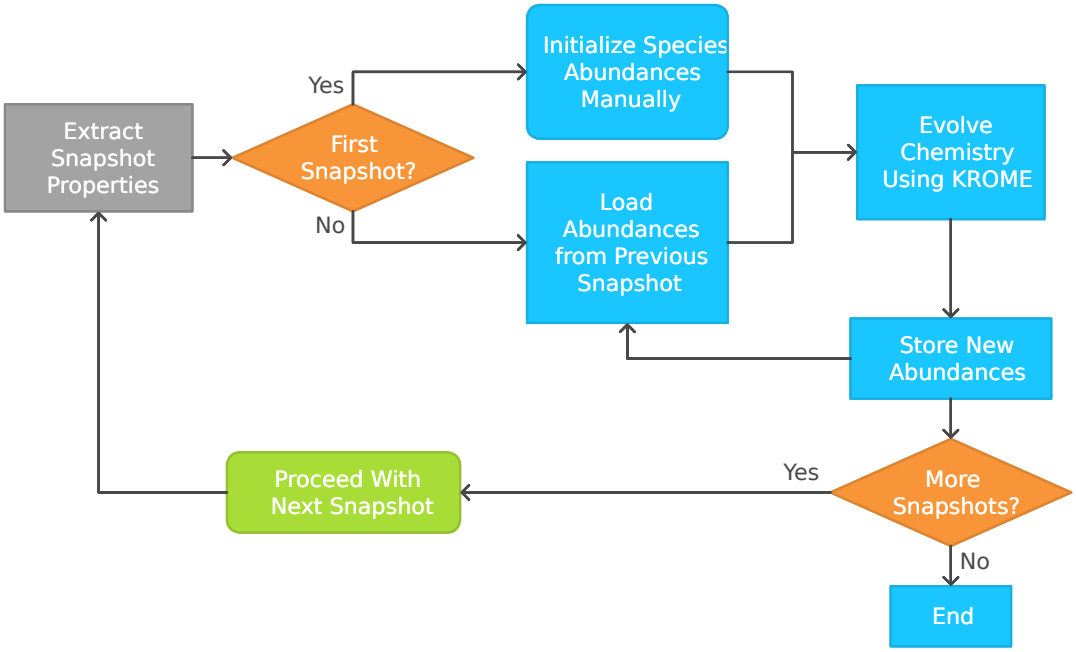

Figure 2.1.2: Post-process flowchart for our case following scheme presented.

abundances of the set of particles to evolve over time. Ultimately, this methodology allows us to generate new snapshot files for the simulation, which are now enriched with the abundances of network species from the chemical evolution simulations. The updated snapshot files provide a comprehensive view of the chemical evolution within the simulated astrophysical environment, facilitating detailed analysis and comparison with observational data or theoretical predictions.

2.2 The KROME Package

To incorporate complex chemistry into our post-processing framework, we used the non-equilibrium chemistry code KROME, an open source, GNU-licensed package designed to integrate microphysical processes into a wide spectrum of numerical models (Grassi et al., 2014). KROME's primary functionality lies in its ability to process a user-defined chemical network, formatted in a CSV-like structure, and subsequently generate the necessary subroutines to solve the associated chemical rate equations. This feature allows for flexible and accurate simulation of chemical reactions within astrophysical environments.

The KROME package includes a Python-based preprocessor that automatically

generates a FORTRAN framework to address the chemical rate equations, which are treated as a system of coupled ordinary differential equations (ODEs). This framework is particularly efficient at modeling the time-dependent evolution of both chemical abundances and thermal properties within a system. This flexibility is crucial for simulating the complex interplay between chemical and physical processes.

One of the significant advantages of KROME is its support for the inclusion of various thermal and chemical processes relevant to astrochemistry. These processes include cooling mechanisms involving endothermic reactions, radiative cooling of molecules and atoms, and heating processes due to photochemical reactions and exothermic chemical reactions (see Tab. 2.2.1). Furthermore, KROME provides a comprehensive dust grain model that accounts for the formation and destruction of grains, as well as the catalytic formation of molecular hydrogen on grain surfaces. The pre-processor facilitates the seamless integration of these processes into other simulation codes or post-processing frameworks.

KROME's computational core utilizes the high-order solver DLSODES (Hindmarsh, 1983), which is well suited for handling the sparse matrices characteristic of chemical networks in astrophysical simulations. DLSODES offers both accuracy and efficiency, often outperforming other solvers in terms of computational performance and reliability. This makes it an ideal choice for simulations that require precise modeling of complex chemical networks under different astrophysical conditions.

By integrating KROME into our post-processing framework, we exploit a powerful tool set to simulate the complex and dynamic processes that govern chemical evolution in astrophysical environments. The flexibility, accuracy, and computational efficiency provided by KROME significantly enhance our ability to model the intricate interplay of microphysical processes within molecular clouds, star-forming regions, and circumstellar discs. This capability is essential for advancing our understanding of the chemical complexity that arises in these environments and for improving the predictive power of our numerical simulations.

Table 2.2.1: List of the main processes for different environments. Note that this list is indicative and may depend on parameters other than temperature and density such as metallicity.

	T(K)	n(cm^{-3})	processes
HIM	$\gtrsim 3 \times 10^5$	~ 0.004	atomic cooling
HII	10^4	$0.3 - 10^4$	atomic and metal cooling, photoheating
WNM	$\sim 5 \times 10^3$	0.6	atomic and metal cooling, CR, photoheating, dust sputtering
CNM	~ 100	30	metal and H_2 cooling, dust growth
diff H_2	~ 50	~ 100	H_2 and metal cooling
dense H_2	$10 - 50$	$1 - 10^6$	CR and photoionisation/dissociation, H_2 and HD cooling, dust growth
cold dense	$\lesssim 10^2$	$10^6 - 10^{14}$	dust cooling, photoheating, chemical heating
warm collapsing	$\sim 10^3$	$> 10^{14}$	chemical cooling, H_2 cooling, chemical heating, CIE

Source: Grassi et al. (2014)

2.2.1 Rate Equations

The chemical evolution of species within KROME is governed by a system of ordinary differential equations (ODEs), representing a Cauchy problem where the solution is uniquely determined by the initial conditions of the system. The general form of the ODE for the number density of the ith species is:

$$\frac{dn_i}{dt} = \sum_{j \in F_i} \left(k_j \prod_{r \in R_j} n_r(j) \right) - \sum_{j \in D_i} \left(k_j \prod_{r \in R_j} n_r(j) \right) \tag{2.2.1}$$

Here, F_i represents the set of reactions that form the ith species, while D_i represents the reactions that destroy it. The jth reaction has a set of reactants (R_j), and the number density of each reactant at time t for the jth reaction is $n_r(j)$. The reaction rate coefficient (k_j), which has units of $cm^{3(n-1)}$ s^{-1}, with n the number of reactants in the jth reaction, is typically a function of the gas temperature, but can also depend on other parameters (e.g. the number densities of the reactants). Each species has an initial number density $n_i(t = 0)$, and KROME's aim is to find a solution after a given time interval Δt to obtain the updated set of number densities $n_i(t = \Delta t)$. The precise modeling of these rate equations within KROME ensures an accurate representation of the chemical dynamics within our astrophysical simulations.

2.2.2 Photoionization and Photodissociation

KROME incorporates photoionization and photodissociation processes in the following forms:

$$\begin{aligned} \mathrm{A} + h\nu &\rightarrow \mathrm{A}^+ + \mathrm{e}^- \\ \mathrm{A} + h\nu &\rightarrow \mathrm{B} + \mathrm{C} \end{aligned} \tag{2.2.2}$$

using a framework based on previous work by Glover and Abel (2008) and Grassi et al. (2012). The photoionization rate (in units of s^{-1}) is expressed as

$$R_{ph} = 4\pi \int_{E_t}^{\infty} \frac{I(E)\sigma(E)}{E} e^{-\tau(E)} dE \tag{2.2.3}$$

where E_t is the ionization potential, $I(E)$ is the energy distribution of the impinging photon flux, $\sigma(E)$ is the cross-section, and $\tau(E)$ is the optical depth of the gas. The term E is the energy in standard units of eV. This formulation allows for the accurate calculation of photoionization and photodissociation rates, which are crucial for modeling the chemical evolution of astrophysical environments exposed to high-energy radiation.

2.2.3 Cosmic-rays Processes

Cosmic-ray (CR) ionization and dissociation processes are another critical component modeled by KROME. The rate of CR-induced reactions in the form:

$$\begin{aligned} \mathrm{A} + \mathrm{CR} &\rightarrow \mathrm{A}^+ + \mathrm{e}^- + \mathrm{CR} \\ \mathrm{A} + \mathrm{CR} &\rightarrow \mathrm{B} + \mathrm{C} + \mathrm{CR}, \end{aligned} \tag{2.2.4}$$

is modeled using the rate approximation:

$$k_{CR} = \alpha\zeta \tag{2.2.5}$$

in units of s^{-1} where (ζ) represents the molecular hydrogen ionization rate and α is the value of the reaction rate at $\mathrm{T} = 300\,\mathrm{K}$.

2.2.4 Dust

KROME offers versatile methods for treating dust grains, including size-binned approaches and size-independent gas-dust reactions. For our study we use the solver-friendly freeze-out/evaporation method[1]. This method simplifies the modeling of dust-related processes by avoiding the need for explicit size binning, allowing the integration of gas-like reactions into the chemical network (detailed method in §2.4.2).

2.3 Reference Model

This study builds on the base model introduced in Bate (2019), more specifically the solar metallicity case. While detailed calculations and parameters are extensively documented therein, we provide a concise overview here for clarity.

The model comprises four radiation-hydrodynamical simulations investigating the formation of star clusters subsequent to the collapse of a molecular cloud. Each simulation explores different environments, with metallicity values ranging from 1/100, 1/10, 1, to 3 times solar metallicity. These simulations were conducted using a modified version of the smoothed particle hydrodynamics (SPH) code SPHNG (Benz, 1990; Benz et al., 1990), integrating methodologies from (Bate et al., 1995; Price and Monaghan, 2007; Whitehouse et al., 2005; Whitehouse and Bate, 2006).

The gravitational forces between the particles are calculated using a binary tree. The adaptive smoothing lengths are determined by the particle mass and density relationship, which is given by $h = 1.2(m/\rho)^{1/3}$, where m and ρ are the mass and density of the SPH particle, respectively (see Price and Monaghan, 2007). This ensures that the appropriate neighbor counts are maintained in regions of variable density.

In order to integrate the equations of motion, a second-order Runge-Kutta-Fehlberg method (Fehlberg, 1969) is employed, which strikes a balance between accuracy and computational efficiency. Furthermore, individual particle time-steps serve to improve efficiency by enabling independent evolution in regions that are dynamically diverse (Bate et al., 1995). Furthermore, the incorporation of

[1] https://bitbucket.org/tgrassi/krome/wiki/dust_bins

artificial viscosity, parameterized with variable coefficients, α_ν varying between 0.1 and 1 while $\beta_\nu = 2\alpha_\nu$ (see Price and Monaghan, 2005).

This comprehensive SPH framework enables robust and efficient simulations of intricate astrophysical phenomena, thereby contributing to deeper insights into star cluster formation within varying metallicity environments.

Fig. 2.3.1 shows a complete view of the solar metallicity case that we are using for this study.

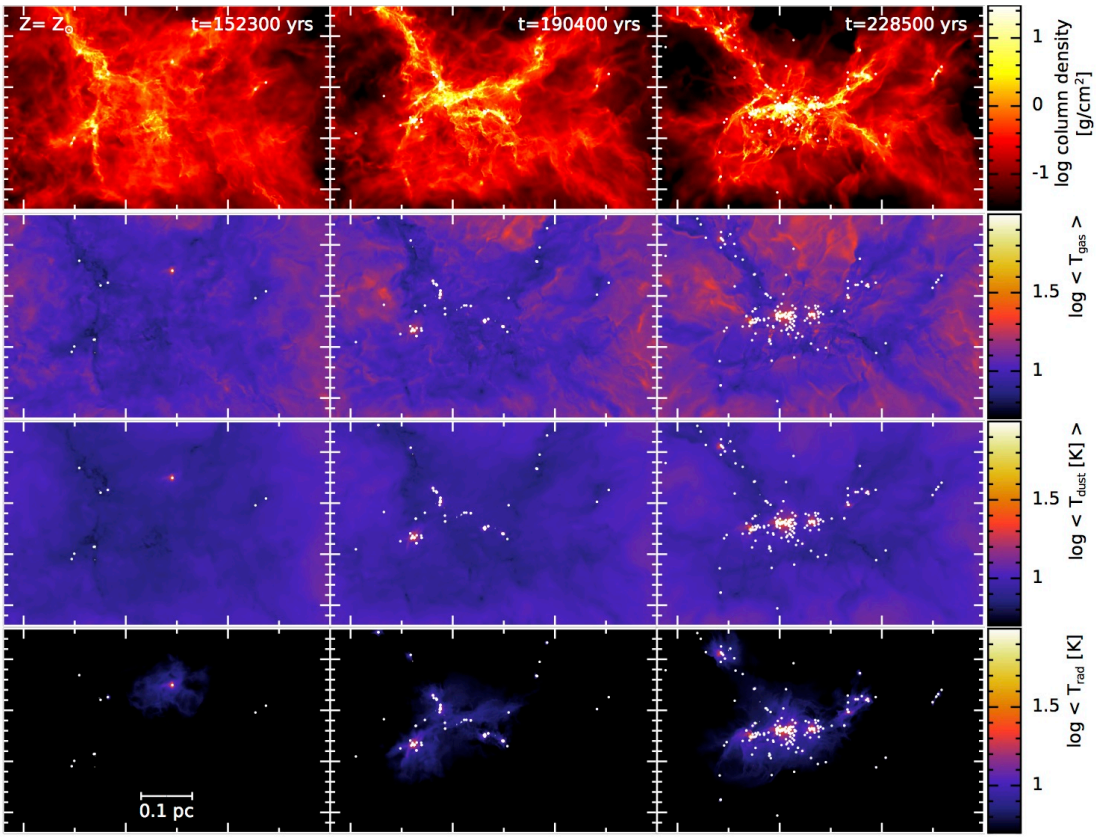

Figure 2.3.1: Column density and temperature snapshots at three different times ($t = 0.80, 1.00, 1.20\ t_{\rm ff}$) for the calculation with solar metallicity. From top to bottom, the rows give column density and the mass-weighted gas temperature, dust temperature, and protostellar radiation temperature. The colour scales are logarithmic. The column density scale covers $0.03 - 30$ g cm^{-3}, and the temperature scales cover $5 - 100$ K. The stars are plotted using white circles.
Source: Bate (2019)

2.3.1 Radiative transfer and diffuse ISM model

The primary distinction between this model and those previously developed by M. Bate (e.g., Bate, 2012) lies in the use of a novel radiative transfer and diffuse ISM method introduced by Bate and Keto (2015) for the handling of thermodynamics.

This innovative method integrates two distinct models: the flux-limited diffusion radiative transfer technique described by Whitehouse et al. (2005) and Whitehouse and Bate (2006), along with a diffuse ISM model similar to that of Glover and Clark (2012b), but using a simplified chemical model. This integration is crucial for accurately modeling the thermal evolution of the interstellar medium (ISM). Consequently, the model incorporates separate temperature treatments for gas, dust, and radiation fields.

The gas component encompasses various heating and cooling mechanisms. Heating mechanisms include:

- Cosmic ray heating through direct collisions with gas particles.
- Indirect gas heating via photoelectric emission of hot electrons from dust grains, stimulated by photons from the interstellar radiation field (ISRF).
- Heating through the formation of molecular hydrogen in dust grains.

The cooling mechanisms for the gas include:

- Electron recombination.
- Fine-structure cooling of atomic oxygen and carbon.
- Molecular line cooling.

The dust temperature is determined by assuming that the dust is in local thermodynamic equilibrium with the total radiation field, which also accounts for the collisional exchange of thermal energy between gas and dust. The dust-gas collisional energy transfer rates used in the calculations are derived from Hollenbach and McKee (1989), as also used in Glover and Clark (2012a).

The chemical model used here specifically addresses the evolution of hydrogen and carbon. The abundances of C^+, neutral carbon, CO, and the depletion of CO on dust grains are calculated using the framework proposed by Keto and Caselli (2008). For hydrogen, the model evolves the abundances of atomic and molecular

hydrogen using the formation and dissociation rates of molecular hydrogen from Glover et al. (2010). Due to the absence of an explicit chemical model for oxygen, the abundance of atomic oxygen is estimated assuming that it scales proportionally to $(1 - \mathrm{n(CO)/n(C)})$.

2.3.2 Initial conditions

The initial conditions for all four calculations are as follows: Bate (2019) begin with a uniform density spherical cloud of gas, having a radius of 0.404 pc and containing 500 $\mathrm{M}_\odot$ of gas. The initial density imposed is $1.2 \times 10^{-19}\,\mathrm{g\,cm^{-3}}$ (hydrogen number density $n_\mathrm{H} = 6 \times 10^4\,\mathrm{cm^{-3}}$). The initial free-fall time of the gas is $t_\mathrm{ff} = 1.90 \times 10^5$ years. Although the cloud initially has a uniform density, an initial supersonic "turbulent" velocity field is imposed with an initial root-mean-square Mach number $\mathcal{M} = 13.7$ at 10 K, following the method of Ostriker et al. (2001) and Bate et al. (2003). The velocity field is a divergence-free random Gaussian with a power spectrum $P(k) \propto k^{-4}$, where k is the wavenumber. This is implemented on a 128^3 uniform grid with particle velocities interpolated from the grid.

For each calculation, the dust is initially in thermal equilibrium with the local interstellar radiation field (ISRF), and the gas is in thermal equilibrium with heating from the ISRF and cosmic rays, with cooling provided by atomic and molecular line emission and collisional coupling with the dust. This results in a range of initial temperatures for the gas and dust, with dust being warmest on the outside of the cloud and coolest at the center. Specifically, for the case selected with $Z = Z_\odot$, the dust temperature ranges from 7.1 K to 17 K, and the gas temperature ranges from 9.1 K to 9.8 K.

All clouds are modeled using 3.5×10^7 SPH particles, providing sufficient resolution to resolve the local Jeans mass throughout the calculation, which is necessary to correctly model fragmentation down to the opacity limit (Bate and Burkert, 1997; Truelove et al., 1997; Whitworth, 1998; Boss et al., 2000; Hubber et al., 2006). Each calculation is run up to $1.20 t_\mathrm{ff}$, tracking the hydrodynamic collapse of the protostars formed during the simulations.

2.3.3 Sink particles

In all calculations, the protostellar collapse is traced through to the second collapse phase, which is induced by the dissociation of molecular hydrogen (Larson, 1969). Sink particles (see Bate et al., 1995) are introduced when the gas density exceeds $10^{-5}\,\mathrm{g\,cm^{-3}}$. At this point, all SPH particles within an accretion radius, $r_{acc} = 0.5\,\mathrm{AU}$, of the densest particle are replaced by a single sink particle that conserves the combined mass and momentum of the original particles. If an SPH particle approaches within r_{acc}, is gravitationally bound, and has a specific angular momentum lower than that required for a circular orbit at r_{acc}, it is accreted by the sink particle. This means that matter around the sinks can only be resolved above approximately 1 AU diameter. The angular momentum of the accreted particles is utilized to calculate the spin of the sink particles, although this spin does not influence the overall dynamics of the simulation. The sink particles in this model do not contribute to radiative feedback, which is a significant limitation discussed in detail by Bate (2012). Additionally, sink particles are programmed to merge if they pass within 0.03 AU of each other, ensuring that close encounters result in the formation of a single, larger sink particle.

2.4 Chemical Network

Our chemical network has been specifically designed to study relevant $\mathrm{H-C-O}$ bearing species in physical conditions analogous to those present in nearby giant molecular clouds (GMCs) including relevant surface reactions to explore the role of dust inside the discs chemistry.

2.4.1 Gas-phase chemistry

To ensure the precision and reliability of our model, we adopt reaction rates similar to those detailed in Grassi et al. (2017) to explore gas phase reactions in our region. These reactions include photodissociation and photoionization processes due to UV photons emitted by stars, ionization and dissociation by direct collisions with cosmic rays, bimolecular reactions (e.g., $\mathrm{A + B \rightarrow C + D}$), charge transfer reactions (e.g., $\mathrm{A^+ + B \rightarrow A + B^+}$), associative detachment (e.g., $\mathrm{A^- + B \rightarrow AB + e^-}$), electron recombination and attachment (e.g., $\mathrm{AB^+ + e^- \rightarrow A + B}$), and three-body associations.

2.4.2 Grains-related Chemistry

Furthermore, our network incorporates processes at the interface gas-dust occurring on the surface to simulate the role of dust grains in these environments. This inclusion is crucial for modeling regions close to circumstellar discs, where dust surface chemistry significantly impacts the formation and evolution of molecular species.

We included different solid-phase reactions into the network in order to simulate different reactions in silicon-based (silicate) grains to model the dust component.

2.4.2.1 Adsorption onto dust grains

The freeze-out of particles into dust grains is computed following the model presented in Hollenbach and McKee (1979)

$$k_i^{ads} = v_i^{th} f_d S \tag{2.4.1}$$

here $v_i^{th} = \sqrt{8k_B T_g/\pi m_i}$ is the thermal velocity of the ith specie in gas phase with mass m_i, k_B the Boltzmann constant and T_g the gas temperature, S is the sticking coefficient defined as

$$S = \left(1 + 4 \times 10^{-2}\sqrt{T_g + T_d} + 2 \times 10^{-3} T_g + 8 \times 10^{-6} T_g^2\right)^{-1} \tag{2.4.2}$$

and f_d is a scaling factor that takes into account the grain size distribution

$$f_d = \frac{\rho_d}{4/3\rho_0} \cdot \frac{a_{max}^{p+3} - a_{min}^{p+3}}{a_{max}^{p+4} - a_{min}^{p+4}} \cdot \frac{p+4}{p+3} \tag{2.4.3}$$

where ρ_d is the total dust mass density, we consider dust grains to be silicates with a typical specific density $\rho_0 = 3\,\mathrm{g\,cm^{-3}}$ and a dust-to-gas mass ratio $\mathcal{D} = 0.01$, $a_{min} = 5 \times 10^{-7}\,\mathrm{cm}$ and $a_{max} = 2.5 \times 10^{-5}\,\mathrm{cm}$ are the boundaries of the dust size distribution radii, assuming a power-law distribution, i.e. $\varphi(a) \propto a^p$ (Mathis et al., 1977) with a $p = -3.5$ exponent.

Table 2.4.1: $T_{b,X}$ values for the substrates bare grain.

Species	$T_{b,X}$ [K]	Species	$T_{b,X}$ [K]
H	500	H_2	300
O	1700	OH	1360
CO	1100	HCO	1100
H_2O	4800	O_2	1250
CO_2	2300	HO_2	4000
H_2CO	1100	CH_3O	1100
CH_3OH	1100	H_2O_2	6000
O_3	2100		

Source: Hocuk and Cazaux (2015)

2.4.2.2 Two-body reactions on dust grains

Species adsorbed onto dust grains can move around the dust grains surface, i.e. thermal diffusion, and react with other species attached to the grains. These reactions depend on the dust temperature and the diffusion energy (usually a fraction of the binding energy) of the species to the grains, the binding energies for the main species that go through adsorption/desorption processes are taken from Hocuk and Cazaux (2015) and reported in Tab. 2.4.1. Also, it is necessary to account for reaction barriers, where if the reaction barrier is high enough, it is necessary to consider tunneling effects. The probability of overcoming these reaction barriers by quantum tunneling is given by

$$P_{reac} = \exp\left(-\frac{2a}{\hbar}\sqrt{2m_{red}k_B E_a}\right) \tag{2.4.4}$$

where $a = 1\,\text{Å}$, $\hbar$ is the reduced Planck constant, m_{red} is the reduced mass of the reactants $m_{red} = (m_i m_j)/(m_i + m_j)$, k_B is Boltzmann constant and E_a is the activation energy of the barrier for the reaction to occur. The activation energies for our framework were obtained from the Kinetic Database for Astrochemistry (KiDA; Wakelam et al., 2012) and reported in Tab. 2.4.2. Therefore, surface reactions between species i and j are determined by the thermal hopping of the molecules on the surface of grains, following the framework described in Semenov et al. (2010) accounting for the dust grain size distribution

Table 2.4.2: Surface two-body reactions present in the network and their corresponding activation energies.

Reactants		Products	E_a	Reactants		Products	E_a
$\perp$ H + $\perp$ H	→	H_2	0	$\perp$ H + $\perp$ O	→	$\perp$ OH	0
$\perp$ H + $\perp$ OH	→	$\perp$ H_2O	0	$\perp$ H + $\perp$ O_2	→	$\perp$ HO_2	1200
$\perp$ H + $\perp$ CO	→	$\perp$ HCO	2500	$\perp$ H + $\perp$ HCO	→	$\perp$ H_2CO	0
$\perp$ H + $\perp$ H_2CO	→	$\perp$ CH_3O	2200	$\perp$ O + $\perp$ O	→	$\perp$ O2	0
$\perp$ O + $\perp$ CO	→	$\perp$ CO_2	1000	$\perp$ H + $\perp$ CH_3O	→	$\perp$ CH_3OH	0
$\perp$ O + $\perp$ O_2	→	$\perp$ O_3	0	$\perp$ OH + $\perp$ OH	→	$\perp$ H_2O_2	0
$\perp$ H + $\perp$ CH	→	$\perp$ CH_2	0	$\perp$ H + $\perp$ CH_2	→	$\perp$ CH_3	0
$\perp$ O + $\perp$ CH_3	→	$\perp$ CH_3O	0	$\perp$ OH + $\perp$ CH_2	→	$\perp$ CH_3O	0
$\perp$ OH + $\perp$ CH_3	→	$\perp$ CH_3OH	0	$\perp$ C + $\perp$ O	→	$\perp$ CO	0
$\perp$ C + $\perp$ H	→	$\perp$ CH	0	$\perp$ H + $\perp$ H_2CO	→	$\perp$ H_2+ $\perp$ HCO	1740
$\perp$ H + $\perp$ O_3	→	$\perp$ OH+ $\perp$ O_2	0	$\perp$ H + $\perp$ H_2O_2	→	$\perp$ OH+ $\perp$ H_2O	1400
$\perp$ O + $\perp$ HO_2	→	$\perp$ O_2+ $\perp$ OH	0	$\perp$ O + $\perp$ HCO	→	$\perp$ CO_2+ $\perp$ H	0
$\perp$ OH + $\perp$ H_2	→	$\perp$ H+ $\perp$ H_2O	2100	$\perp$ OH + $\perp$ CO	→	$\perp$ CO_2+ $\perp$ H	120
$\perp$ C + $\perp$ OH	→	$\perp$ CO+ $\perp$ H	0	$\perp$ C + $\perp$ O_2	→	$\perp$ CO+ $\perp$ O	0
$\perp$ H + $\perp$ H_2O	→	$\perp$ OH+ $\perp$ H_2	0	$\perp$ H + $\perp$ HO_2	→	$\perp$ OH+ $\perp$ OH	0
$\perp$ H + $\perp$ HCO	→	$\perp$ CO+ $\perp$ H_2	0	$\perp$ H + $\perp$ CO_2	→	$\perp$ CO+ $\perp$ OH	0
$\perp$ O + $\perp$ O_3	→	$\perp$ O_2+ $\perp$ O_2	0	$\perp$ O + $\perp$ H_2	→	$\perp$ H+ $\perp$ OH	0
$\perp$ O + $\perp$ OH	→	$\perp$ O_2+ $\perp$ H	0	$\perp$ O + $\perp$ H_2CO	→	$\perp$ CO_2+ $\perp$ H_2	0
$\perp$ OH + $\perp$ HCO	→	$\perp$ CO_2+ $\perp$ H_2	0	$\perp$ HO_2 + $\perp$ H_2	→	$\perp$ H+ $\perp$ H_2O_2	0

Note: The notation $\perp$ represents a species that is bound on the surface of a dust grain.

$$k_{i,j}^{2body} = \nu_0 \left[\exp\left(-\frac{2}{3} \frac{T_{b,i}}{T_d} \right) + \exp\left(-\frac{2}{3} \frac{T_{b,j}}{T_d} \right) \right] \tag{2.4.5}$$

$$R_{i,j}^{2body} = \frac{n_{x_i} n_{x_j}}{n_d n_{sites}} P_{reac} k_{i,j}^{2body} \tag{2.4.6}$$

with $k_{i,j}^{2body}$ the two-body diffusion rate coefficient of species on the surface of grains assumed to occur with a barrier of 2/3 of the binding energies, where ν_0 is the harmonic oscillator frequency (typically $10^{12}\,\mathrm{s}^{-1}$), $E_{b,X} = k_\mathrm{B} T_{b,X}$ is the binding energy of specie X on the grain site, and T_d is the dust temperature. $R_{i,j}^{2body}$ is the two-body reaction rate in $\mathrm{cm}^{-3}\,\mathrm{s}^{-1}$, and $n_d n_{sites}$ represents the total number of potential attachment sites on grain surfaces per cubic centimeter of space, defined in our case as

$$n_d n_{sites} = \frac{f_d}{a_{pp}^2} \tag{2.4.7}$$

where f_d is the scaling factor presented in (2.4.3) and a_{pp} is the typical separation

between two adsorption sites on grain surfaces, assumed to be 3 Å.

2.4.2.3 Thermal desorption

Species can also evaporate from dust grains back to the gas phase. For that we employ a thermal desorption rate, which can be very effective in regions near the stars and the surface of discs. This rate depends exponentially on the binding energies of the species and the dust temperature. These binding energies differ according to the species and type of substrate, as we are only considering bare grain surfaces, we use the thermal desorption rate based on Hasegawa and Herbst (1993) for fully bare dust grains

$$k_i^{des,th} = \nu_0 \exp\left(-\frac{T_{b,i}}{T_d}\right) \tag{2.4.8}$$

with ν_0 the harmonic oscillator frequency, $E_{b,X} = k_B T_{b,X}$ the binding energy of specie X on the grain site, and T_d the dust temperature.

2.4.2.4 Cosmic ray desorption

Other type of desorption of elements from dust grains is cosmic ray induced desorption. Cosmic ray processes are usually inefficient destruction mechanisms in diffuse atmospheres, but can dominate destruction rates inside dense regions like the midplane of circumstellar discs. To include them we use a non-thermal cosmic ray induced desorption model following (Hasegawa and Herbst, 1993)

$$k_i^{des,cr} = \frac{\int_{70\,\mathrm{K}}^{10\,\mathrm{K}} k_i^{des,th}[dt/dT_d]dT_d}{\int_{70\,\mathrm{K}}^{10\,\mathrm{K}}[dt/dT_d]dT_d} \tag{2.4.9}$$

where $k_i^{des,th}$ is given by (2.4.8) and the cooling time of grains as a function of time t is described by the function $T_d(t)$.

By assuming that most of the cosmic ray induced desorption occurs near 70 K (see Hasegawa and Herbst, 1993) this expression simplifies to

$$k_i^{des,cr} = f(70\,\mathrm{K}) k_i^{des,th}(70\,\mathrm{K}) \tag{2.4.10}$$

where $f(70\,\mathrm{K})$ is the fraction of the time spent by grains in the vicinity of 70 K

Table 2.4.3: Fiducial initial abundances

Species	Mass Fraction
H_2	7.11×10^{-1}
He	2.84×10^{-1}
H_3^+	3.84×10^{-4}
O	1.54×10^{-3}
CO	2.39×10^{-3}
X_i^*	10^{-20}

* Rest of the other species initial abundance

$$f(70\,\mathrm{K}) = \left(\frac{\zeta_{cr}}{1.3 \times 10^{-17}\,\mathrm{s}^{-1}}\right) 3.16 \times 10^{-19} \tag{2.4.11}$$

2.4.2.5 Resulting network

Taking all these considerations into account, our remaining chemical network consists of a total of 364 reactions between 65 species that model the formation and destruction of CO and H_2 and explore the formation processes of complex molecules (e.g., CH_3OH, H_2CO) in sites where physical conditions match those found in nearby giant molecular clouds. To initialize this network, we assume a fully molecular state of the initial cloud. Tab. 2.4.3 reports the fiducial initial abundances used in the post-processing run.

Chapter 3

Results

The following section presents the results obtained from the post-processing analysis of the data. The main aim of this method is to integrate complex chemistry into the simulations to further explore the impact of different environmental (e.g., temperature, density, extinction) factors on chemistry and to analyze how different molecular species evolve in the discs.

The inclusion of post-processed chemistry allows for a deeper understanding of how molecules form and react in the conditions modeled by the simulation, particularly in the context of star-forming regions and inside circumstellar type 0/I discs.

Fig. 3.1.3 shows the different discs extracted from the last snapshot at $t = 1.20t_{\rm ff}$ using the extraction scheme presented in §3.1.1. At this time, we are dealing with different types of discs and also hosted by different types of stellar systems.

3.1 The extracted region

In order to investigate the chemical processes in protostellar environments, we selected a small portion of the original dataset (from the solar metallicity scenario outlined in section 2.3). Fig. 3.1.1 presents an initial view of the extracted area by displaying a map of the entire, then zooming in to the extracted region within the raw data. The extraction process consists of identifying the region of interest in the final snapshot, selecting all the particles within it, and extracting their IDs. By tracking these particles throughout the entire snapshot set, we were able to reconstruct the temporal evolution of the region and store the relevant data in a

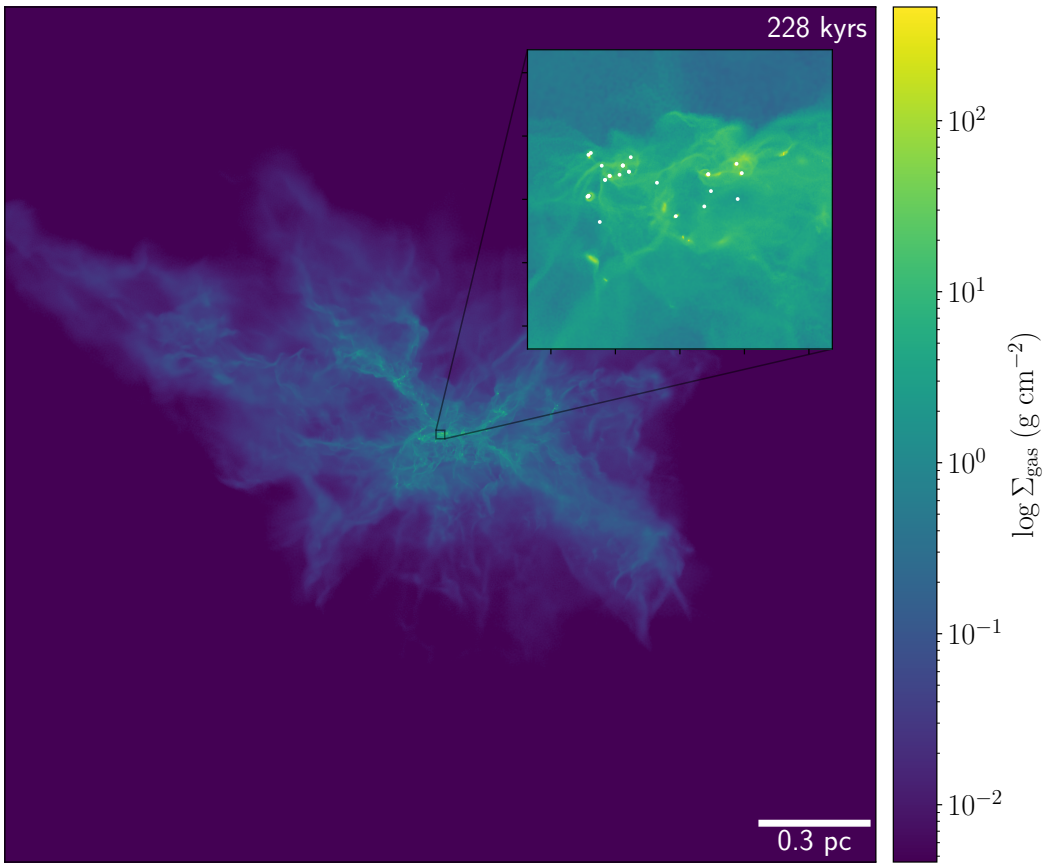

Figure 3.1.1: Surface density maps of the cloud and the selected region at the end of the simulation ($t = 1.20 t_{\rm ff}$). Sink particles are plotted in the zoomed region using white dots (the size of the sinks is not proportional to their properties). The data is extracted from the raw outputs.

new file containing only the particles selected in the last snapshot. This method ensured that no data are lost due to particles moving out of the region or sink particles accreting gas particles.

This subregion covers approximately 1% of the total SPH particles and contains 27 sink particles (stars), resulting in an approximate mass of 30 $M_\odot$. Fig. 3.1.2 illustrates surface density, dust and gas temperature maps of the extracted subregion from the last time step of the simulation ($t = 1.20\, t_{\rm ff} = 228\,$kyrs), with white dots representing stars.

Notably, several disc structures already formed within the selected region, indicative of ongoing star formation. The selection of this subregion allows for

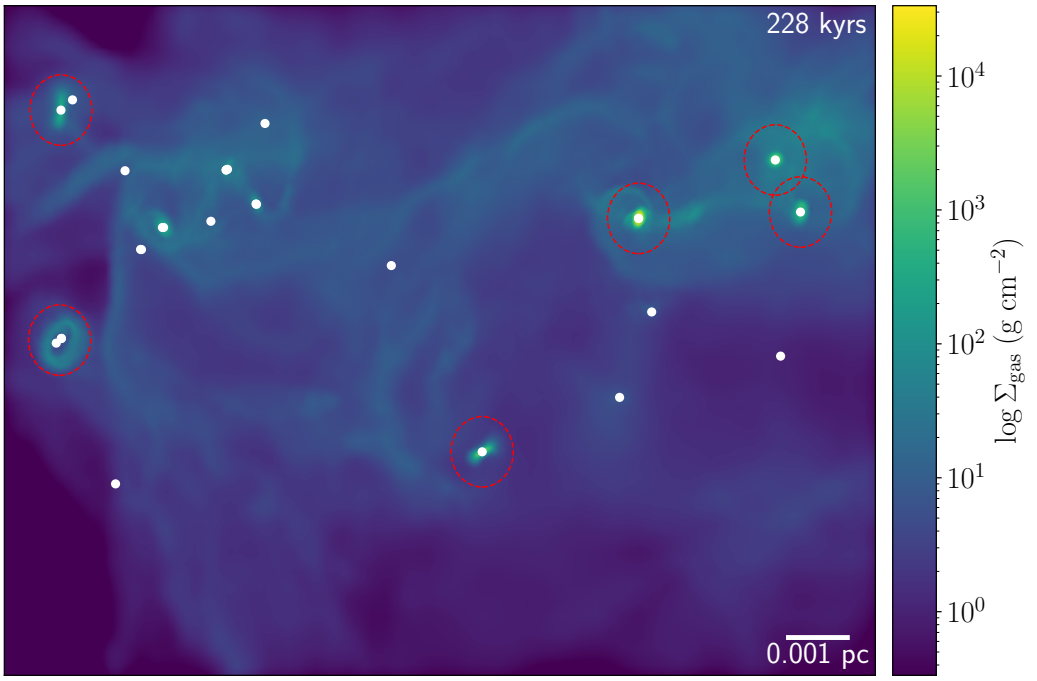

Figure 3.1.2: Surface density map for the extracted sub-region at $t = 1.20\,t_{\rm ff}$. The surface density scale covers $0.3 - 3 \times 10^4\,{\rm g\,cm^{-2}}$. White dots represent stars. Red dashed outlines indicate the locations of the discs formed in the region.

a detailed examination of the chemical complexity and dynamics in a controlled environment, providing valuable insights into the interactions and evolution of matter in a star-forming region.

3.1.1 discs

As previously discussed, various disc-shaped structures are formed in this specific region. These structures are crucial for our study as we analyze the evolution of chemistry in circumstellar discs. Therefore, it is essential to accurately extract the disc particles to examine their properties. We follow a method similar to that described by Bate (2018).

Initially, we extract a 2000 AU spherical region around a selected sink particle. If another sink particle is found within this region, we reduce the radius to the distance of the closest sink and record the companion's ID. With the selected region defined, we calculate the instantaneous ballistic orbit of each SPH gas particle inside it. Particles with an apastron less than 2000 AU and an eccentricity

$e < 0.3$ are considered part of the disc. We then calculate the center of mass of this distribution.

To differentiate the disc from the envelope, we exclude any circumstellar disc with a mass less than $0.03\,M_\odot$ (i.e., $<$ 2100 SPH particles) and size, defined by the radius enclosing 63% of the total disc mass, larger than 300 AU. Additionally, we exclude discs where the radius containing 63% of the disc's mass is more than three times the half-mass radius.

After this filtering procedure, we focus on the circum-multiple discs. After the protostars and some part of their surrounding "circumstellar disc" have been identified, we group these sinks as nodes, and we search for the pair of nodes that have the lowest total energy ($E_k + E_p$) that are also mutual nearest neighbors (distance between sinks $< 2000\,\mathrm{AU}$). This pair is then grouped into a new node, sinks information is removed from the nodes list, and a new node is created containing their ID's and their center of mass information. For our study, we only consider single, binary, triple and quadruple systems at most, as high-order systems are unstable.

The method for extracting the disc of a multiple system is similar to that for extracting a circumstellar disc. SPH particles (and sink particles) are sorted based on their distance from the node's center of mass. Starting with the closest particle, the particle is considered part of the circum-multiple disc if it has not been assigned to any disc, and if its instantaneous ballistic orbit around the node (calculated using its center of mass location and velocity) has an apastron distance less than 2000 AU and an eccentricity ($e < 0.3$). If these criteria are met, the particle's mass is added to the circum-multiple disc of the node, and the node's total mass, as well as its center of mass position and velocity, are updated. This process is repeated for the next SPH particle up to a distance of 2000 AU. If a sink particle not belonging to the node is encountered, the disc extraction is terminated.

Once the circum-multiple disc of the new node has been extracted, the process is repeated for the list of active nodes until no pairs of nodes have negative total energy and are mutual nearest neighbors. The final list of protostellar systems is compiled by traversing the list of all nodes from the highest-order system to the lowest, writing out data only for nodes containing four or fewer protostars and

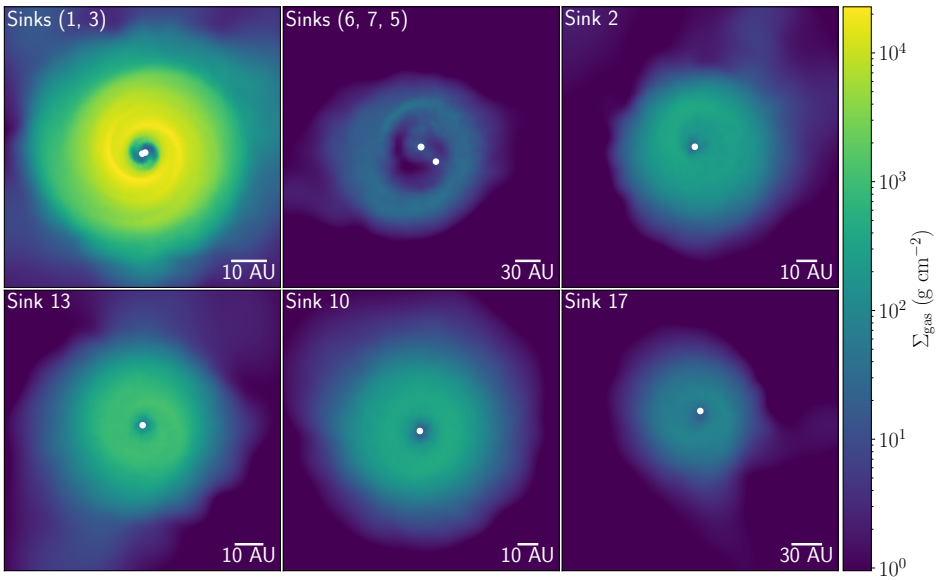

Figure 3.1.3: Face-on logarithmic surface density maps for all the circumstellar disc-like structures formed at $t = 1.20\,t_{\rm ff}$. The maps are sorted by mass of the resultant circumstellar disc structure + sink(s) mass(es) (i.e., top-left map is the most massive system and bottom-right map is the less massive.). The color scale is logarithmic. White dots mark the sink particles position. Sink particles are numbered in order of their formation.

whose components have not been previously documented (e.g., a triple system is not documented if it is part of a quadruple system, and a binary system is not documented if it is part of a triple or quadruple system).

Fig. 3.1.3 shows the extracted discs using the aforementioned method. These will be our main area of interest, as these discs are the regions in which we will be able to find a more diverse chemistry because of their varying physical conditions (see Tab. 3.1.1 to see the general properties of the extracted discs).

3.1.2 Disc Characterization

Tab. 3.1.1 presents a list of the physical properties of each disc, where $M_{\rm tot}$, n_{part} and $r_{extent,max}$ are properties extracted after using the disc extraction method discussed in the previous section, r_c and Σ_c are the characteristic radius and surface density at r_c obtained by fitting power-law radial surface density profiles. This is often adapted by assuming a truncated power-law surface density profile (e.g., Andrews et al., 2010; Tazzari et al., 2017)

Table 3.1.1: Physical properties for the identified discs in the simulation.

Disc	Hosting Sink(s)	Sink(s) Age(s) (kyrs)	$M_{\rm tot}$ ($M_\odot$)	r_c (AU)	Σ_c (g cm^{-2})	n_{part}	$r_{extent,max}$ (AU)
1	1,3	75.2, 70.1	6.623	13.84	2.80×10^4	102590	334.495
2	6,7,5	44.7, 42.4, 44.8	3.273	51.76	2.85×10^1	2473	418.551
3	2	71.3	1.807	24.98	5.36×10^2	6025	499.715
4	13	21.2	0.941	15.10	2.16×10^3	9936	621.068
5	10	20.8	0.686	23.84	8.28×10^2	8196	385.412
6	17	16.1	0.246	46.00	7.84×10^1	3105	161.021

Note: r_c and Σ_c are characteristic properties calculated following the procedure presented in §3.1.2.

$$\Sigma(r) = \Sigma_c \left(\frac{r}{r_c}\right)^{-\gamma} \exp\left[-\left(\frac{r}{r_c}\right)^{2-\gamma}\right], \tag{3.1.1}$$

where r_c is the characteristic or cut-off radius of the disc and γ is the power-law radial density profile in the bulk of the disc (see Bate, 2018, for more information).

Eq. (3.1.1) only gives sensible profiles for $\gamma < 2$, as for values greater than two the profiles show a central cavity and flattens at large radii, hence the mass diverges. For $\gamma = 2$, the exponential term becomes unity, so the density profile becomes a pure power law (and thus the disc mass never converges).

For $\gamma < 2$, the characteristic radius, r_c, is interestingly always equal to the radius containing a fraction $(1 - 1/e)$ of the total mass of the disc (i.e., 63.2% of the total disc mass). Therefore, if the disc is well fitted by the equation, the characteristic radius can be simply obtained by measuring the radius containing 63.2% of the total disc mass. Even measuring this radius alone provides accurate results for the characteristic radius, even for discs that have very different surface density profiles, it will still give a robust measure for r_c.

This method is particularly effective for analyzing single systems, allowing us to determine key characteristic properties of the discs. However, for circumbinary discs and higher order systems (e.g., triple or quadruple systems) it is necessary to account for additional interactions between the systems and the disc. In the case of circumbinary discs it is essential to consider the continuous exchange of angular momentum between the binary system and the surrounding disc. As the binary system orbits with a period shorter than that of the material in the disc,

it generates waves of positive angular momentum within the disc, transferring both energy and angular momentum to it. This continuous transfer of angular momentum causes the inner region of the disc to accelerate, making the material migrates outwards. Consequently, a low-density region, called inner gap, forms around the binary system.

To consider this inner gap region in the disc it is necessary to employ a modified version of Equation (3.1.1) accounting for the cavity created by the binary-disc interaction (Günther and Kley, 2002)

$$\Sigma_{bin}(r) = f_{gap}\Sigma(r) \tag{3.1.2}$$

with f_{gap} the gap function that characterizes the cavity created by the binary interaction with the disc defined as

$$f_{gap} = \left[1 + \exp\left(-\frac{r - r_{gap}}{0.1 r_{gap}}\right)\right]^{-1} \tag{3.1.3}$$

with r_{gap} the estimated size of the gap (Artymowicz and Lubow, 1994). Fig. 3.1.4 shows the best fit for each disc present in the last snapshot along with their characteristic properties. We can see that the majority of the discs present in the region are well fitted by this profile, and therefore we can extract their characteristic properties by measuring the radius containing 63.2% of the total disc mass[1].

3.2 Analysis of physical properties in discs

For each disc, we decided to explore the vertical structure and the distribution of each species and its dust component. The analysis of the physical structure of the discs was performed using post-processed data from the simulations with incorporated chemistry. Vertical structure maps were generated for key physical parameters, i.e., gas density (ρ), gas temperature (T_{gas}), dust temperature ($T_{\rm dust}$), and visual extinction (A_v), to highlight their distribution and gradients across the discs. This will allow us to further explore possible interactions between these properties and the chemistry happening inside the discs by comparing this with

[1]The total mass of the extracted gas particles

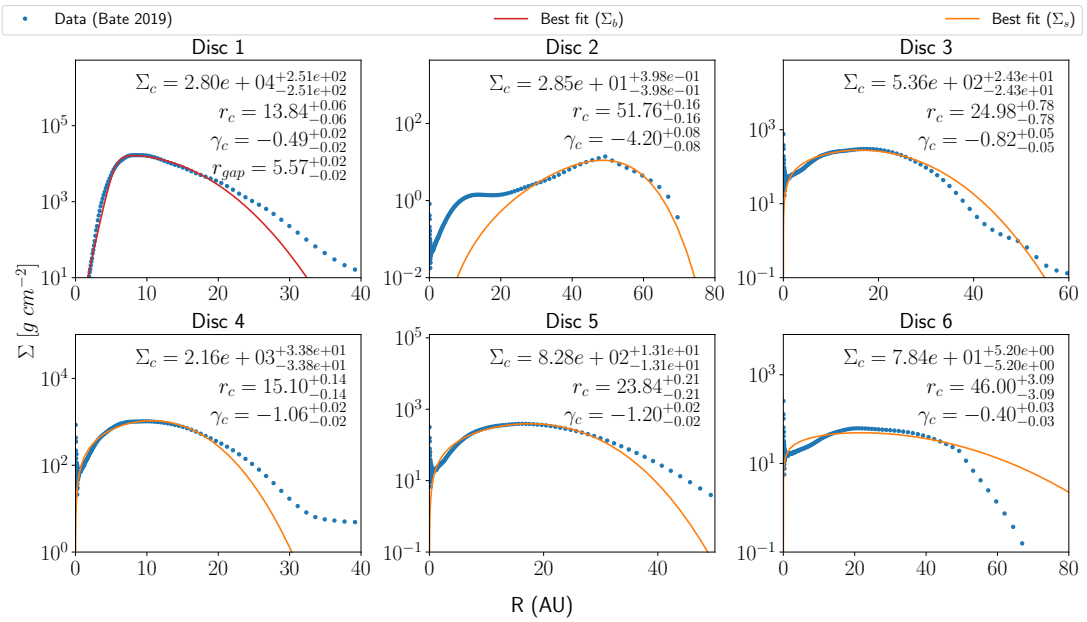

Figure 3.1.4: Radial surface density profile for each disc. Solid lines represent the best fit using a non linear least squares model to fit the parameters (Σ_c, r_c and γ). Red line represents the method used for binary systems (Σ_b), while orange line corresponds to the method applied to single sink systems and systems with more than two stars (Σ_s).

the vertical distribution of chemical species. Figures 3.2.1, 3.2.2 and 3.2.3 show the physical structure of three different discs in the last stage of the simulation.

The gas density in the discs exhibits a gradient distribution that gradually decreases towards the discs surface and the outer parts of the discs, with higher densities near the midplane ($z = 0\,\mathrm{AU}$) reaching values up to $10^{-10}\,\mathrm{g\,cm^{-3}}$ in the densest region. This distribution is consistent with theoretical predictions of vertical hydrostatic equilibrium in discs.

The high densities in the midplane play a significant role in shielding molecules from ultraviolet (UV) radiation, facilitating complex chemical processes. The gas and dust temperatures show different spatial distributions, decreasing radially. Temperatures reach $10^4\,\mathrm{K}$ for gas and $10^3\,\mathrm{K}$ on dust in the hottest disc, near the inner disc edge, where stellar radiation is more intense, and decrease towards higher radii. A particular characteristic of these discs, especially the discs 3 and 6, is the lack of vertical stratification in their temperature distribution (both gas and dust temperatures). This can be attributed to different factors. One point to consider is the age of the discs (see Table 3.1.1), with ages less than $100,\mathrm{kyr}$.

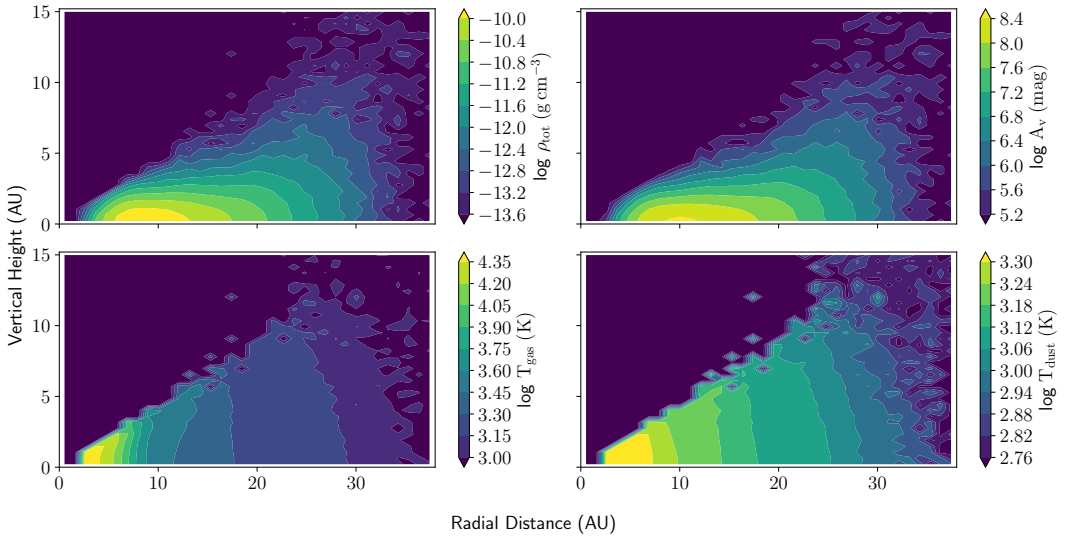

Figure 3.2.1: Disc 1 vertical structure at $t = 1.20t_{ff} = 228$ kyrs (i.e., last snapshot). The 2D mass density (top-left), visual extinction (top-right), gas temperature (bottom-left), and dust temperature (bottom-right) profiles are reported as a function of the discs radius and height both in AU units. The logarithmic colorbar represents the levels of the contour for each quantity, divided into 10 levels for each range.

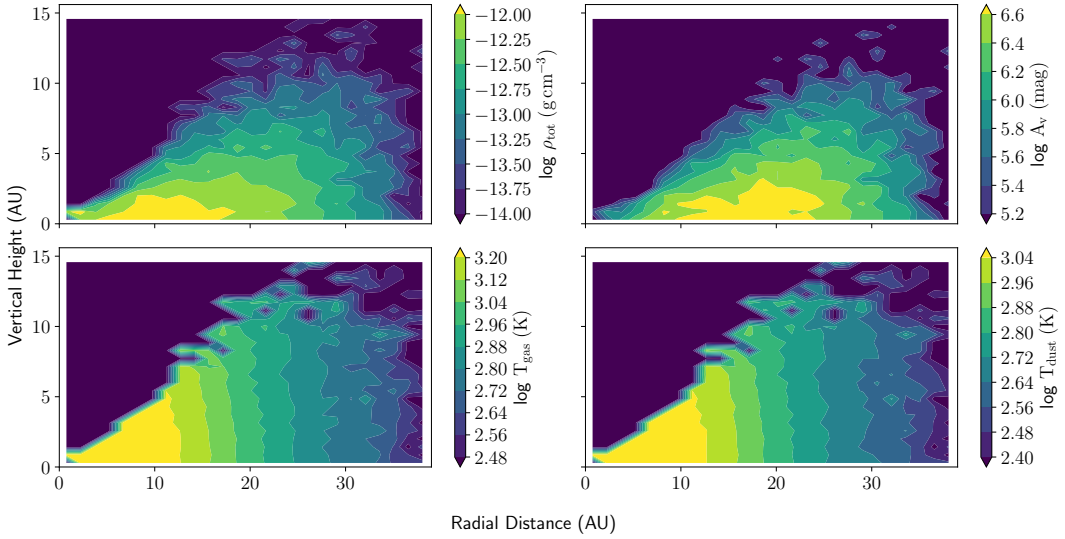

Figure 3.2.2: Disc 3 vertical structure at $t = 1.20t_{ff} = 228$ kyrs. The 2D mass density (top-left), visual extinction (top-right), gas temperature (bottom-left), and dust temperature (bottom-right) profiles are represented as a function of the discs radius vs. height both in AU units. The logarithmic colorbar represents the levels of the contour for each quantity, divided into 10 levels for each range.

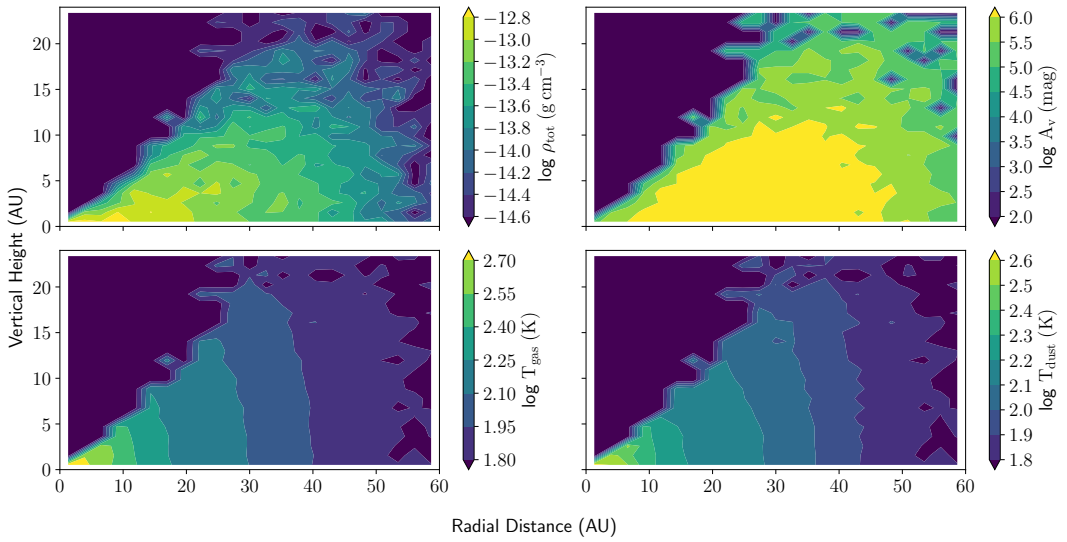

Figure 3.2.3: Disc 6 vertical structure at $t = 1.20t_{ff} = 228$ kyrs. The 2D mass density (top-left), visual extinction (top-right), gas temperature (bottom-left), and dust temperature (bottom-right) profiles are represented as a function of the discs radius vs. height both in AU units. The logarithmic colorbar represents the levels of the contour for each quantity, divided into 10 levels for each range.

At such early stages, the discs have not had sufficient time to develop significant vertical stratification, a process that typically requires more time for denser, heavier particles to settle towards the midplane and for temperature gradients to become well-established. Another contributing factor could be insufficient numerical resolution in the simulations (for discs 3 and 6 the number of particles is notably lower in comparison to disc 1), which may artificially smooth vertical gradients.

A_v takes exceptionally high values ($> 10^5$) close to the discs midplane, providing strong shielding against external UV radiation. These values decrease with height and highlight the transition to more exposed regions, where photodissociation processes dominate.

3.2.1 Chemical properties of discs

We follow several important species such as water and some key precursors of methanol (CH_3OH), the smallest complex organic molecule. These are CO; HCO; H_2O; H_2CO and CH_3O, which we explore in the gas phase. Figures 3.2.4, 3.2.5, and 3.2.6 illustrate the gas-phase distribution of these species for the three discs discussed above. The results highlight distinct chemical distributions discs at

different stages of evolution, comparing the disc around the oldest stellar system (disc 1) to younger ones (discs 3 and 6). Specifically, higher concentrations of certain species are observed near the inner regions of the binary disc, whereas younger single-stellar systems exhibit lower and more scattered distributions.

In the binary system disc (Fig. 3.2.4), H-bearing species are concentrated in the inner regions near the disc midplane, in contrast, carbon monoxide (CO) exhibits a nearly uniform vertical distribution in the upper layers, with its abundance decreasing by 2 to 4 orders of magnitudes in the inner zones where temperatures exceed 10^3 K. This distribution reflects the influence of the disc's structural dynamics, driven by the gravitational torque generated by the binary system at its center, redistributing matter outward (see Fig. 3.2.1). Methanol (CH_3OH) is found in significant concentrations near the midplane in the innermost disc regions. This is especially interesting due to the fact that, within the chosen chemical network, gas-phase methanol is produced via the desorption process from dust grains, and generally, the production of methanol in the gas phase is insufficient to show fractional abundances exceeding 10^{-9} (Garrod et al., 2006). The high abundance of this species within a warm disc, particularly concentrated toward its center, where temperatures are high enough to desorb species from dust grains, suggests that methanol predominantly forms in particles located far from the star at early stages, before being transported inward to the warmer regions closer to the star. Once entering the disc, methanol undergoes desorption from dust grains, leading to the high concentrations observed. This desorption process is more efficient near the disc's center due to the elevated temperatures in this part of the disc. In fact, if we look at the dust temperature distribution and compare it with the methanol distribution, we see that both quantities share a similar distribution shape in dense regions. Water (H_2O) also follows a similar pattern, but peaks around 10 AU from the center, possibly following higher densities and temperatures between $1000 - 10000$ K. In contrast, formaldehyde (H_2CO) exhibits a more scattered distribution throughout this disc without a clear structure.

The massive single-star system hosting Disc 3 presents a different chemical distribution inside the disc. Carbon monoxide (CO) is uniformly distributed throughout the disc, while small concentrations of HCO, CH_3O, and CH_3OH are observed near the disc midplane. In particular, when comparing Fig. 3.2.5 with Fig. 3.2.2, we find indications that these concentrations correspond to regions

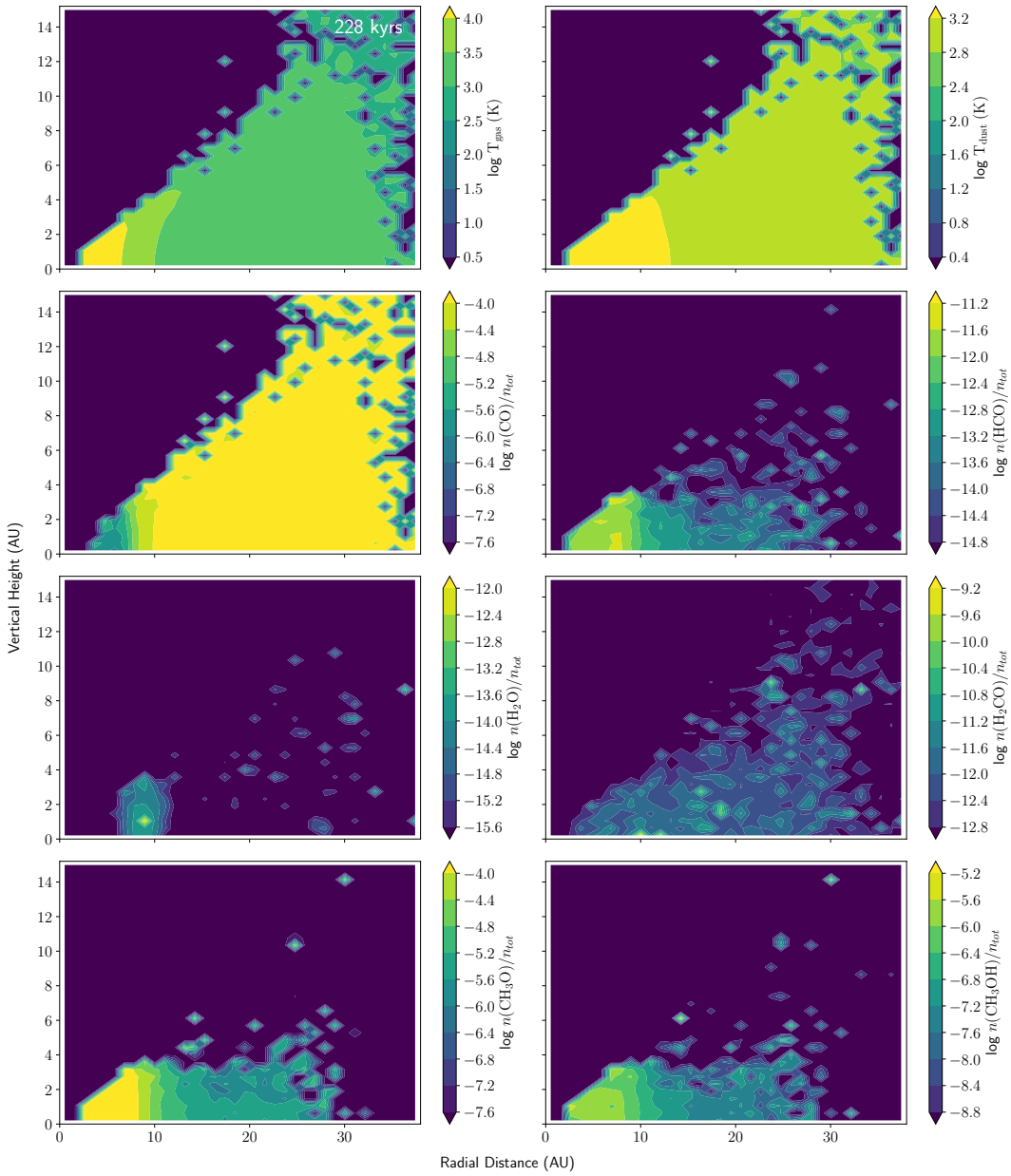

Figure 3.2.4: Disc 1 vertical distribution at $t = 1.20t_{ff} = 228$ kyrs. The 2D distribution plots show: gas temperature, dust temperature, CO relative abundance, HCO relative abundance, H_2O relative abundance, H_2CO relative abundance, CH_3O relative abundance, and CH_3OH relative abundance profiles that are represented as a function of the discs radius vs. height both in AU units. The logarithmic colorbar represents the levels of the contour for each quantity, divided into 10 levels for each range.

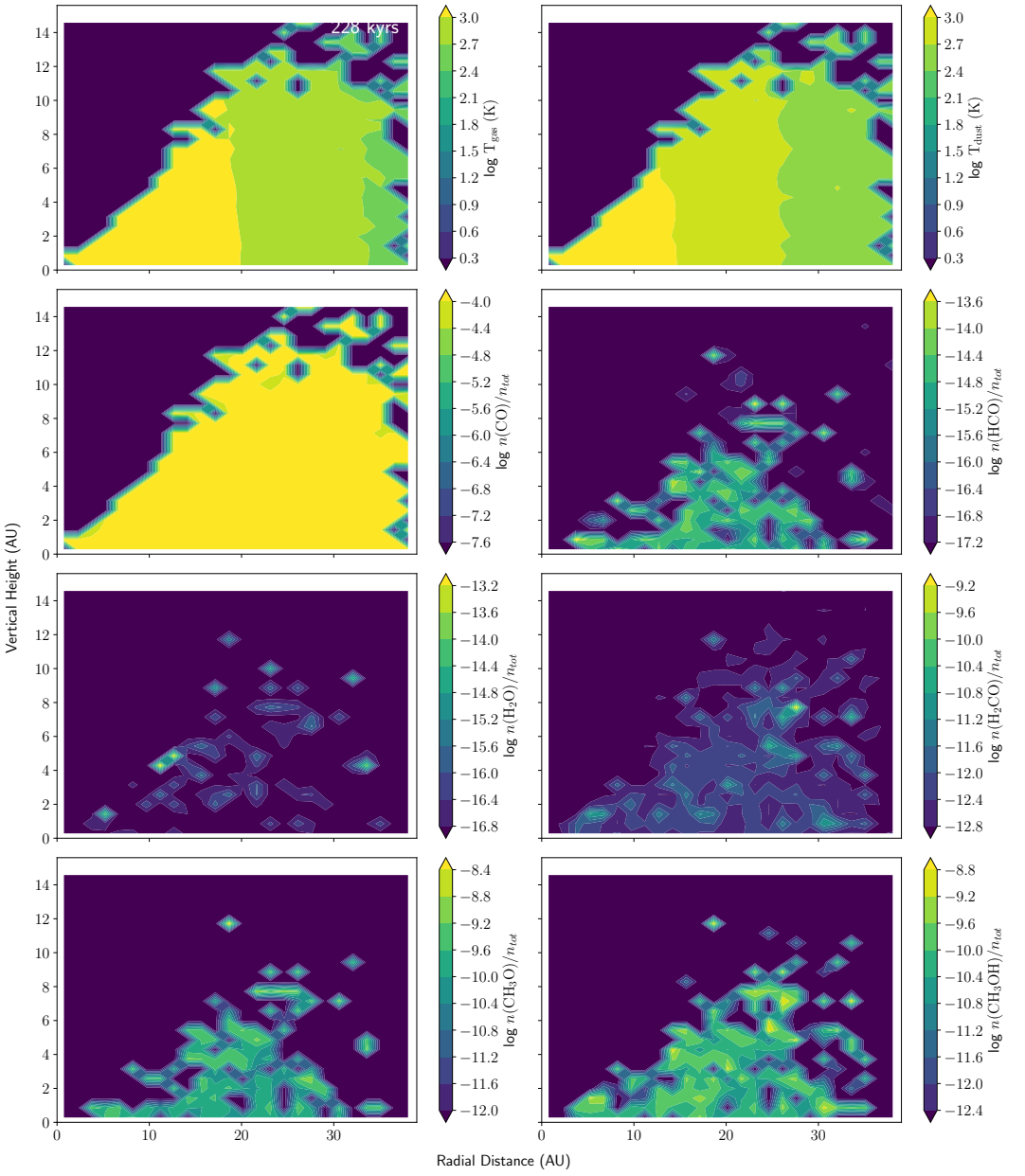

Figure 3.2.5: Disc 3 vertical distribution for different species at $t = 1.20t_{ff} =$ 228 kyrs. The 2D distribution plots show: gas temperature, dust temperature, CO relative abundance, HCO relative abundance, H_2O relative abundance, H_2CO relative abundance, CH_3O relative abundance, and CH_3OH relative abundance profiles that are represented as a function of the discs radius vs. height both in AU units. The logarithmic colorbar represents the levels of the contour for each quantity, divided into 10 levels for each range.

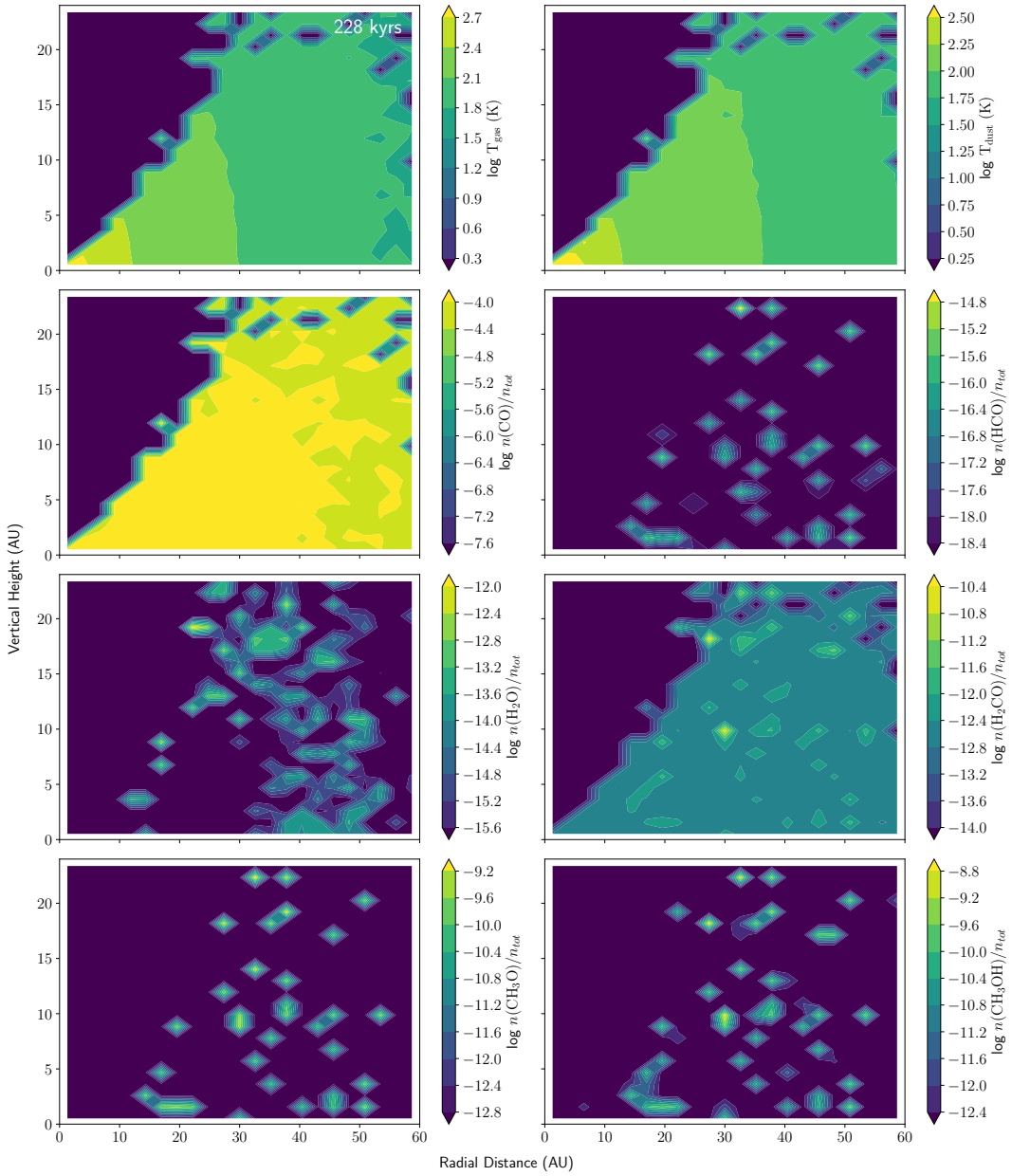

Figure 3.2.6: Disc 6 vertical distribution for different species at $t = 1.20t_{ff} =$ 228 kyrs. The 2D distribution plots show: gas temperature, dust temperature, CO relative abundance, HCO relative abundance, H_2O relative abundance, H_2CO relative abundance, CH_3O relative abundance, and CH_3OH relative abundance profiles that are represented as a function of the discs radius vs. height both in AU units. The logarithmic colorbar represents the levels of the contour for each quantity, divided into 10 levels for each range.

with higher visual extinction. In contrast, water (H_2O) and formaldehyde (H_2CO) show scattered and diffuse distributions, with no significant clustering.

For the low-mass system (Fig. 3.2.6), chemical species exhibit small and scattered concentrations, with the exception of CO and H_2O. Carbon monoxide (CO) shows a relatively uniform distribution, decreasing slightly towards larger radii, possibly following the density and visual extinction distribution profiles throughout the disc. Water (H_2O) shows notable concentrations in regions where temperatures fall below 100 K (see Fig. 3.2.3).

This behavior highlights the influence of key properties on the chemical structure of the different discs present in the region and the evolutionary stage of the different objects. We see that the abundance of chemical species is mainly related to the temperature of gas and dust, related to the presence of gas phase species in regions where the necessary conditions to form them are not accomplished, i.e., high concentrations of methanol in warm discs when its gas phase can only be achieved through desorption from dust grains. In order to explain these peculiar results further analyses are required, in particular to understand the high abundances of species whose formation pathway is only through surface reactions in regions of the discs where surface chemistry is not possible.

3.2.2 Evolution of chemical complexity around sinks

To trace the inheritance and evolution of chemical complexity, the chemical state of the gas and dust in the immediate vicinity of the sink particles was examined in multiple time steps: at the time of the sink particles formation and at subsequent stages of the disc evolution up to the last snapshot. Figures 3.2.7, 3.2.8, and 3.2.9 illustrate the progression of chemical properties around the three analyzed sink particles (also see Appendix A for information on other species). These figures reveal that chemical abundances are initially influenced by the prestellar conditions of the molecular cloud, with cold temperatures promoting the formation of molecules on dust and their subsequent desorption inside warm regions of the discs.

For the binary system of disc 1, the oldest sink particle was selected as the reference point to track the chemical evolution of the system. This choice facilitates the analysis of the interplay between the physical properties of the gas in the vicinity

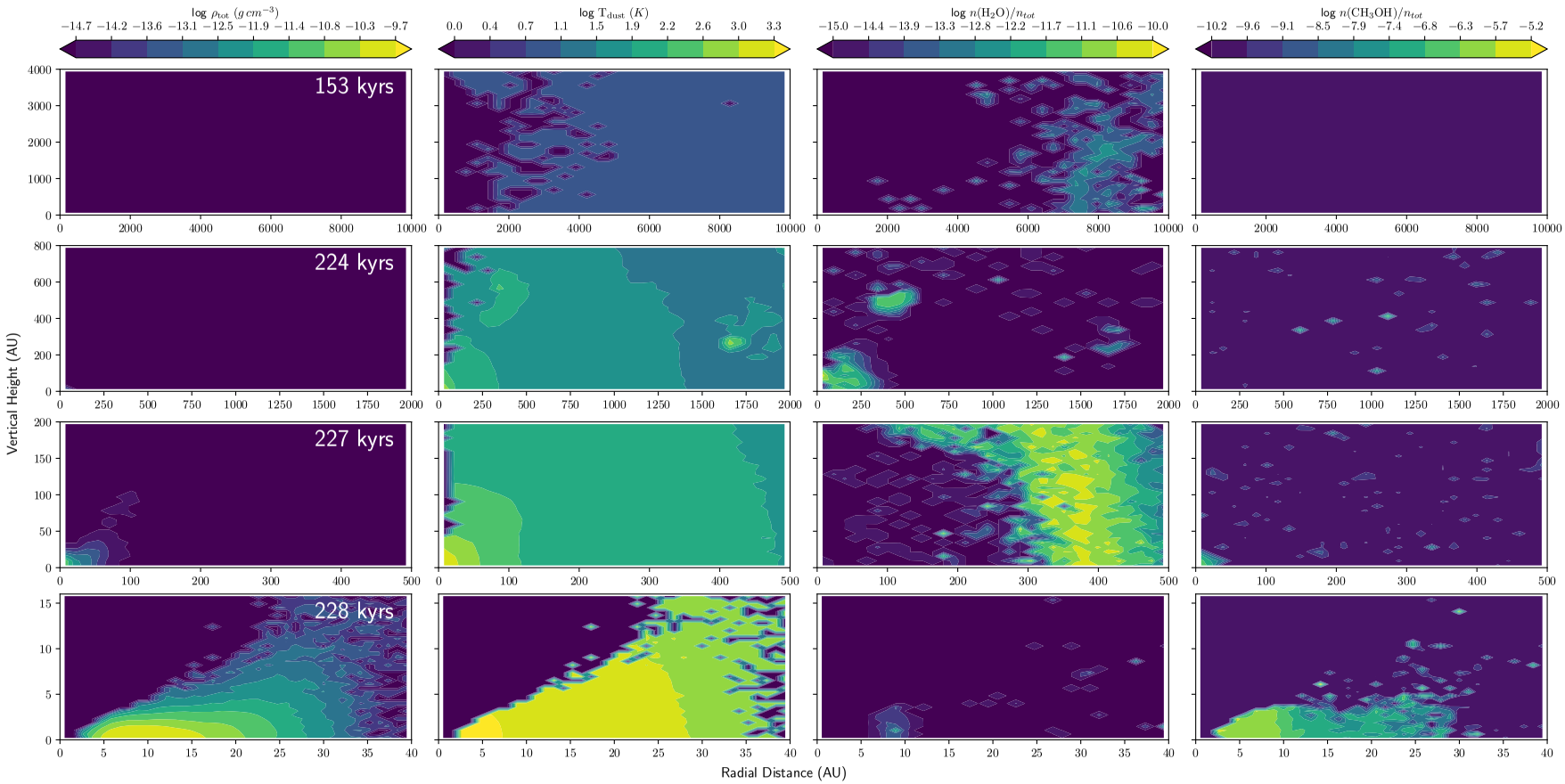

Figure 3.2.7: Time evolution of dust species and physical properties around the sink hosting Disc 1. From top to bottom each row is a different time, ranging from 153 to 224 to 227 and 228 kyrs respectively. From left to right we have $\rho_{\rm tot}$, $T_{\rm dust}$, H_2O relative abundance and CH_3OH relative abundance.

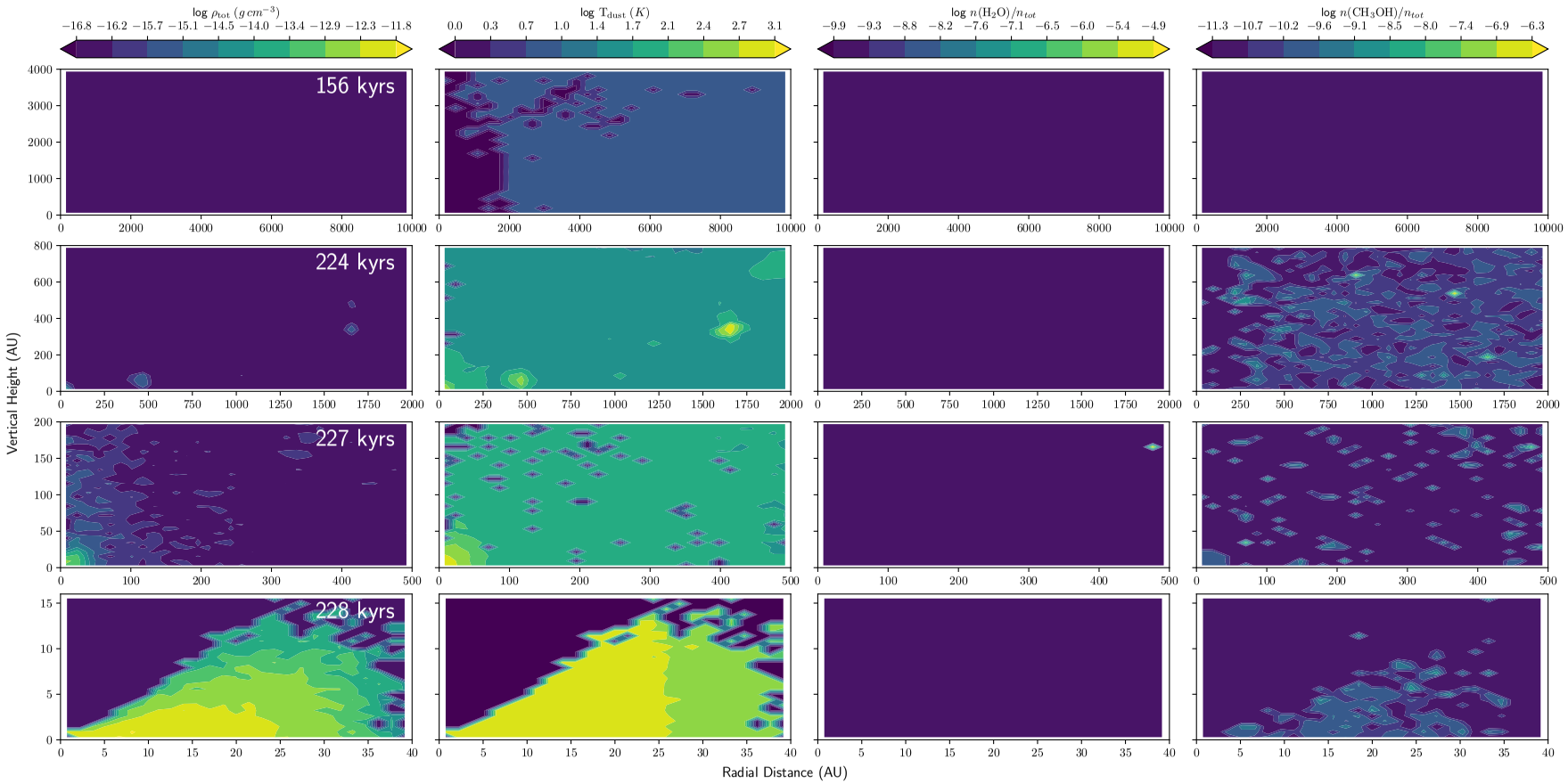

Figure 3.2.8: Time evolution of dust species and physical properties around the sink hosting Disc 3. From top to bottom each row is a different time, ranging from 156 to 224 to 227 and 228 kyrs respectively. From left to right we have $\rho_{\rm tot}$, $T_{\rm dust}$, H_2O relative abundance and CH_3OH relative abundance.

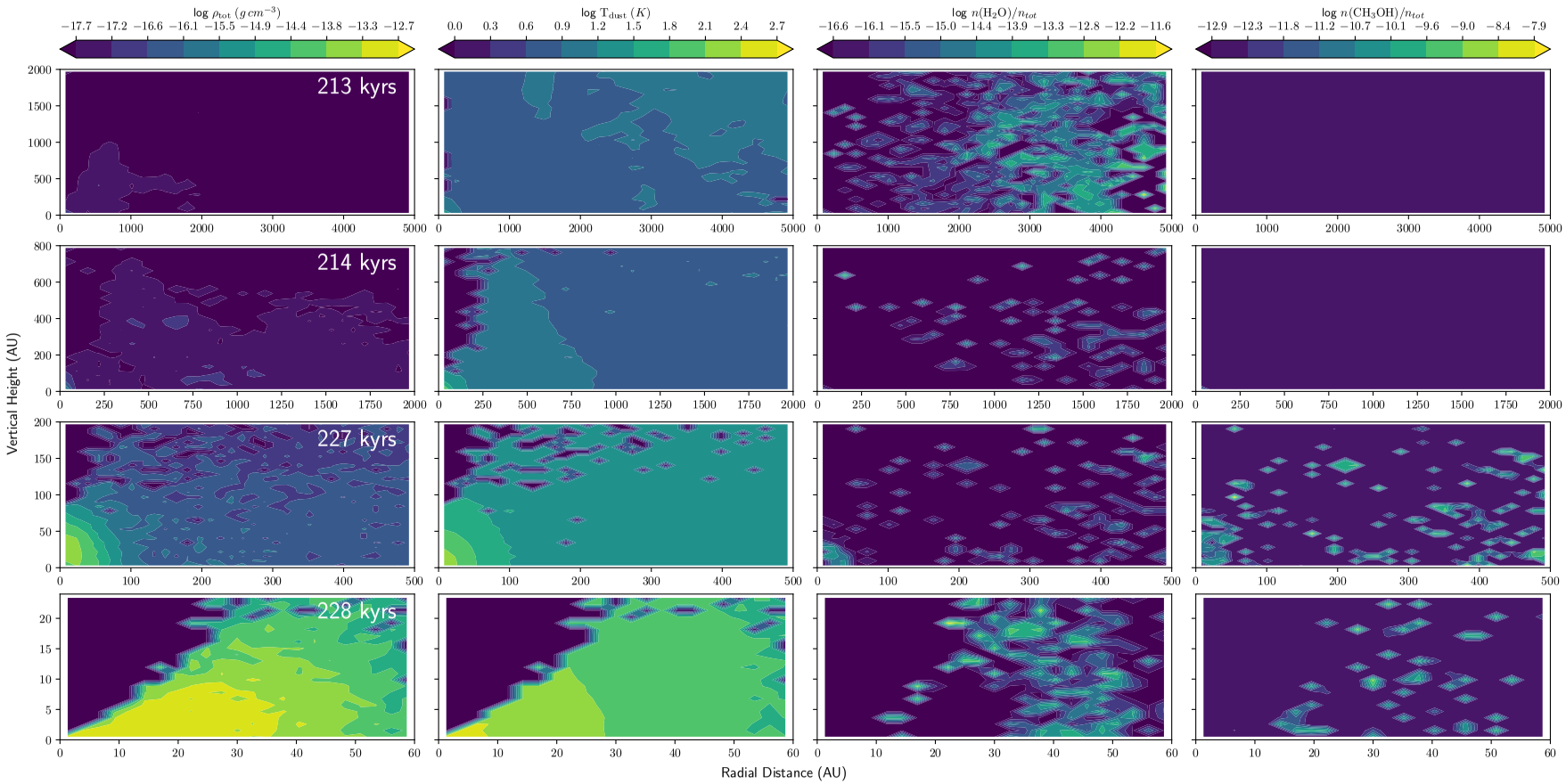

Figure 3.2.9: Time evolution of dust species and physical properties around the sink hosting Disc 6. From top to bottom each row is a different time, ranging from 213 to 214 to 227 and 228 kyrs respectively. From left to right we have $\rho_{\rm tot}$, $T_{\rm dust}$, H_2O relative abundance and CH_3OH relative abundance.

of the sink and the behavior of key species. As visualized in our results, the spatial distribution of these species is closely related to dust temperature, since higher abundances of gas phase species are found inside the warm discs and dust phase species are mostly found in cold regions away from the stars. Methanol (CH_3OH) in dust begins to form approximately > 30 kyrs after the formation of the star, and is found mainly in dust temperature ranges of $\sim 10 - 40$ K, subsequently, gas phase methanol begins to accumulate significantly at later stages of disc evolution, approximately > 50 kyrs after the formation of the sink particle, and is found mainly located in the midplane of the disc specially in warmer regions (see Fig. 3.2.7). Appendix A provides a comprehensive analysis of the spatial distributions of gas- and dust-phase species, including CO, HCO, H_2O, H_2CO, CH_3O, and CH_3OH in the same regions analyzed in Fig. 3.2.7. Additional analysis to the data indicate that dust-phase methanol is relatively more abundant at early stages of the disc evolution in distant regions where temperatures are lower, these particles containing high dust phase abundances are further incorporated into the discs and desorb the species to the gas-phase due to the elevated temperatures inside the discs. Therefore, high methanol abundances are concentrated in hotter regions of the disc within the binary system. For water we see similar trends; on dust grains it exhibits relatively a more homogeneous abundance distribution around the star across earlier stages and then desorbs to gas phase inside the warm disc. Although it has a similar behavior with temperature as methanol, water is sensitive to a wider range of temperatures ($\sim 6 - 100$ K).

For single and younger stellar systems (associated with discs 3 and 6), the chemical distributions exhibit trends similar to those observed in disc 1. The key difference compared to the binary system is the lower abundance of water and methanol in the last snapshot, probably because of the evolutionary stage of these objects at that point. These observations align with the respective formation pathways of both species. As methanol and formaldehyde form in grains under dark cloud conditions by hydrogenation of CO on dust:

$$\perp \mathrm{CO} \xrightarrow{\perp \mathrm{H}} \perp \mathrm{HCO} \xrightarrow{\perp \mathrm{H}} \perp \mathrm{H_2CO} \xrightarrow{\perp \mathrm{H}} \perp \mathrm{CH_3O} \xrightarrow{\perp \mathrm{H}} \perp \mathrm{CH_3OH} \tag{3.2.1}$$

Note that the radical $\perp CH_3O$ can also be formed through some additional reactions starting with oxygen on dust

$$\begin{matrix} \perp \mathrm{O} \\ \perp \mathrm{O_3} \end{matrix} \xrightarrow[\perp \mathrm{H}]{\perp \mathrm{H}, \perp \mathrm{H_2}, \perp \mathrm{HO_2}} \perp \mathrm{OH} \xrightarrow[\perp \mathrm{CH_3}]{\perp \mathrm{CH_2}} \begin{matrix} \perp \mathrm{CH_3O} \\ \perp \mathrm{CH_3OH} \end{matrix} \tag{3.2.2}$$

In contrast, water and the other analyzed molecules with multiple formation pathways in the adopted chemical network are more abundant and seems to promote methanol formation in the discs. Its production depends primarily on the presence of suitable environmental conditions, which are widely available in this region due to its broad range of temperatures and densities. This explains a more widespread and consistent distribution of these species in both single and binary systems.

It is also important to consider the evolutionary stage of the discs presented in this work, as the disc around the binary system is older than the ones surrounding single stellar systems. This can be one of the reasons for the difference in methanol abundances between those discs where younger discs contain lower abundances and a more scattered distribution, highlighting that methanol formation begins at later stages of the discs evolution.

Chapter 4

Concluding Remarks

This thesis has focused on the implementation and analysis of complex chemistry within circumstellar discs formed in a simulation of a star-forming molecular cloud. Using post-processing techniques similar to those outlined in Ferrada-Chamorro et al. (2021), we incorporated a detailed chemical network into the Smoothed Particle Hydrodynamics simulation presented in Bate (2019). By combining the physical properties of the discs formed in the simulation with astrochemical modeling using the KROME package (Grassi et al., 2014), we have analyzed the intricate interplay between key parameters and the chemical evolution of the discs, emphasizing the role of methanol (CH_3OH) as a tracer of chemical complexity. This work advances our understanding of how physical conditions in circumstellar discs influence the synthesis, distribution, and evolution of complex molecules in the context of star-forming molecular clouds, addressing a critical aspect of star and planet formation research.

4.1 Key Results and Their Implications

One of the main findings of this study is the relationship between the physical structure of circumstellar discs and their chemical composition and evolution. The vertical distribution of gas density, gas and dust temperatures, and visual extinction form different zones that define the chemical environment within discs and the immediate surrounding of disc during the evolution of such objects. The dense and cold regions around the sinks create the conditions necessary to host surface chemistry and freeze-out reactions. This, combined with high temperatures

at later stages of the discs evolution, result in higher abundances of gas phase species such as methanol and water in denser regions inside the discs at advanced stages of their evolution; this can be seen by comparing the binary system with younger ones and comparing their methanol distribution; in particular we can see that methanol shows higher concentrations in the binary system disc in the last snapshots, in comparison to the younger discs whose show less abundant and scattered distributions of this molecule. Methanol, in particular, demonstrates a clear correlation with dust temperature. It forms on grain surfaces at temperatures between $10 - 40\,\mathrm{K}$, desorbs at higher temperatures, and subsequently accumulates in warm regions of the discs. These findings align with previous work (Walsh et al., 2014) which emphasized the critical role of thermal desorption and surface chemistry in shaping the distribution of complex organic molecules in discs.

The chemical distribution of the circumbinary disc system differs significantly from that of single-stellar systems. Binary systems exhibit more dynamic structures, influenced by gravitational torques that redistribute material and create zones of varying density and temperatures. This dynamic behavior is reflected in the observed chemical distributions, with methanol and water concentrated near the midplane and inner regions, while CO is more uniformly distributed in the outer layers. In contrast, single-stellar systems display more homogeneous chemical distributions, with methanol and other species correlated with high A_v regions, reinforcing the role of UV shielding in promoting chemical complexity.

Additionally, our study revealed the temporal evolution of chemical complexity around in the close vicinities of sink particles during the evolution of discs. The formation and accumulation of methanol is closely related to prestellar conditions and the subsequent evolution of the disc. During the early stages of the disc formation, the cold temperatures facilitate the synthesis of methanol and other species on dust grains. As the systems evolve, methanol desorbs and becomes abundant in gas phase, particularly in regions where temperatures rise above the desorption threshold. This temporal evolution underscores the importance of studying chemical inheritance from the molecular cloud phase, as mentioned in Herbst and van Dishoeck (2009), who showed how prestellar chemistry influences the molecular composition of protostellar and protoplanetary environments.

4.2 Limitations and Future Research

While this thesis has provided valuable information on the addition of complex chemistry in simulations using post-processing techniques, several limitations in the methodology highlight areas for further improvement and future research. First, the chemical network used in this study was limited to a basic $H - C - O$ framework, restricting the analysis to a small subset of species. The expansion of the network would represent a big step forward to improve this kind of research. Including N− and S-bearing species (e.g., NH_3, N_2H^+, SO, CS) would allow a more comprehensive analysis of the chemical diversity in discs.

Also, to have a better view on different discs and regions over time, it is necessary to improve the resolution of the simulation and modify the extraction methods to avoid losing data between snapshots. A better method to extract a region or simply working with the entire dataset will improve further analysis and help us to have better statistics by studying more and well defined discs through time.

Finally, another limitation arises from the post-processing approach used in this study. Although computationally efficient, this method ignores key interactions between chemistry and evolving physical conditions. Implementing on-the-fly chemistry in simulations would enable a more realistic coupling between physical and chemical evolution.

4.3 Broader Implications and Future Prospects

The results of this work have opened multiple pathways for future research on chemical complexity inside star-forming regions, particularly on the later stages of stellar evolution involving circumstellar disc structures. One of the significant outcomes of this work is the successful integration of complex chemical processes into simulations of star-forming regions, revealing some important processes occurring in the dynamics of these bodies. Although this thesis mainly focused on modeling the chemical evolution of star-forming regions and circumstellar environments, there is enough room to expand this work into more resolved simulations involving protoplanetary discs, which are a crucial step in the evolution of stellar systems. Methanol, often considered a precursor to prebiotic molecules, serves as a critical benchmark to assess the potential for chemical complexity in

protoplanetary environments. Future studies that incorporate a wider range of species and reactions will further clarify the pathways leading to the synthesis of prebiotic molecules, providing valuable context for interpreting observations of extrasolar systems.

To further advance our understanding of chemical processes in protoplanetary discs, future research must focus on exploring these processes in more refined simulations, enhancing both their spatial and temporal resolution, enabling the capture of finer details of chemical evolution. This can be achieved by implementing on-the-fly (OTF) chemistry within the simulations, where chemical reactions are dynamically computed during the simulation rather than through post-processing. This approach significantly improves the accuracy and consistency of chemical models in simulations (Ferrada-Chamorro et al., 2021; Perotti et al., 2024). Implementing OTF chemistry in protoplanetary disc simulations will allow for a more realistic tracking of the intricate interplay between micro- and macrophysics, as this method allows for a consistent thermal evolution of the regions as a result of chemical reactions. Incorporating more resolved chemistry in such simulations would also enable a deeper investigation of the impact of stellar radiation and accretion processes on disc chemistry. Protoplanetary discs experience strong irradiation from their central stars, particularly in the form of far-UV and X-ray radiation, which significantly influences the ionization states and chemical pathways in the disc (Bergin et al., 2007). To understand how this affects molecular abundances and the formation of complex organic molecules, future work will need to incorporate both improved radiative transfer models and expanded chemical networks that can simulate the influence of ionization on molecular processes. Furthermore, future research should explore the role of turbulence and disc dynamics on chemical distributions. Previous studies have indicated that turbulence can play a significant role in mixing chemical species across the disc, leading to non-uniform distributions of molecules that are crucial for planet formation (Glover et al., 2010). By coupling advanced hydrodynamic simulations with detailed chemical networks, future research can investigate how turbulence-induced mixing affects the evolution of key molecules.

In addition, the inclusion of dust evolution and grain surface chemistry in future models will be essential. Grain surface reactions have been identified as key processest for the formation of complex organic molecules in protoplanetary discs

(Herbst and van Dishoeck, 2009). As dust grains grow and migrate within the disc, they provide surfaces for chemical reactions that cannot occur in gas phase, significantly influencing the overall chemical composition and diversity. Future simulations that couple the dynamics of dust growth with grain-surface chemical reactions would provide a more comprehensive understanding of the chemistry in these environments.

Finally, combining theoretical models with observational data, such as those obtained by ALMA and JWST, will be crucial for validating and refining these models, as our objective is to address theoretical models in order to predict the behavior of real systems in order to support observational studies.

By addressing current limitations and broadening the scope of analysis, future research can provide deeper insights into the origins of chemical complexity, offering a bridge between the physics of star formation and the chemistry that contribute to the emergence of planetary systems.

Bibliography

Ádámkovics, M., Glassgold, A. E., and Najita, J. R. (2014). Shielding by Water and OH in FUV and X-Ray Irradiated Protoplanetary Disks. *Astrophysical Journal*, 786(2):135.

Aikawa, Y. and Herbst, E. (1999). Molecular evolution in protoplanetary disks. Two-dimensional distributions and column densities of gaseous molecules. *Astronomy and Astrophysics*, 351:233–246.

Aikawa, Y., Okuzumi, S., and Pontoppidan, K. (2022). The physical and chemical processes in protoplanetary disks: constraints on the composition of comets. *arXiv e-prints*, page arXiv:2212.14529.

Akimkin, V., Zhukovska, S., Wiebe, D., Semenov, D., Pavlyuchenkov, Y., Vasyunin, A., Birnstiel, T., and Henning, T. (2013). Protoplanetary Disk Structure with Grain Evolution: The ANDES Model. *Astrophysical Journal*, 766(1):8.

Andre, P., Ward-Thompson, D., and Barsony, M. (2000). From Prestellar Cores to Protostars: the Initial Conditions of Star Formation. In Mannings, V., Boss, A. P., and Russell, S. S., editors, *Protostars and Planets IV*, page 59.

Andrews, S. M., Wilner, D. J., Hughes, A. M., Qi, C., and Dullemond, C. P. (2010). Protoplanetary Disk Structures in Ophiuchus. II. Extension to Fainter Sources. *Astrophysical Journal*, 723(2):1241–1254.

Armitage, P. J. (2011). Dynamics of Protoplanetary Disks. *Annual Review of Astronomy and Astrophysics*, 49(1):195–236.

Artymowicz, P. and Lubow, S. H. (1994). Dynamics of Binary-Disk Interaction. I. Resonances and Disk Gap Sizes. *Astrophysical Journal*, 421:651.

Bachiller, R. (1996). Bipolar molecular outflows from young stars and protostars. *Annual Review of Astronomy and Astrophysics*, 34(Volume 34, 1996):111–154.

Bacmann, A., Lefloch, B., Ceccarelli, C., Castets, A., Steinacker, J., and Loinard, L. (2002). The degree of CO depletion in pre-stellar cores. *Astronomy and Astrophysics*, 389:L6–L10.

Bacmann, A., Lefloch, B., Ceccarelli, C., Steinacker, J., Castets, A., and Loinard, L. (2003). CO Depletion and Deuterium Fractionation in Prestellar Cores. *Astrophysical Journal, Letters*, 585(1):L55–L58.

Bate, M. R. (2012). Stellar, brown dwarf and multiple star properties from a radiation hydrodynamical simulation of star cluster formation. *Monthly Notices of the RAS*, 419(4):3115–3146.

Bate, M. R. (2018). On the diversity and statistical properties of protostellar discs. *Monthly Notices of the RAS*, 475(4):5618–5658.

Bate, M. R. (2019). The statistical properties of stars and their dependence on metallicity. *Monthly Notices of the RAS*, 484(2):2341–2361.

Bate, M. R., Bonnell, I. A., and Bromm, V. (2003). The formation of a star cluster: predicting the properties of stars and brown dwarfs. *Monthly Notices of the RAS*, 339(3):577–599.

Bate, M. R., Bonnell, I. A., and Price, N. M. (1995). Modelling accretion in protobinary systems. *Monthly Notices of the RAS*, 277(2):362–376.

Bate, M. R. and Burkert, A. (1997). Resolution requirements for smoothed particle hydrodynamics calculations with self-gravity. *Monthly Notices of the RAS*, 288(4):1060–1072.

Bate, M. R. and Keto, E. R. (2015). Combining radiative transfer and diffuse interstellar medium physics to model star formation. *Monthly Notices of the RAS*, 449(3):2643–2667.

Benz, W. (1990). Smooth Particle Hydrodynamics - a Review. In Buchler, J. R., editor, *Numerical Modelling of Nonlinear Stellar Pulsations Problems and Prospects*, page 269.

Benz, W., Bowers, R. L., Cameron, A. G. W., and Press, W. H. . (1990). Dynamic Mass Exchange in Doubly Degenerate Binaries. I. 0.9 and 1.2 M_{sun} Stars. *Astrophysical Journal*, 348:647.

Bergin, E. A., Aikawa, Y., Blake, G. A., and van Dishoeck, E. F. (2007). The Chemical Evolution of Protoplanetary Disks. In Reipurth, B., Jewitt, D., and Keil, K., editors, *Protostars and Planets V*, page 751.

Boogert, A. C. A., Gerakines, P. A., and Whittet, D. C. B. (2015). Observations of the icy universe. *Annual Review of Astronomy and Astrophysics*, 53:541–581.

Boss, A. P., Fisher, R. T., Klein, R. I., and McKee, C. F. (2000). The Jeans Condition and Collapsing Molecular Cloud Cores: Filaments or Binaries? *Astrophysical Journal*, 528(1):325–335.

Bovino, S., Schleicher, D. R. G., and Grassi, T. (2019). Computational Astrochemistry: importance, pitfalls and applications. *Boletin de la Asociacion Argentina de Astronomia La Plata Argentina*, 61:274–276.

Capelo, P. R., Bovino, S., Lupi, A., Schleicher, D. R. G., and Grassi, T. (2018). The effect of non-equilibrium metal cooling on the interstellar medium. *Monthly Notices of the RAS*, 475(3):3283–3304.

Carr, J. S. and Najita, J. R. (2011). Organic Molecules and Water in the Inner Disks of T Tauri Stars. *Astrophysical Journal*, 733(2):102.

Caselli, P. and Ceccarelli, C. (2012). Our astrochemical heritage. *Astronomy and Astrophysics Reviews*, 20:56.

Christensen, C., Quinn, T., Governato, F., Stilp, A., Shen, S., and Wadsley, J. (2012). Implementing molecular hydrogen in hydrodynamic simulations of galaxy formation. *Monthly Notices of the RAS*, 425(4):3058–3076.

Coutens, A., Commerçon, B., and Wakelam, V. (2020). Chemical evolution during the formation of a protoplanetary disk. *Astronomy and Astrophysics*, 643:A108.

Dullemond, C. P. and Monnier, J. D. (2010). The Inner Regions of Protoplanetary Disks. *Annual Review of Astronomy and Astrophysics*, 48:205–239.

Dutrey, A., Semenov, D., Chapillon, E., Gorti, U., Guilloteau, S., Hersant, F., Hogerheijde, M., Hughes, M., Meeus, G., Nomura, H., Piétu, V., Qi, C., and Wakelam, V. (2014). Physical and Chemical Structure of Planet-Forming Disks Probed by Millimeter Observations and Modeling. In Beuther, H., Klessen, R. S., Dullemond, C. P., and Henning, T., editors, *Protostars and Planets VI*, pages 317–338.

Ercolano, B. and Koepferl, C. (2014). The lifetime of protoplanetary discs: Observations and theory. In Stamatellos, D., Goodwin, S., and Ward-Thompson, D., editors, *The Labyrinth of Star Formation*, pages 63–68, Cham. Springer International Publishing.

Fehlberg, E. (1969). Low-order classical runge-kutta formulas with stepsize control and their application to some heat transfer problems. Technical Report NASA-TR-R-315, NASA. Available at NASA Technical Reports Server (NTRS).

Ferrada-Chamorro, S., Lupi, A., and Bovino, S. (2021). Chemical post-processing of magneto-hydrodynamical simulations of star-forming regions: robustness and pitfalls. *Monthly Notices of the RAS*, 505(3):3442–3451.

Garrod, R., Park, I. H., Caselli, P., and Herbst, E. (2006). Are gas-phase models of interstellar chemistry tenable? The case of methanol. *Faraday Discussions*, 133:51.

Garrod, R. T., Weaver, S. L. W., and Herbst, E. (2008). Complex chemistry in star-forming regions: An expanded gas-grain warm-up chemical model. *The Astrophysical Journal*, 682(1):283.

Glassgold, A. E., Najita, J., and Igea, J. (2004). Heating Protoplanetary Disk Atmospheres. *Astrophysical Journal*, 615(2):972–990.

Glover, S. C. O. and Abel, T. (2008). Uncertainties in H2 and HD chemistry and cooling and their role in early structure formation. *Monthly Notices of the Royal Astronomical Society*, 388(4):1627–1651.

Glover, S. C. O. and Clark, P. C. (2012a). Approximations for modelling CO chemistry in giant molecular clouds: a comparison of approaches. *Monthly Notices of the RAS*, 421(1):116–131.

Glover, S. C. O. and Clark, P. C. (2012b). Star formation in metal-poor gas clouds. *Monthly Notices of the RAS*, 426(1):377–388.

Glover, S. C. O., Federrath, C., Mac Low, M. M., and Klessen, R. S. (2010). Modelling CO formation in the turbulent interstellar medium. *Monthly Notices of the RAS*, 404(1):2–29.

Gnedin, N. Y., Tassis, K., and Kravtsov, A. V. (2009). Modeling Molecular Hydrogen and Star Formation in Cosmological Simulations. *Astrophysical Journal*, 697(1):55–67.

Goldsmith, P. F. and Langer, W. D. (1978). Molecular cooling and thermal balance of dense interstellar clouds. *Astrophysical Journal*, 222:881–895.

Grassi, T., Bovino, S., Gianturco, F. A., Baiocchi, P., and Merlin, E. (2012). Complexity reduction of astrochemical networks. *Monthly Notices of the RAS*, 425(2):1332–1340.

Grassi, T., Bovino, S., Haugbølle, T., and Schleicher, D. R. G. (2017). A detailed framework to incorporate dust in hydrodynamical simulations. *Monthly Notices of the RAS*, 466(2):1259–1274.

Grassi, T., Bovino, S., Schleicher, D. R. G., Prieto, J., Seifried, D., Simoncini, E., and Gianturco, F. A. (2014). KROME - a package to embed chemistry in astrophysical simulations. *Monthly Notices of the RAS*, 439(3):2386–2419.

Grassi, T., Merlin, E., Piovan, L., Buonomo, U., and Chiosi, C. (2011). MaNN: Multiple Artificial Neural Networks for modelling the Interstellar Medium. *arXiv e-prints*, page arXiv:1103.0509.

Günther, R. and Kley, W. (2002). Circumbinary disk evolution. *Astronomy and Astrophysics*, 387:550–559.

Hartmann, L. (1998). *Accretion Processes in Star Formation*.

Hasegawa, T. I. and Herbst, E. (1993). New gas-grain chemical models of quiscent dense interstellar clouds :the effects of H2 tunnelling reactions and cosmic ray induced desorption. *Monthly Notices of the RAS*, 261:83–102.

Henning, T. and Semenov, D. (2013). Chemistry in Protoplanetary Disks. *Chemical Reviews*, 113(12):9016–9042.

Herbst, E. and van Dishoeck, E. F. (2009). Complex organic interstellar molecules. *Annual Review of Astronomy and Astrophysics*, 47(Volume 47, 2009):427–480.

Hindmarsh, A. C. (1983). ODEPACK, A Systematized Collection of ODE Solvers. In Stepleman, R. S. et al., editors, *Scientific Computing*, volume 1 of

IMACS Transactions on Scientific Computation, pages 55–64. North-Holland, Amsterdam. Also available as LLNL Report UCRL-88007, August 1982.

Hocuk, S. and Cazaux, S. (2015). Interplay of gas and ice during cloud evolution. *Astronomy and Astrophysics*, 576:A49.

Hollenbach, D. and McKee, C. F. (1979). Molecule formation and infrared emission in fast interstellar shocks. I. Physical processes. *Astrophysical Journal, Supplement*, 41:555–592.

Hollenbach, D. and McKee, C. F. (1989). Molecule Formation and Infrared Emission in Fast Interstellar Shocks. III. Results for J Shocks in Molecular Clouds. *Astrophysical Journal*, 342:306.

Hu, C.-Y., Naab, T., Walch, S., Glover, S. C. O., and Clark, P. C. (2016). Star formation and molecular hydrogen in dwarf galaxies: a non-equilibrium view. *Monthly Notices of the RAS*, 458(4):3528–3553.

Hubber, D. A., Goodwin, S. P., and Whitworth, A. P. (2006). Resolution requirements for simulating gravitational fragmentation using SPH. *Astronomy and Astrophysics*, 450(3):881–886.

Jørgensen, J. K., Belloche, A., and Garrod, R. T. (2020). Astrochemistry During the Formation of Stars. *Annual Review of Astronomy and Astrophysics*, 58:727–778.

Jørgensen, J. K., Favre, C., Bisschop, S. E., Bourke, T. L., van Dishoeck, E. F., and Schmalzl, M. (2012). Detection of the Simplest Sugar, Glycolaldehyde, in a Solar-type Protostar with ALMA. *Astrophysical Journal, Letters*, 757(1):L4.

Katz, H., Kimm, T., Sijacki, D., and Haehnelt, M. G. (2017). Interpreting ALMA observations of the ISM during the epoch of reionization. *Monthly Notices of the RAS*, 468(4):4831–4861.

Keto, E. and Caselli, P. (2008). The Different Structures of the Two Classes of Starless Cores. *Astrophysical Journal*, 683(1):238–247.

Larson, R. B. (1969). Numerical calculations of the dynamics of collapsing proto-star. *Monthly Notices of the RAS*, 145:271.

Larson, R. B. (2003). The physics of star formation. *Reports on Progress in Physics*, 66(10):1651–1697.

Lissauer, J. J. (1993). Planet formation. *Annual Review of Astronomy and Astrophysics*, 31:129–174.

Lupi, A. and Bovino, S. (2020). The [C II]-SFR correlation in dwarf galaxies across cosmic time. *Monthly Notices of the RAS*, 492(2):2818–2827.

Lupi, A., Bovino, S., Capelo, P. R., Volonteri, M., and Silk, J. (2018). The natural emergence of the correlation between H_2 and star formation rate surface densities in galaxy simulations. *Monthly Notices of the RAS*, 474(3):2884–2903.

Lupi, A., Pallottini, A., Ferrara, A., Bovino, S., Carniani, S., and Vallini, L. (2020). Predicting FIR lines from simulated galaxies. *Monthly Notices of the RAS*, 496(4):5160–5175.

Mac Low, M.-M. and Klessen, R. S. (2004). Control of star formation by supersonic turbulence. *Reviews of Modern Physics*, 76(1):125–194.

Mamajek, E. E. (2009). Initial Conditions of Planet Formation: Lifetimes of Primordial Disks. In Usuda, T., Tamura, M., and Ishii, M., editors, *Exoplanets and Disks: Their Formation and Diversity*, volume 1158 of *American Institute of Physics Conference Series*, pages 3–10.

Mandell, A. M., Bast, J., van Dishoeck, E. F., Blake, G. A., Salyk, C., Mumma, M. J., and Villanueva, G. (2012). First Detection of Near-infrared Line Emission from Organics in Young Circumstellar Disks. *Astrophysical Journal*, 747(2):92.

Markwick, A. J., Ilgner, M., Millar, T. J., and Henning, T. (2002). Molecular distributions in the inner regions of protostellar disks. *Astronomy and Astrophysics*, 385:632–646.

Mathis, J. S., Rumpl, W., and Nordsieck, K. H. (1977). The size distribution of interstellar grains. *Astrophysical Journal*, 217:425–433.

McCaughrean, M. J. and O'Dell, C. R. (1996). Direct Imaging of Circumstellar Disks in the Orion Nebula. *Astronomical Journal*, 111:1977.

McKee, C. F. and Ostriker, E. C. (2007). Theory of Star Formation. *Annual Review of Astronomy and Astrophysics*, 45(1):565–687.

Morbidelli, A., Lunine, J. I., O'Brien, D. P., Raymond, S. N., and Walsh, K. J. (2012). Building Terrestrial Planets. *Annual Review of Earth and Planetary Sciences*, 40(1):251–275.

Najita, J. R., Ádámkovics, M., and Glassgold, A. E. (2011). Formation of Organic Molecules and Water in Warm Disk Atmospheres. *Astrophysical Journal*, 743(2):147.

Najita, J. R., Carr, J. S., Brittain, S. D., Lacy, J. H., Richter, M. J., and Doppmann, G. W. (2021). High-resolution Mid-infrared Spectroscopy of GV Tau N: Surface Accretion and Detection of NH_3 in a Young Protoplanetary Disk. *Astrophysical Journal*, 908(2):171.

Najita, J. R., Carr, J. S., Glassgold, A. E., and Valenti, J. A. (2007). Gaseous Inner Disks. In Reipurth, B., Jewitt, D., and Keil, K., editors, *Protostars and Planets V*, page 507.

Nickerson, S., Teyssier, R., and Rosdahl, J. (2018). A simple model for molecular hydrogen chemistry coupled to radiation hydrodynamics. *Monthly Notices of the RAS*, 479(3):3206–3226.

Nomura, H., Aikawa, Y., Tsujimoto, M., Nakagawa, Y., and Millar, T. J. (2007).

Molecular Hydrogen Emission from Protoplanetary Disks. II. Effects of X-Ray Irradiation and Dust Evolution. *Astrophysical Journal*, 661(1):334–353.

Öberg, K. I. and Bergin, E. A. (2021). Astrochemistry and compositions of planetary systems. *Physics Reports*, 893:1–48.

Öberg, K. I., Facchini, S., and Anderson, D. (2023). Protoplanetary disk chemistry. *Annual Review of Astronomy and Astrophysics*, 61(1):null.

Öberg, K. I., Fuchs, G. W., Awad, Z., Fraser, H. J., Schlemmer, S., van Dishoeck, E. F., and Linnartz, H. (2007). Photodesorption of CO Ice. *Astrophysical Journal, Letters*, 662(1):L23–L26.

Öberg, K. I., Linnartz, H., Visser, R., and van Dishoeck, E. F. (2009a). Photodesorption of Ices. II. H_2O and D_2O. *Astrophysical Journal*, 693(2):1209–1218.

Öberg, K. I., Qi, C., Fogel, J. K. J., Bergin, E. A., Andrews, S. M., Espaillat, C., van Kempen, T. A., Wilner, D. J., and Pascucci, I. (2010). The Disk Imaging Survey of Chemistry with SMA. I. Taurus Protoplanetary Disk Data. *Astrophysical Journal*, 720(1):480–493.

Öberg, K. I., van Dishoeck, E. F., and Linnartz, H. (2009b). Photodesorption of ices I: CO, N_2, and CO_2. *Astronomy and Astrophysics*, 496(1):281–293.

Ostriker, E. C., Stone, J. M., and Gammie, C. F. (2001). Density, Velocity, and Magnetic Field Structure in Turbulent Molecular Cloud Models. *Astrophysical Journal*, 546(2):980–1005.

Pallottini, A., Ferrara, A., Bovino, S., Vallini, L., Gallerani, S., Maiolino, R., and Salvadori, S. (2017). The impact of chemistry on the structure of high-z galaxies. *Monthly Notices of the RAS*, 471(4):4128–4143.

Pan, L. and Padoan, P. (2009). The Temperature of Interstellar Clouds from Turbulent Heating. *Astrophysical Journal*, 692(1):594–607.

Perotti, G., Cacciapuoti, L., Tung, N. D., Grassi, T., Schisano, E., and Testi, L. (2024). Planet Formation and Disk Chemistry: Dust and Gas Evolution during Planet Formation. *arXiv e-prints*, page arXiv:2407.03520.

Pontoppidan, K. M., Salyk, C., Bergin, E. A., Brittain, S., Marty, B., Mousis, O., and Öberg, K. I. (2014). Volatiles in Protoplanetary Disks. In Beuther, H., Klessen, R. S., Dullemond, C. P., and Henning, T., editors, *Protostars and Planets VI*, pages 363–385.

Price, D. J. and Monaghan, J. J. (2005). Smoothed Particle Magnetohydrodynamics - III. Multidimensional tests and the $\nabla.B= 0$ constraint. *Monthly Notices of the RAS*, 364(2):384–406.

Price, D. J. and Monaghan, J. J. (2007). An energy-conserving formalism for adaptive gravitational force softening in smoothed particle hydrodynamics and N-body codes. *Monthly Notices of the RAS*, 374(4):1347–1358.

Richings, A. J. and Schaye, J. (2016). The effects of metallicity, UV radiation and non-equilibrium chemistry in high-resolution simulations of galaxies. *Monthly Notices of the RAS*, 458(1):270–292.

Ruaud, M., Wakelam, V., Gratier, P., and Bonnell, I. A. (2018). Influence of galactic arm scale dynamics on the molecular composition of the cold and dense ISM. I. Observed abundance gradients in dense clouds. *Astronomy and Astrophysics*, 611:A96.

Semenov, D., Hersant, F., Wakelam, V., Dutrey, A., Chapillon, E., Guilloteau, S., Henning, T., Launhardt, R., Piétu, V., and Schreyer, K. (2010). Chemistry in disks. IV. Benchmarking gas-grain chemical models with surface reactions. *Astronomy and Astrophysics*, 522:A42.

Shu, F. H., Adams, F. C., and Lizano, S. (1987). Star formation in molecular clouds: observation and theory. *Annual Review of Astronomy and Astrophysics*, 25:23–81.

Tafalla, M., Santiago-García, J., Myers, P. C., Caselli, P., Walmsley, C. M., and Crapsi, A. (2006). On the internal structure of starless cores. II. A molecular survey of L1498 and L1517B. *Astronomy and Astrophysics*, 455(2):577–593.

Tazzari, M., Testi, L., Natta, A., Ansdell, M., Carpenter, J., Guidi, G., Hogerheijde, M., Manara, C. F., Miotello, A., van der Marel, N., van Dishoeck, E. F., and Williams, J. P. (2017). Physical properties of dusty protoplanetary disks in Lupus: evidence for viscous evolution? *Astronomy and Astrophysics*, 606:A88.

Testi, L., Birnstiel, T., Ricci, L., Andrews, S., Blum, J., Carpenter, J., Dominik, C., Isella, A., Natta, A., Williams, J. P., and Wilner, D. J. (2014). Dust Evolution in Protoplanetary Disks. In Beuther, H., Klessen, R. S., Dullemond, C. P., and Henning, T., editors, *Protostars and Planets VI*, pages 339–361.

Tielens, A. G. G. M. (2013). The molecular universe. *Reviews of Modern Physics*, 85(3):1021–1081.

Tomassetti, M., Porciani, C., Romano-Díaz, E., and Ludlow, A. D. (2015). Simulating the H_2 content of high-redshift galaxies. *Monthly Notices of the RAS*, 446(4):3330–3345.

Truelove, J. K., Klein, R. I., McKee, C. F., Holliman, John H., I., Howell, L. H., and Greenough, J. A. (1997). The Jeans Condition: A New Constraint on Spatial Resolution in Simulations of Isothermal Self-gravitational Hydrodynamics. *Astrophysical Journal, Letters*, 489(2):L179–L183.

van Dishoeck, E. F. (2014). Astrochemistry of dust, ice and gas: introduction and overview. *Faraday Discussions*, 168:9.

van Dishoeck, E. F. (2018). Astrochemistry: overview and challenges. In Cunningham, M., Millar, T., and Aikawa, Y., editors, *Astrochemistry VII: Through the Cosmos from Galaxies to Planets*, volume 332, pages 3–22.

van Dishoeck, E. F. and Blake, G. A. (1998). Chemical Evolution of Star-Forming Regions. *Annual Review of Astronomy and Astrophysics*, 36:317–368.

Wakelam, V., Herbst, E., Loison, J. C., Smith, I. W. M., Chandrasekaran, V., Pavone, B., Adams, N. G., Bacchus-Montabonel, M. C., Bergeat, A., Béroff, K., Bierbaum, V. M., Chabot, M., Dalgarno, A., van Dishoeck, E. F., Faure, A., Geppert, W. D., Gerlich, D., Galli, D., Hébrard, E., Hersant, F., Hickson, K. M., Honvault, P., Klippenstein, S. J., Le Picard, S., Nyman, G., Pernot, P., Schlemmer, S., Selsis, F., Sims, I. R., Talbi, D., Tennyson, J., Troe, J., Wester, R., and Wiesenfeld, L. (2012). A KInetic Database for Astrochemistry (KIDA). *Astrophysical Journal, Supplement*, 199(1):21.

Walsh, C., Millar, T. J., Nomura, H., Herbst, E., Widicus Weaver, S., Aikawa, Y., Laas, J. C., and Vasyunin, A. I. (2014). Complex organic molecules in protoplanetary disks. *Astronomy and Astrophysics*, 563:A33.

Whitehouse, S. C. and Bate, M. R. (2006). The thermodynamics of collapsing molecular cloud cores using smoothed particle hydrodynamics with radiative transfer. *Monthly Notices of the RAS*, 367(1):32–38.

Whitehouse, S. C., Bate, M. R., and Monaghan, J. J. (2005). A faster algorithm for smoothed particle hydrodynamics with radiative transfer in the flux-limited diffusion approximation. *Monthly Notices of the RAS*, 364(4):1367–1377.

Whitworth, A. P. (1998). The Jeans instability in smoothed particle hydrodynamics. *Monthly Notices of the RAS*, 296(2):442–444.

Widicus Weaver, S. L. (2019). Millimeterwave and Submillimeterwave Laboratory Spectroscopy in Support of Observational Astronomy. *Annual Review of Astronomy and Astrophysics*, 57:79–112.

Willacy, K., Klahr, H. H., Millar, T. J., and Henning, T. (1998). Gas and grain chemistry in a protoplanetary disk. *Astronomy and Astrophysics*, 338:995–1005.

Williams, J. P. and Cieza, L. A. (2011). Protoplanetary Disks and Their Evolution. *Annual Review of Astronomy and Astrophysics*, 49(1):67–117.

Appendix A

Discs Chemical Distribution

Figures A0.1-A0.12 present the vertical structure plots for different properties of the analyzed discs, i.e., physical properties (ρ_{tot}, A_v, T_{gas} and T_{dust}), and gas- and dust-phase CO, H_2O, HCO, H_2CO, CH_3O and CH_3OH maps.

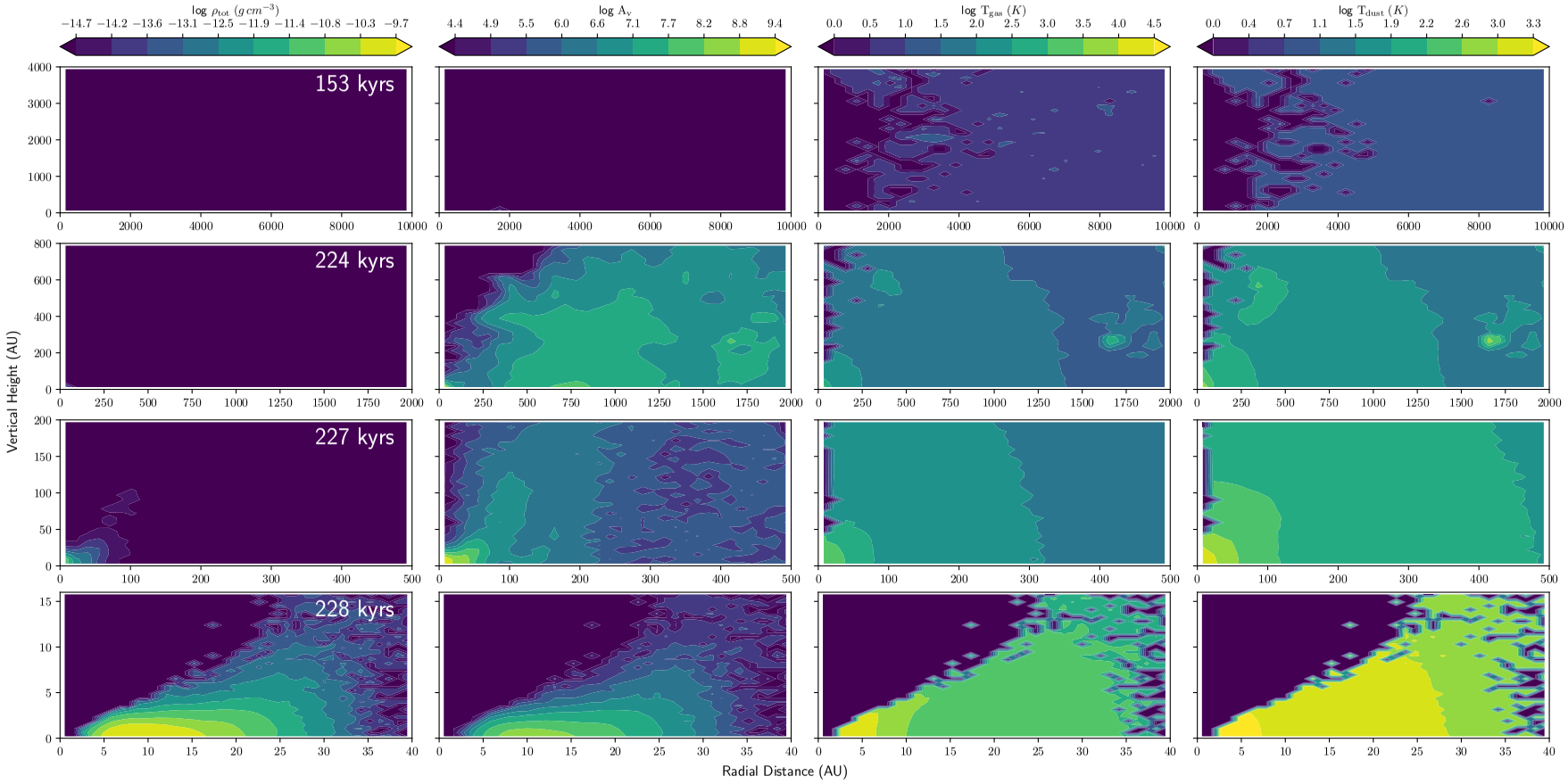

Figure A0.1: Physical structure evolution of the gas around the sink hosting Disc 1. From top to bottom each row is a different time, ranging from 153 to 224 to 227 and 228 kyrs respectively. From left to right we have $\rho_{\rm tot}$, $\rm A_v$, $T_{\rm gas}$ and $T_{\rm dust}$.

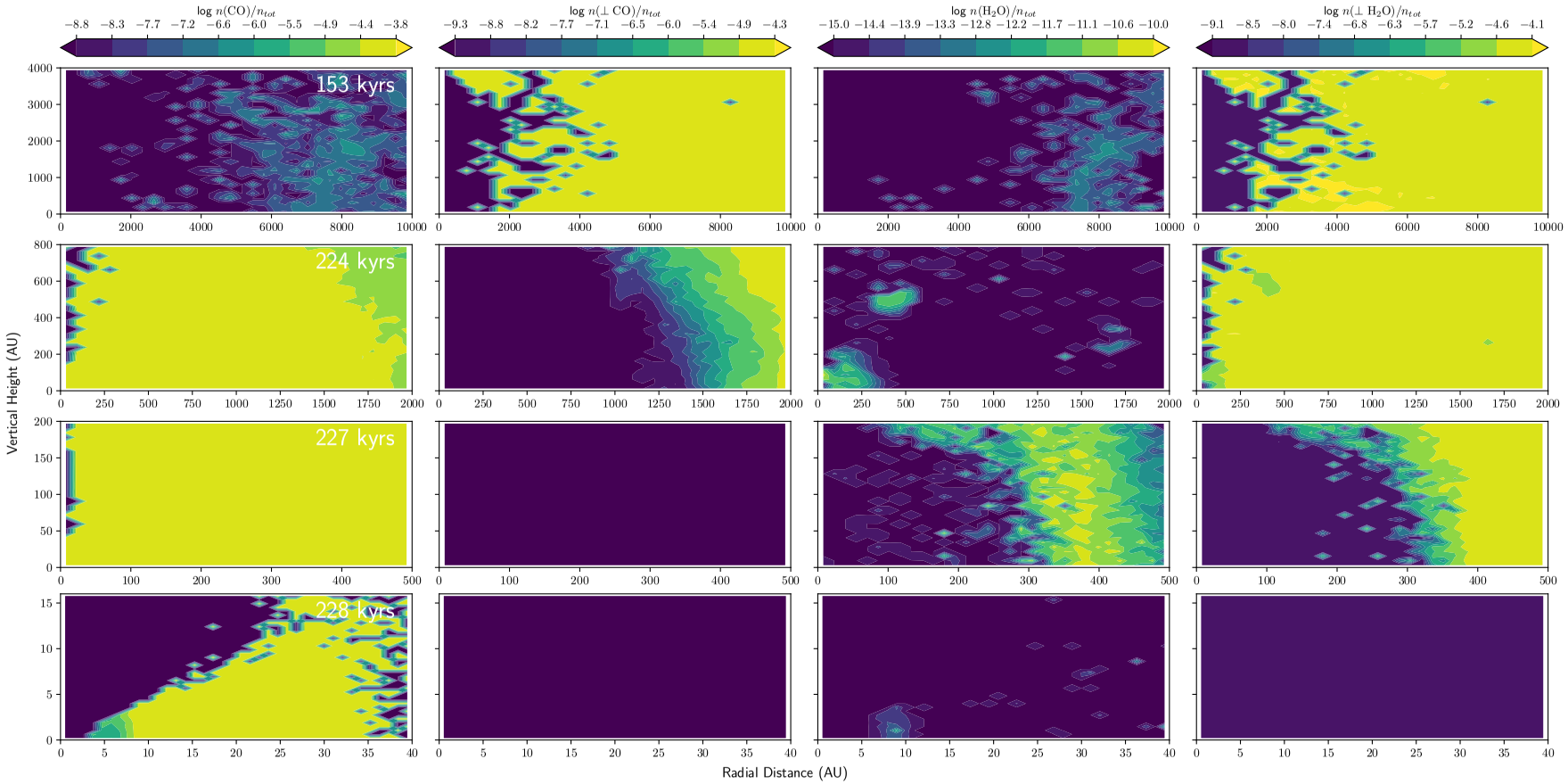

Figure A0.2: Physical structure evolution of the gas around the sink hosting Disc 1. From top to bottom each row is a different time, ranging from 153 to 224 to 227 and 228 kyrs respectively. From left to right we have CO, $\perp$ CO, H_2O and $\perp$ H_2O.

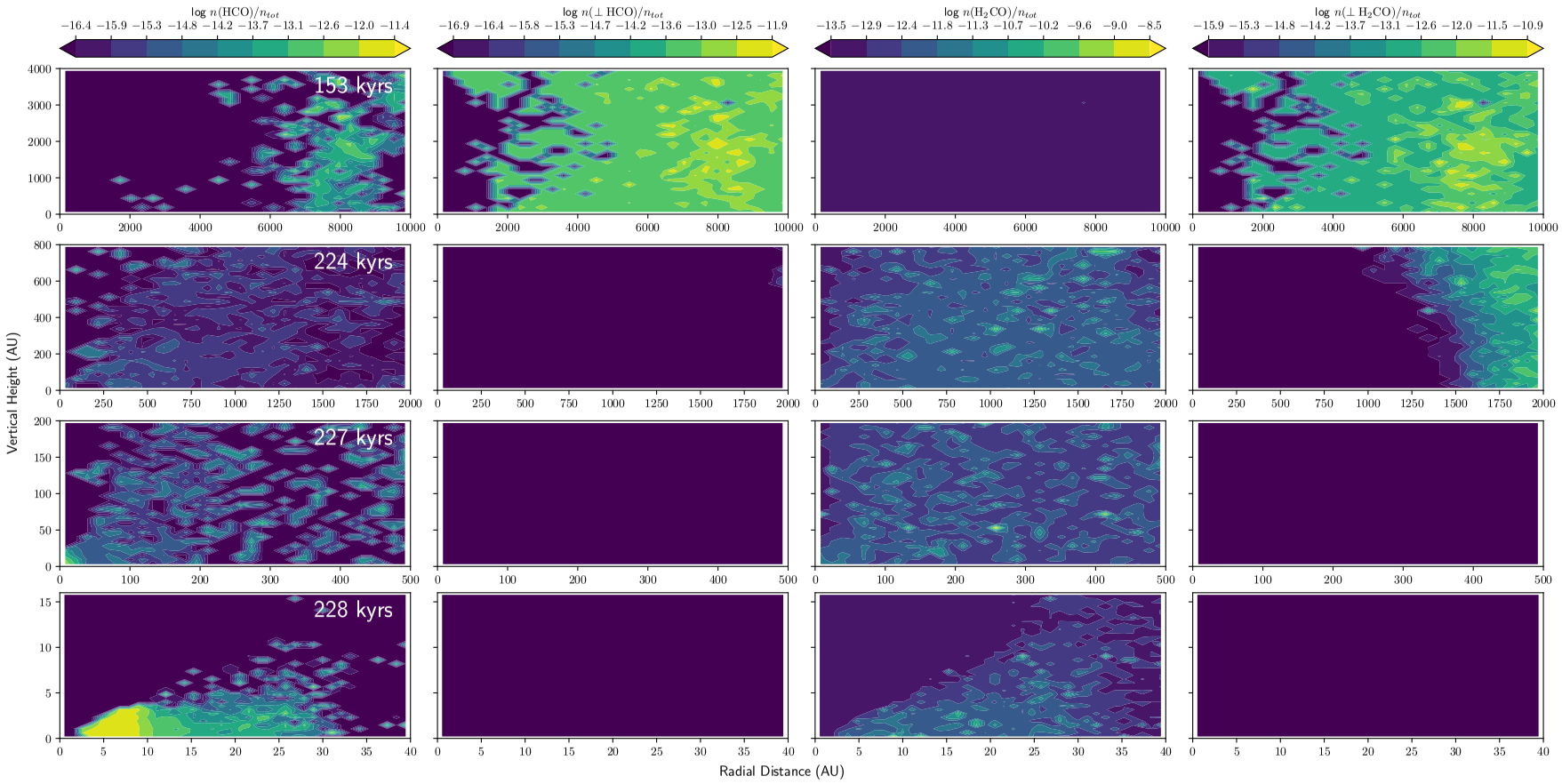

Figure A0.3: Physical structure evolution of the gas around the sink hosting Disc 1. From top to bottom each row is a different time, ranging from 153 to 224 to 227 and 228 kyrs respectively. From left to right we have HCO, $\perp$ HCO, H_2CO and $\perp$ H_2CO.

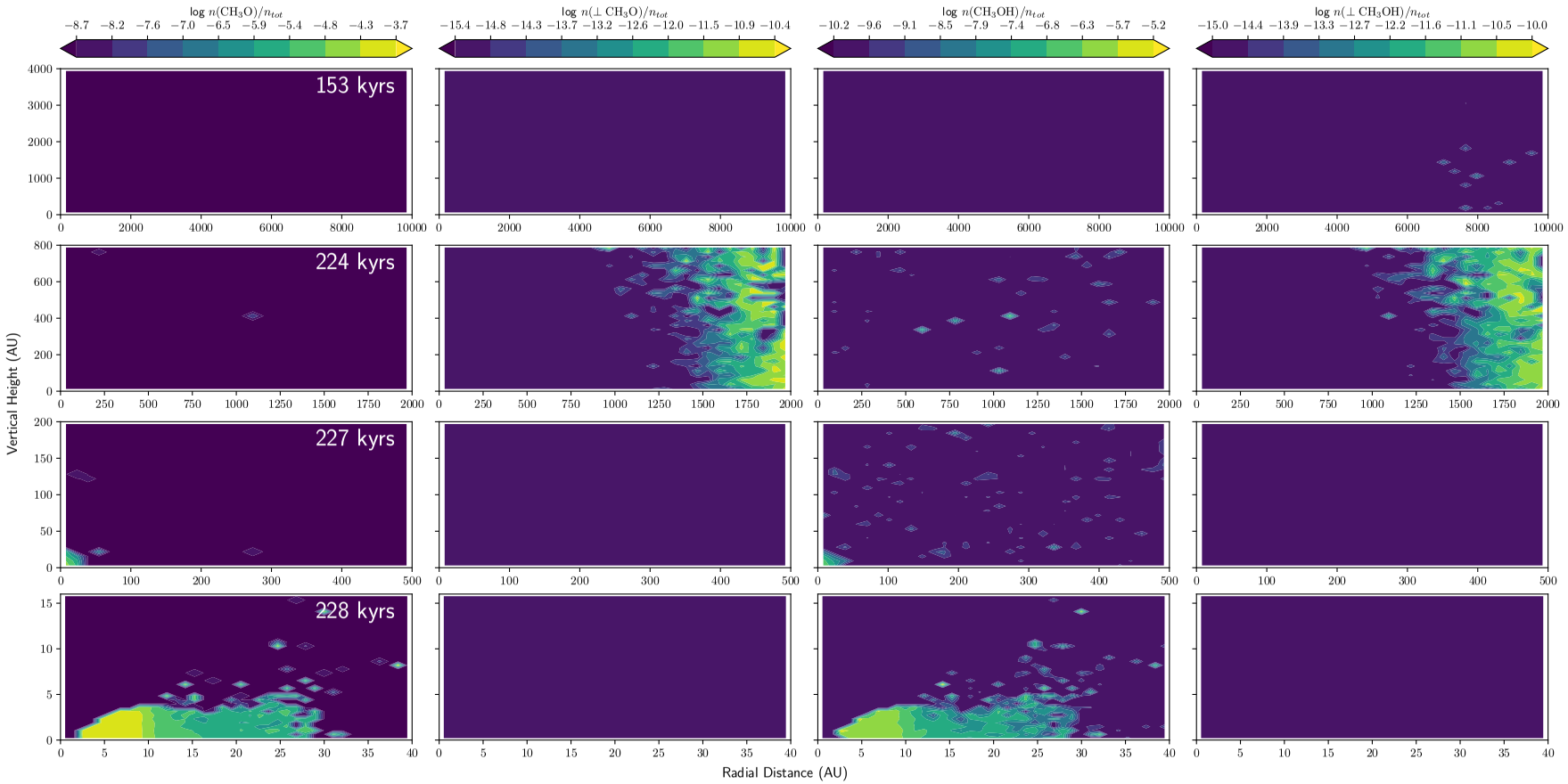

Figure A0.4: Physical structure evolution of the gas around the sink hosting Disc 1. From top to bottom each row is a different time, ranging from 153 to 224 to 227 and 228 kyrs respectively. From left to right we have CH_3O, $\perp$ CH_3O, CH_3OH and $\perp$ CH_3OH.

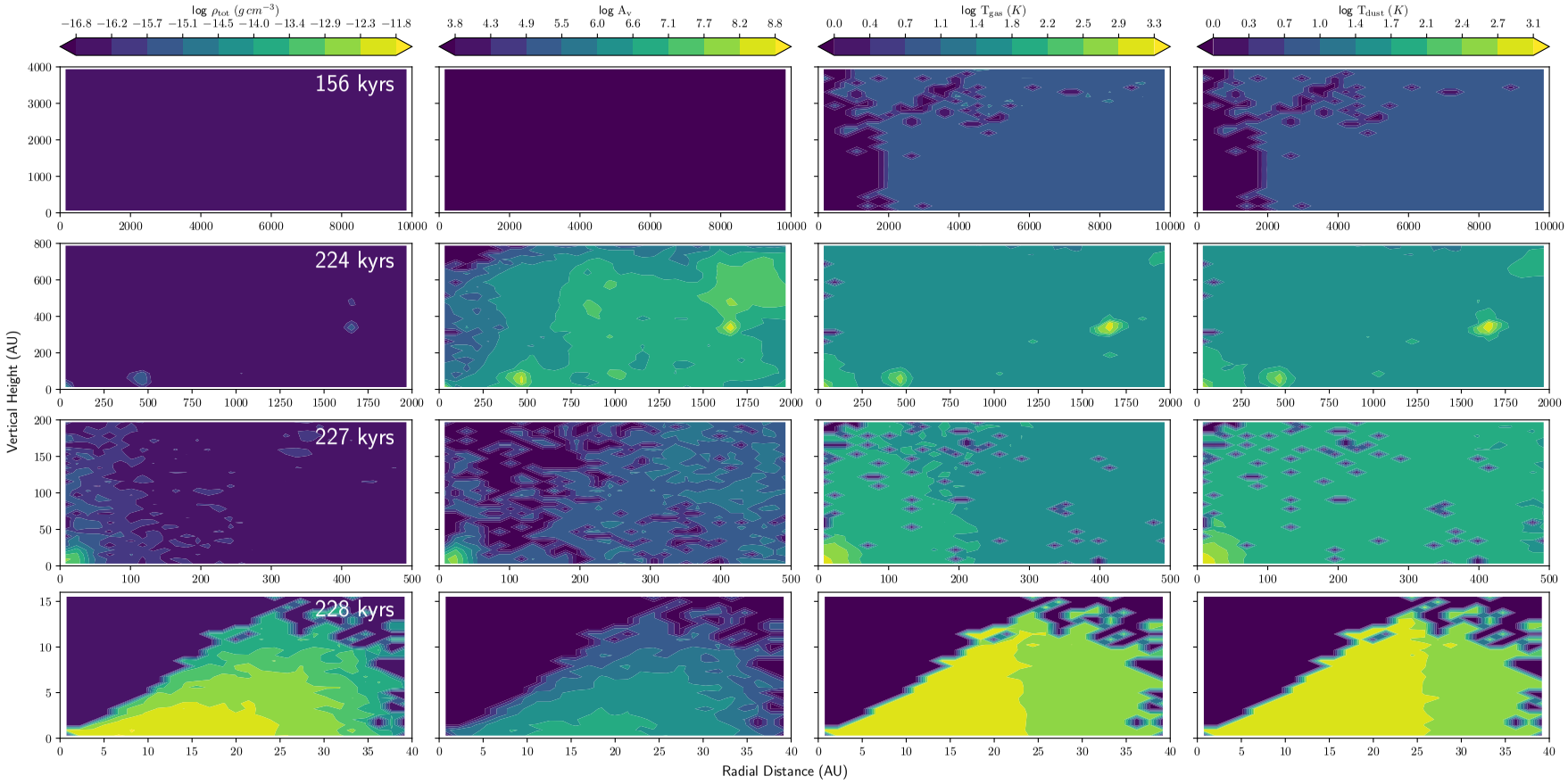

Figure A0.5: Physical structure evolution of the gas around the sink hosting Disc 3. From top to bottom, each row is a different time, ranging from 156 to 224 to 227 and 228 kyrs respectively. From left to right we have $\rho_{\rm tot}$, $\rm A_v$, $T_{\rm gas}$ and $T_{\rm dust}$.

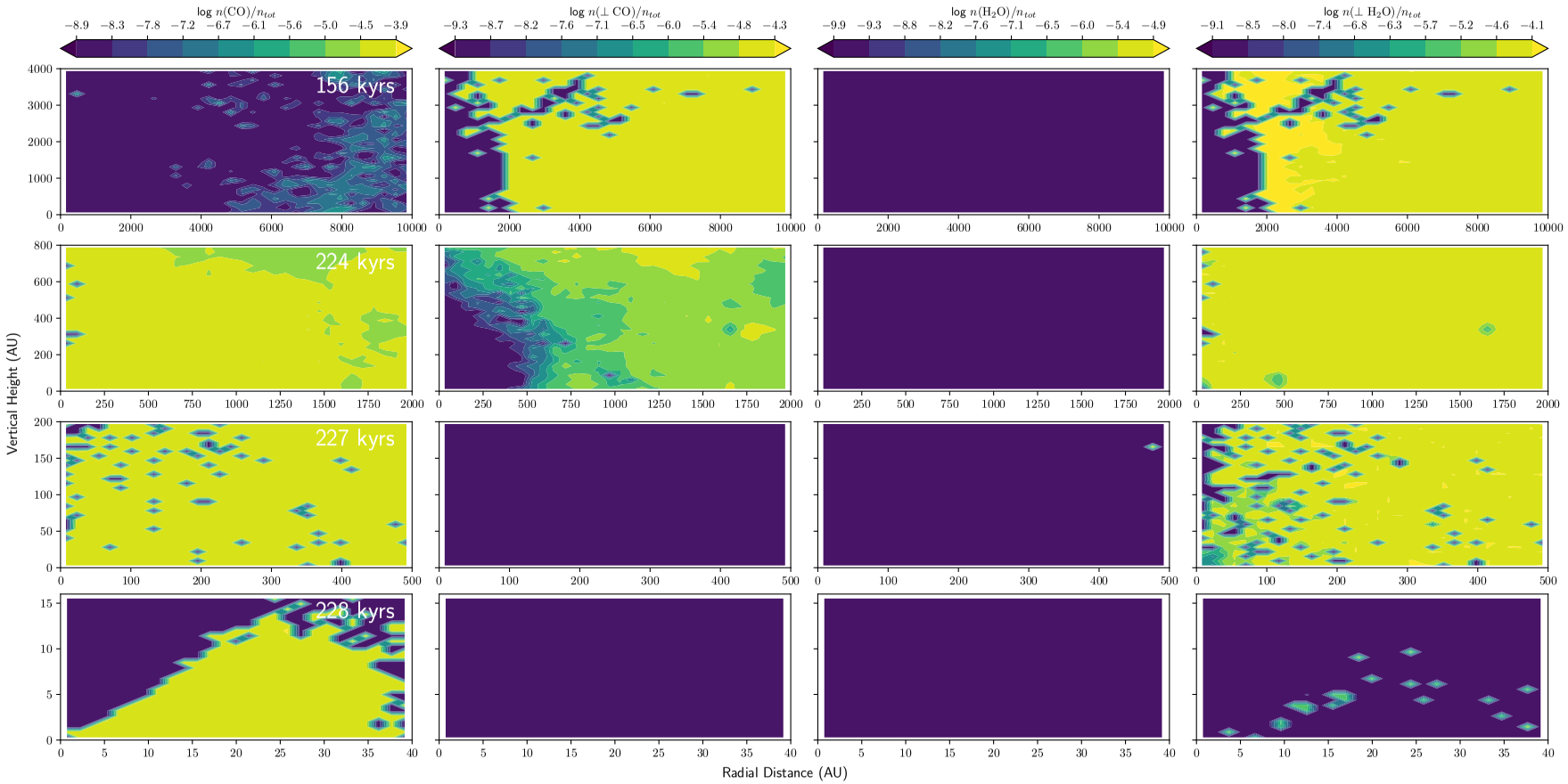

Figure A0.6: Physical structure evolution of the gas around the sink hosting Disc 3. From top to bottom each row is a different time, ranging from 156 to 224 to 227 and 228 kyrs respectively. From left to right we have CO, $\perp$ CO, H_2O and $\perp$ H_2O.

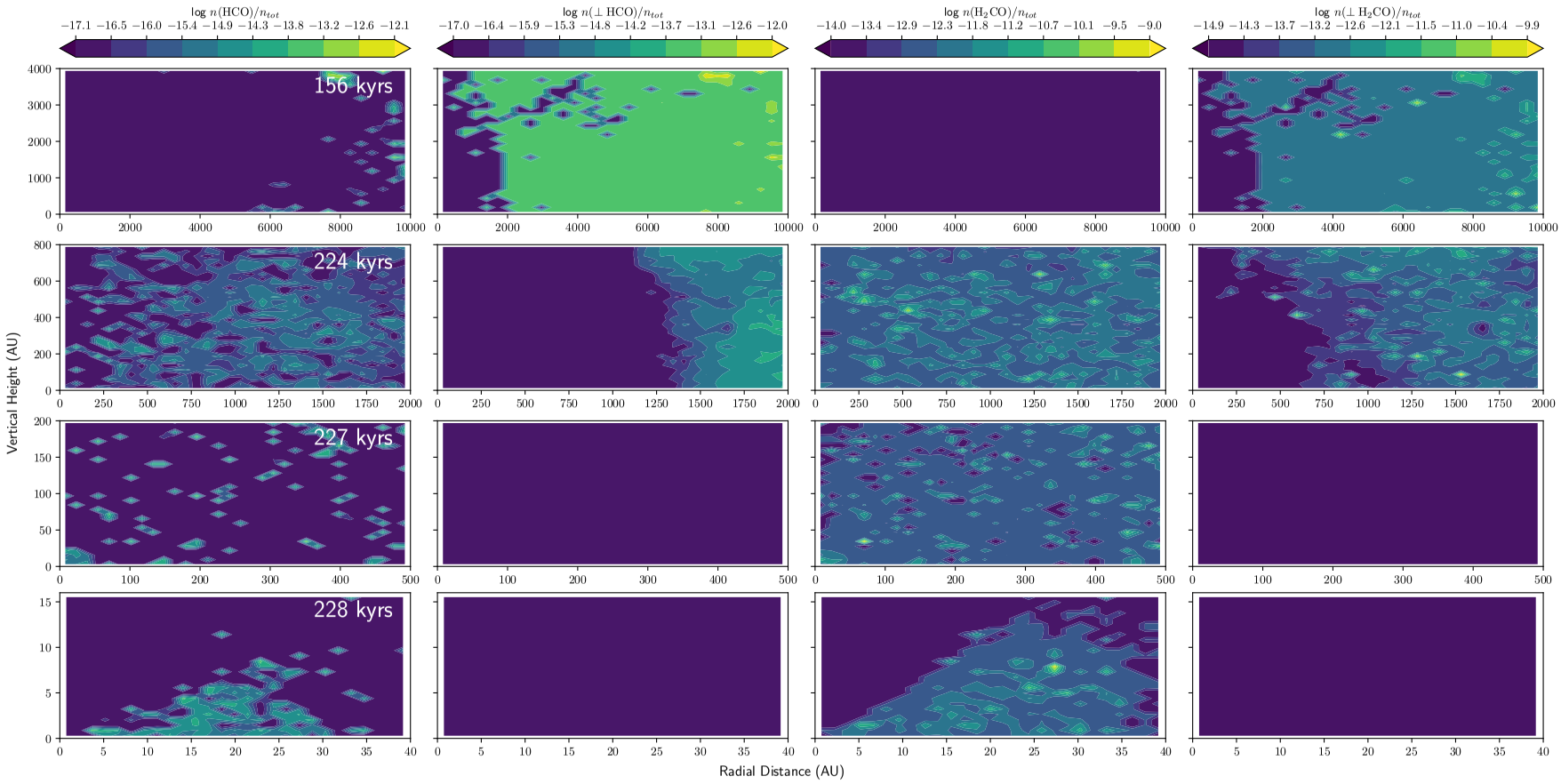

Figure A0.7: Physical structure evolution of the gas around the sink hosting Disc 3. From top to bottom each row is a different time, ranging from 156 to 224 to 227 and 228 kyrs respectively. From left to right we have HCO, $\perp$ HCO, H_2CO and $\perp$ H_2CO.

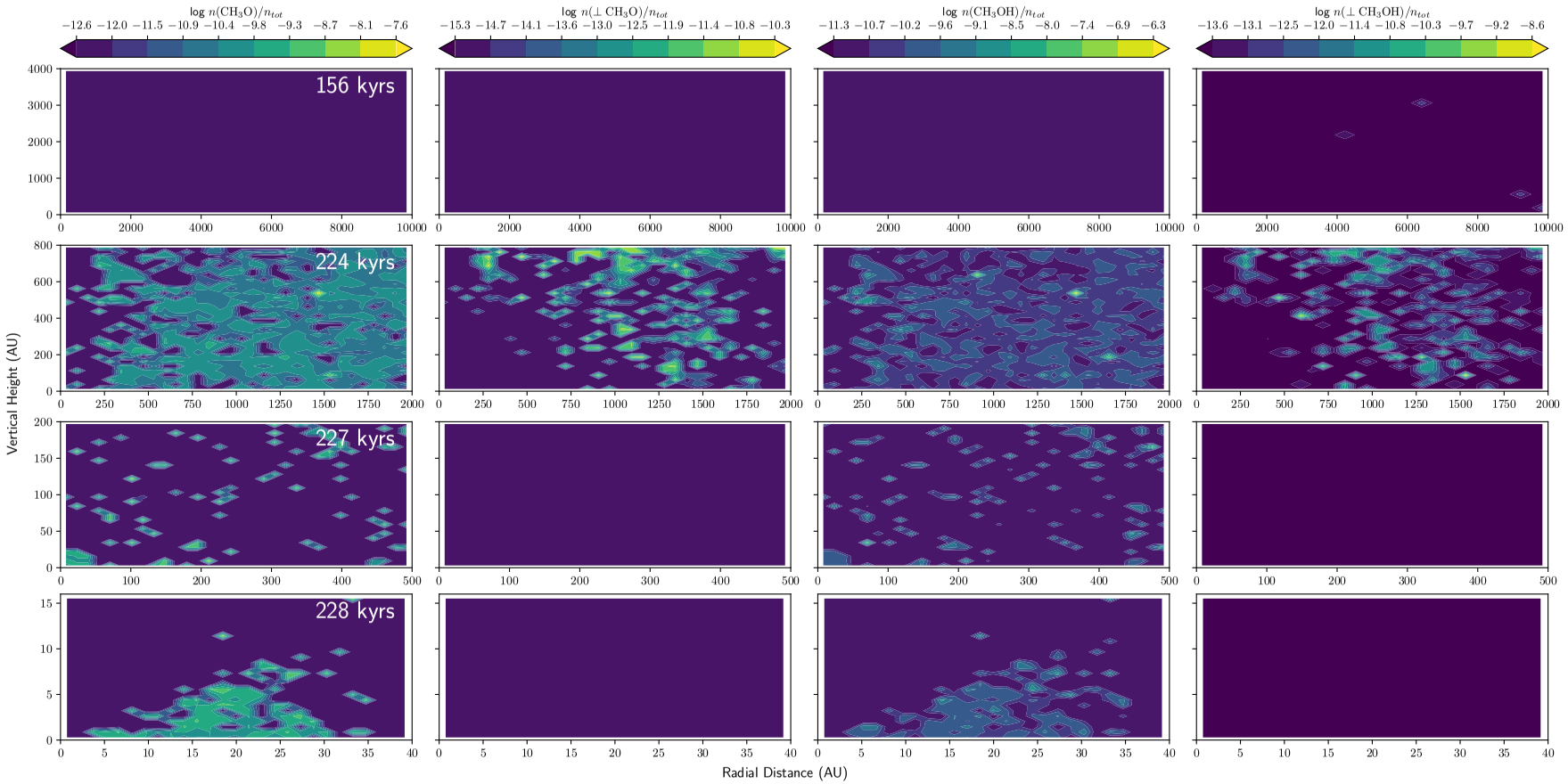

Figure A0.8: Physical structure evolution of the gas around the sink hosting Disc 3. From top to bottom each row is a different time, ranging from 156 to 224 to 227 and 228 kyrs respectively. From left to right we have CH_3O, $\perp$ CH_3O, CH_3OH and $\perp$ CH_3OH.

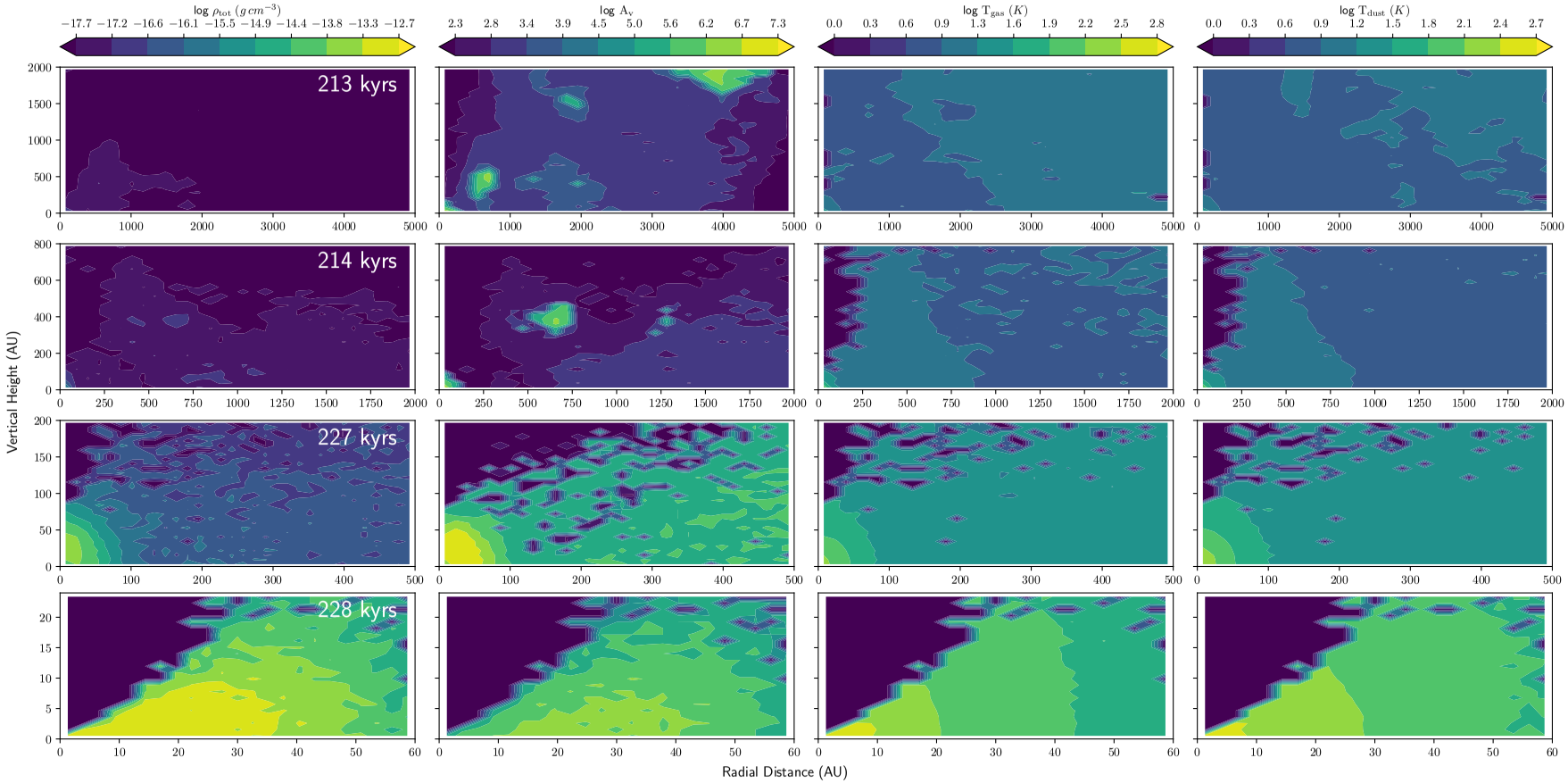

Figure A0.9: Physical structure evolution of the gas around the sink hosting Disc 6. From top to bottom each row is a different time, ranging from 213 to 214 to 227 and 228 kyrs respectively. From left to right we have $\rho_{\rm tot}$, $\rm A_v$, $T_{\rm gas}$ and $T_{\rm dust}$.

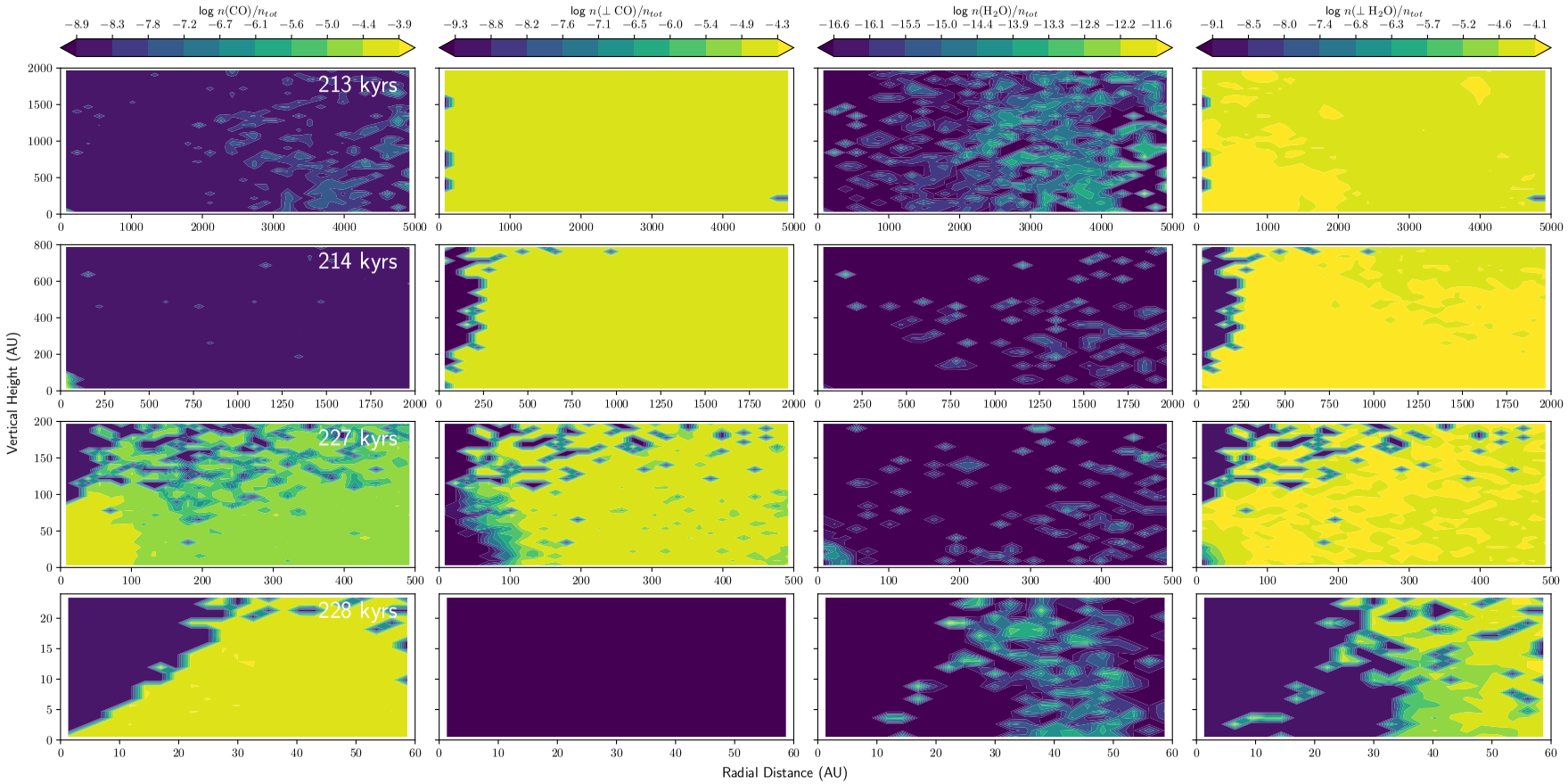

Figure A0.10: Physical structure evolution of the gas around the sink hosting Disc 6. From top to bottom each row is a different time, ranging from 213 to 214 to 227 and 228 kyrs respectively. From left to right we have CO, $\perp$ CO, H_2O and $\perp$ H_2O.

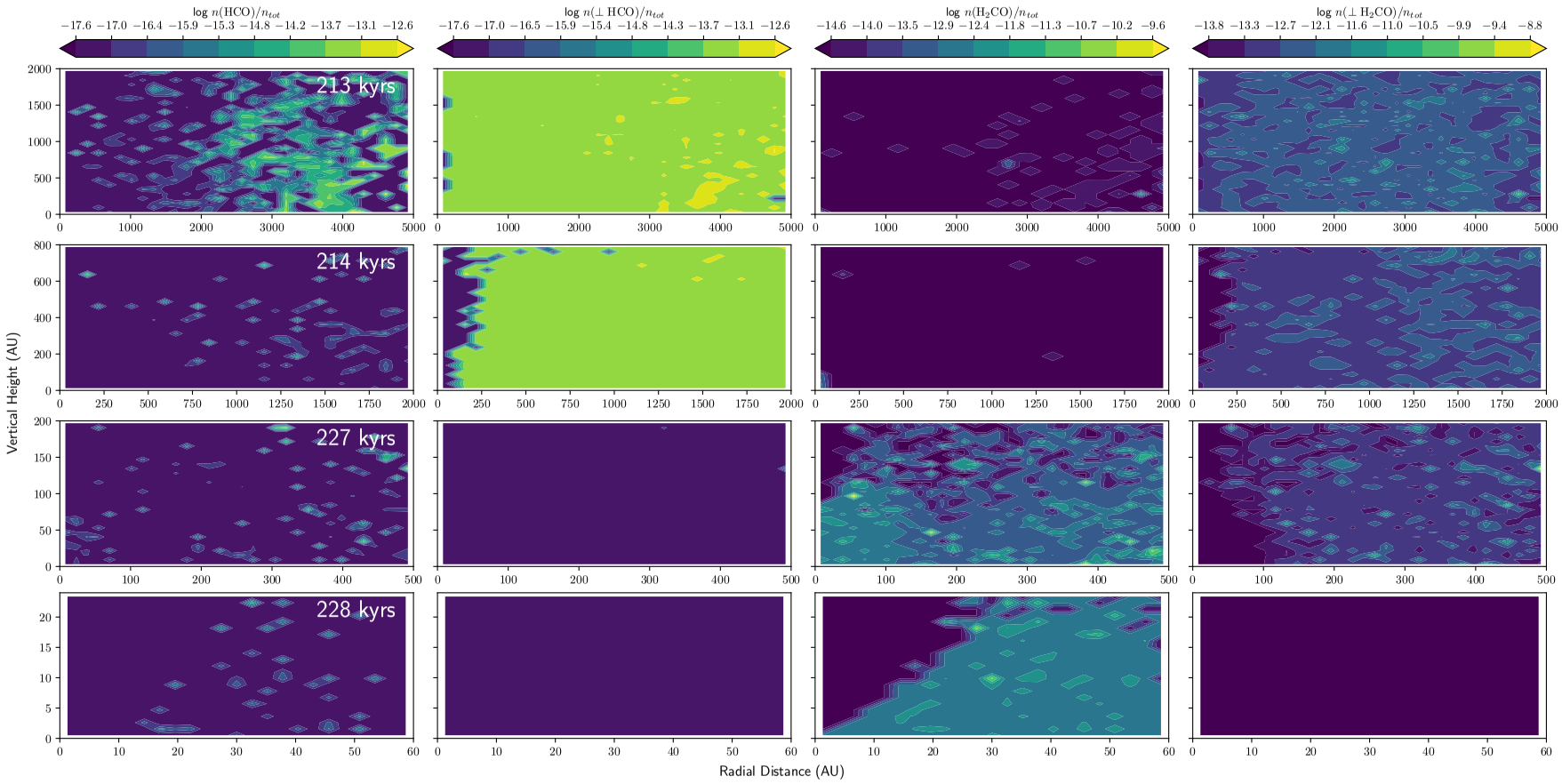

Figure A0.11: Physical structure evolution of the gas around the sink hosting Disc 6. From top to bottom each row is a different time, ranging from 213 to 214 to 227 and 228 kyrs respectively. From left to right we have HCO, $\perp$ HCO, H_2CO and $\perp$ H_2CO.

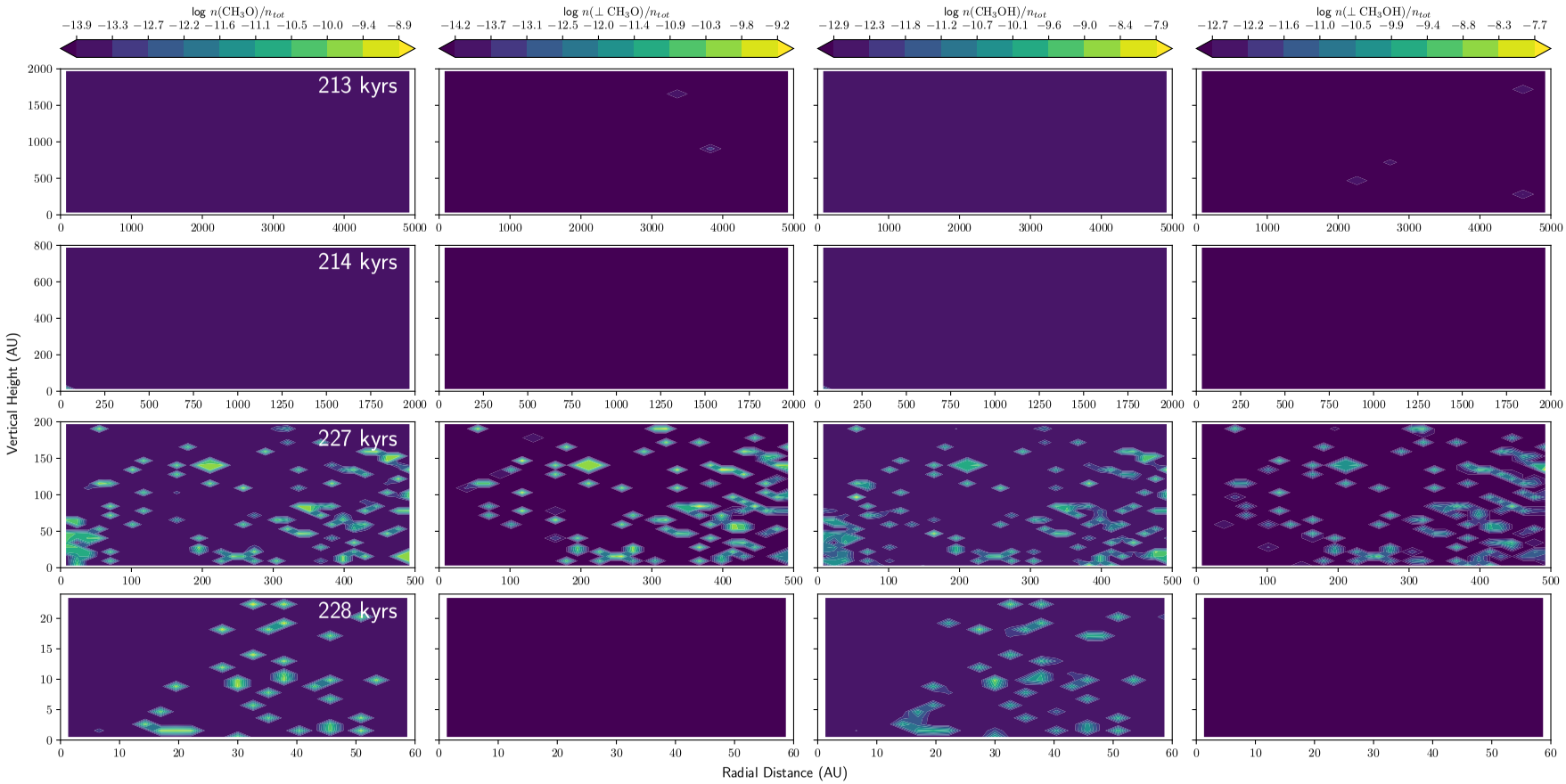

Figure A0.12: Physical structure evolution of the gas around the sink hosting Disc 6. From top to bottom each row is a different time, ranging from 213 to 214 to 227 and 228 kyrs respectively. From left to right we have CH_3O, $\perp$ CH_3O, CH_3OH and $\perp$ CH_3OH.